Hyper Resolute Laser Writing mediated by tailored ENZ Metamaterials:

The specific case of All-Dielectric Broadband Metalenses

Doctoral thesis
2020/2021

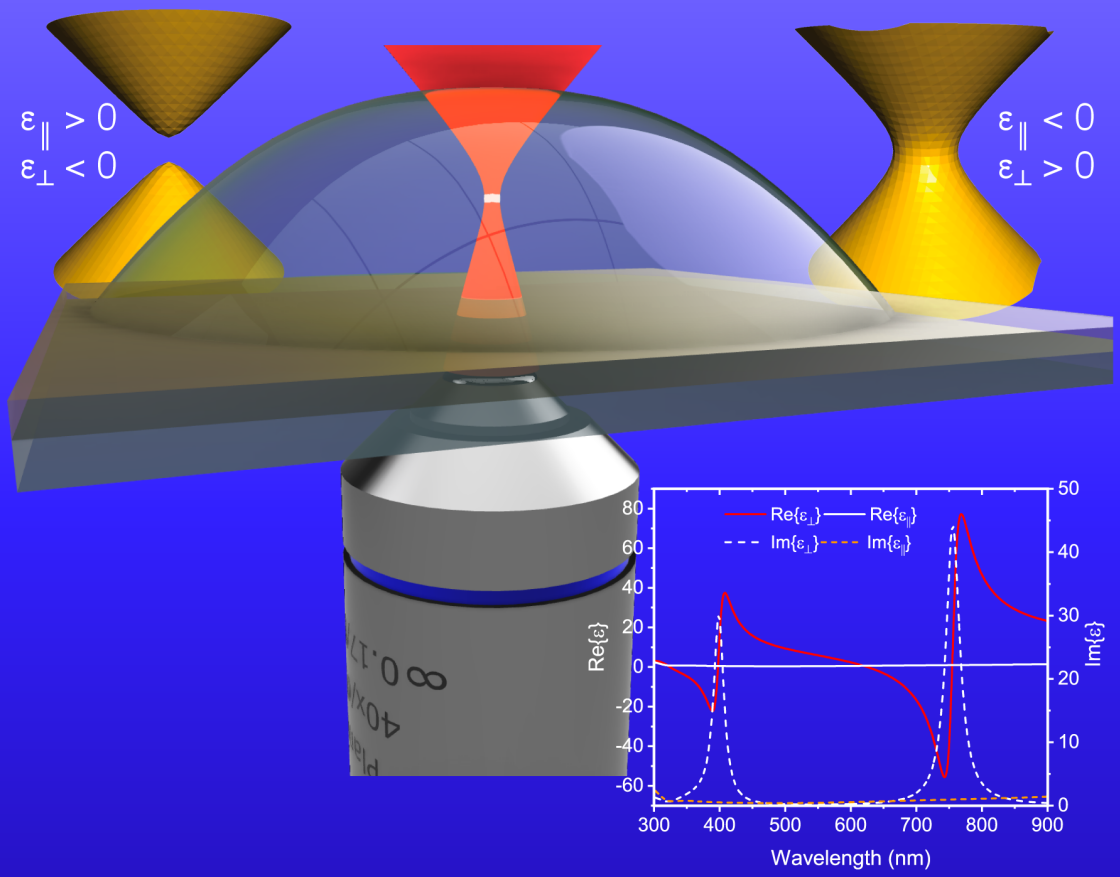

Dr. Giuseppe Emanuele Lio

Department of Physics,
Institute of Nanotechnology at
University of Calabria and CNR-Nanotec

Doctorate in Science and Technology of Physics,
Chemistry and Materials

UNIVERSITÀ DELLA CALABRIA

Dipartimento di Fisica

Dottorato di ricerca in

Scienze e Tecnologie Fisiche, Chimiche e dei Materiali

Ciclo
XXXIII

Hyper Resolute Laser Writing mediated by tailored ENZ Metamaterials:
The specific case of All-Dielectric Broadband Metalenses

Settore Scientifico Disciplinare in: Fisica della Materia FIS/03

Coordinatore:

Ch.ma Prof.ssa Gabriella CIPPARRONE
Firma
Firma oscurata in base alle linee guida del Garante della privacy

Supervisore/Tutor:

Ch.mo Prof. Roberto CAPUTO
Firma
Firma oscurata in base alle linee guida del Garante della privacy

Egr. Dott. Michele GIOCONDO
Firma
Firma oscurata in base alle linee guida del Garante della privacy

Ch.mo Prof. Antonio DE LUCA
Firma
Firma oscurata in base alle linee guida del Garante della privacy

Dottorando:

Dott. Giuseppe Emanuele LIO
Firma
Firma oscurata in base alle linee guida del Garante della privacy

Dedicated to my Parents

Vincenzo and Patrizia

"Regola I. Delle cose naturali non devono essere ammesse cause più numerose di quelle che sono vere e bastano a spiegare i fenomeni. Come dicono i filosofi: la natura non fa nulla invano, e inutilmente viene fatto con molte cose ciò che può essere fatto con poche. La natura, infatti, è semplice e non sovrabbonda in cause superflue delle cose. "

"Rule I. We are to admit no more causes of natural things such as are both true and sufficient to explain their appearances. To this purpose the philosophers say that Nature does nothing in vain, and more is in vain when less will serve; for Nature is pleased with simplicity, and effects not the pomp of superfluous causes"

Sir. Isaac Newton

Contents

Acknowledgements **vi**

Declaration of Authorship **vii**

List of Publications **ix**

List of Abbreviations **xi**

List of Symbols and Constants **xii**

Abstract **xiii**

Introduzione **xvi**

1 Main theoretical aspects **1**
1.1 Metamaterials: general point of view 1
1.1.1 Hyperbolic Metamaterials 3
1.1.2 Layered metal-dielectric structures 5
1.1.3 ϵNear Zero (and Pole) Metamaterials 6
1.2 Plasmons at metal/ dielectric interface, in metamaterials and optical nano-cavities 9
1.3 Subwavelength metamaterials for imaging and super-lenses . 12
1.3.1 Collimation effect in ϵNear Zero and Pole metamaterials and Lens effect 14
1.4 Conclusion 17

2 Metamaterials Design and Experimental Characterization **18**
2.1 Ellipsometry 19
2.2 Transfer Matrix Method 21
2.3 Numerical ellipsometer by using COMSOL Multiphysics . . . 23
2.4 Numerical and experimental examples of spectroscopic ellipsometry 26
2.5 Color gamut a macroscopic effects of plasmonic modes inside optical nano-cavities 31
2.6 Pseudo dielectric function $< \tilde{\varepsilon} >$ in MIMI cavity: an effective way to recognize the plasmonic resonances 34
2.7 Conclusion 41

3 The MIMI device prototype for the Hyper Resolution in two photon direct laser writing (TP-DLW) process **43**
3.1 One and two-photon lithography 43
3.2 MIMI device for TP-DLW process 49

3.3 Results of the hyper resolute TP-DLW lithography 52
3.4 Conclusion 56

4 All-Dielectric Apochromatic Broadband Metalenses: Design, TP-DLW fabrication and Characterization 57
4.1 Metalenses: the state of art 58
4.2 Metalenses design assisted by Deep Machine Learning 59
4.3 Morphological and microscopic characterization 64
4.4 Experimental Results: All-dielectric metalenses optical carachterization 66
4.5 Conclusion 69

Conclusions and perspectives 71

A The Effective Medium Theory 75

B The TMM code in Matlab 77

List of Figures 78

Bibliography 85

Acknowledgements

At the end of this experience, I would like to thank the following people who have helped me to undertake this research:

My supervisor *Prof. Roberto Caputo* for his enthusiasm for the project, for his support, encouragement and patience. I would like to say that I am grateful to him because he was and he is my beacon in science. He introduced me in the scientific world and he taught me to address any issue that occurred. The meetings and conversations with him were vital in inspiring me to think outside the box, from multiple perspectives to form a comprehensive and objective critique.

I would like to thank my other supervisors *Prof. Antonio De Luca* and *Dr. Michele Giocondo*, who gave me the opportunity to work with them and to learn the professional skills that now I have. I also thank *Prof. Giuseppe Strangi* for the opportunity to work with him and in the NanoPlasm-laboratory at the Case Western Reserve University.

I would say thanks to my colleagues and friends met in these years. I thank *Antonio Ferraro* for his supporting in each situation. I thank *Giovanna* that introduced me on this doctoral carrier, and I thank *Tiziana* that gave me knowledges to face out many hard challenges. Finally, I would also thank *Vincenzo* for interesting scientific discussions.

I thank *Dante*, *Biagio*, *Antonio Condello*, *Ylli* and *Alexa* who were always present in these academic years.

I am very grateful to my parents, *Vincenzo* and *Patrizia*, who encouraged and supported me during all my studies.

Last but not the least, a very special thank is for a very exceptional person, *Filomena*, who followed and supported me in this experience staying always by my side.

Declaration of Authorship

I, Dott. Giuseppe Emanuele LIO, declare that this thesis titled, "**Hyper Resolute Laser Writing mediated by tailored ENZ Metamaterials: The specific case of All-Dielectric Broadband Metalenses**" and the work presented in it are my own. I confirm that:

- This work was done wholly or mainly while in candidature for a research degree at this University.
- Where any part of this thesis has previously been submitted for a degree or any other qualification at this University or any other institution, this has been clearly stated.
- Where I have consulted the published work of others, this is always clearly attributed.
- Where I have quoted from the work of others, the source is always given. With the exception of such quotations, this thesis is entirely my own work.
- I have acknowledged all main sources of help.
- Where the thesis is based on work done by myself jointly with others, I have made clear exactly what was done by others and what I have contributed myself.

Signed: 

Date: 12/03/2021

List of Publications

This Ph.D. thesis is based on the following publications:

1. Giuseppe Emanuele Lio, Antonio Ferraro, Tiziana Ritacco, Dante Maria Aceti, Antonio De Luca, Michele Giocondo and Roberto Caputo. **"Leveraging on ENZ Metamaterials to achieve 2D and 3D Hyper Resolution in Two-Photon Direct Laser Writing"**. In: "Advanced Materials", 2021.

2. Giuseppe Emanuele Lio and Antonio Ferraro. **LIDAR and Beam Steering Tailored by Neuromorphic Metasurfaces Dipped in a Tunable Surrounding Medium**. In: "Photonics" 8.3 (2021).

3. Giuseppe Emanuele Lio, Antonio Ferraro, Tiziana Ritacco, Dante Maria Aceti, Antonio De Luca, Roberto Caputo, and Michele Giocondo. **"Hyper Resolute Ultra Thin LowCost All-Dielectric Broadband Achromatic Metalenses"**. In: "arXiv", preprint arXiv:2008.03250, 2020.

4. Giuseppe Emanuele Lio, Tiziana Ritacco, Antonio Ferraro, Antonio De Luca, Roberto Caputo, and Michele Giocondo. **"Hyper Resolution Two Photon Direct Laser Writing using ENZ Nano-Cavity"**. In: "arXiv", preprint arXiv:2007.13509, 2020.

5. Giovanna Palermo, Kandammathe Valiyaveedu Sreekanth, Nicolò Maccaferri, Giuseppe Emanuele Lio, Giuseppe Nicoletta, Francesco De Angelis, Michael Hinczewski, and Giuseppe Strangi. **"Hyperbolic dispersion metasurfaces for molecular biosensing"**. In: "Nanophotonics" -Review-, vol. 10(1), pp. 295 - 314, 2020.

6. Giuseppe Emanuele Lio, Antonio Ferraro, Michele Giocondo, Roberto Caputo, and Antonio De Luca, **"Color gamut behavior in epsilon near-zero nanocavities during propagation of gap surface plasmons"**. Advanced Optical Materials, vol. 8, no. 17, p. 2 000 487, 2020.

7. Giuseppe Emanuele Lio, Antonio De Luca, Cesare Paolo Umeton, and Roberto Caputo. **"Opto-mechanically induced thermoplasmonic response of unclonable flexible tags with hotspot fingerprint"**. Journal of Applied Physics, vol. 128.9, p. 093107,2020.

8. Giovanna Palermo, Giuseppe Emanuele Lio, and Giuseppe Strangi, **"Compressed and canalized emission of quantum emitters in mim nanocavities"**. Quantum Stud.: Math. Found., vol. 7, pp. 355–361, 2020.

9. Giovanna Palermo, Giuseppe Emanuele Lio, Marco Esposito, Loredana Ricciardi, Mariachiara Manoccio, Vittorianna Tasco, Adriana Passaseo, Antonio De Luca, and Giuseppe Strangi, **"Biomolecular sensing at the**

interface between chiral metasurfaces and hyperbolic metamaterials". ACS Applied Materials & Interfaces, vol. 12, no. 27, pp. 30181"30188, 2020.

10. Giuseppe Emanuele Lio, Josslyn Beltran Madrigal, Christophe Couteau, Sylvain Blaize, and Roberto Caputo , **"Conceptual implementation of a photonic-plasmonic transistor onto a structured nano-guided hybrid system"**. Physica status solidi (a), vol. 217, no. 11, p. 1 900 911, 2020.

11. Xiaolun Xu, Josslyn Beltran Madrigal, Aurèllie Broussier, Giuseppe Emanuele Lio, Fabien Geoffray, Ali Issa, Safi Jradi, Renaud Bachelot, Christophe Couteau, and Sylvain Blaize, **"Quantum emitters based on polymeric structures embedded with quantum dots fabricated via photo- polymerization"**. Advanced Fabrication Technologies for Micro/Nano Optics and Photonics XIII, G. von Freymann, E. Blasco, and D. Chanda, Eds., International Society for Optics and Photonics, vol. 11292, SPIE, pp. 59 "66, 2020.

12. Giuseppe Emanuele Lio, Giovanna Palermo, Antonio De Luca, and Roberto Caputo, **"Tensile control of the thermal flow in plasmonic heaters realized on flexible substrates"**. The Journal of Chemical Physics, vol. 151, no. 24, p. 244 707, 2019.

13. Giuseppe Emanuele Lio, Giovanna Palermo, Roberto Caputo, and Antonio De Luca, **"A comprehensive optical anal- ysis of nanoscale structures: From thin films to asymmetric nanocavities"**. RSC advances, vol. 9, no. 37, pp. 21 429"21 437, 2019.

14. Giuseppe Emanuele Lio, Josslyn Beltran Madrigal, Xiaolun Xu, Ying Peng, Stefano Pierini, Christophe Couteau, Safi Jradi, Renaud Bachelot, Roberto Caputo, and Sylvain Blaize, **"Integration of nanoemitters onto photonic structures by guided evanescent-wave nano- photopolymerization"**. The Journal of Physical Chemistry C, vol. 123, no. 23, pp. 14 669"14 676, 2019.

15. Giuseppe Emanuele Lio, Giovanna Palermo, Roberto Caputo, and Antonio De Luca, **"Opto-mechanical control of flexible plasmonic materials"**. Journal of Applied Physics, vol. 125, no. 8, p. 082 533, 2019.

16. Fausto D Apuzzo, Marco Esposito, Massimo Cuscunà, Alessandro Cannavale, Salvatore Gambino, Giuseppe E Lio, Antonio De Luca, Giuseppe Gigli, and Stefano Lupi, **"Mid-infrared plasmonic excitation in indium tin oxide microhole arrays"**. ACS Photonics, vol. 5, no. 6, pp. 2431"2436, 2018.

List of Abbreviations

HMM	**H**yperbolic **M**eta**M**materials
ϵ**NZ**	ϵ **N**ear **Z**ero
ϵ**NZP**	ϵ **N**ear **Z**ero and **P**ole
FWHM	**F**ull **W**idth at **H**alf **M**aximum
DR	**D**ispersion **R**elation
SPP	**S**urface **P**lasmon **P**olariton
GSP	**G**ap **S**urface **P**lasmon
TMM	**T**ransfer **Matrix** **M**ethod
TP	**T**wo **P**hotons
DLW	**T**wo **P**hotons **D**irect **L**aser **W**riting
TP-DLW	**D**irect **L**aser **W**riting
TPA	**T**wo **P**hotons **A**bsorption
TPP	**T**wo **P**hotons **P**olymerization
voxel	Volume pixel
PEW	**P**hotopolymerisation by **E**vanescent **W**ave
EBL	**E**lectron **B**eam **L**ithography
FZP	**F**resnel **Z**one **P**lates
PSF	**P**oint **S**pread **F**unction
DOF	**D**epth **O**f **F**ocus

List of Symbols and Constants

c_0	Speed of light	$2.997\,924\,58 \times 10^8\,\mathrm{m\,s^{-1}}$ (exact)
ε_0	Dielectric vacuum constant	$8.85 \times 10^{12}\,\mathrm{F\,m^{-1}}$ (exact)
ω	Angular frequency	rad/s
λ	Wavelength	nm
k	wave vector	μm^{-1}
ε_r	Relative dielectric constant	
μ_r	Relative permability	
$\parallel$	Parallel direction	
$\perp$	Perpendicular direction	
ε_1	Permittivity real part	
ε_2	Permittivity imaginary part	
$\Psi\Delta$	The ellipsometer parameters	
$< \tilde{\varepsilon} >$	Pseudo dielectric function	
E	Energy	eV
ΔE	Energy difference	
$\hbar$	Reduced Plank constant	1.0545×10^{-34} Js(exact)
I	Light or laser intensity	
P	Laser power	
ρ	Density of resist radicals	
σ	Cross section	
σ_{abs}	Absorption Cross section	
σ_{sca}	Scattering Cross section	
σ_{ext}	Extintion Cross section	

Abstract

Metamaterials are part of an emerging research field with a broad range of useful potential applications in cross-disciplinary fields spanning material science, optics, industrial applications, and last but not least, sensing from environmental hazards to cancer cells. Metamaterials present particular features especially when they are fabricated as multi-stack layered systems or optical nano-cavities. In fact, due to the particular features presented by this kind of materials as strong self-collimation and canalization effects, extraordinary transmittance and plasmonic behavior, they open a very wide scenario of nano-technological applications. The application that has been addressed in this thesis exploits the interesting and intriguing features of metal/ insulator/ metal/insulator systems, so-called MIMIs, in optical nano-cavities configuration tailored to drastically improve the resolution of a generic Two Photon Direct Laser Writing (TP-DLW) lithography process. The enhanced technique covers an important role in nanotechnology and especially in new nanomaterials frontiers for the possible realization of polymeric, thus completely dielectric, metasurfaces. For these reasons, the driving concept of the work presented in this research activity is to carry out the entire cycle of realization of MIMI devices, passing from their design, optimization, fabrication and characterization. Following their realization, the optimized MIMI are used to enhance the TP-DLW process in order to fabricate hyper-resolute test samples as 1D gratings, 2D metasurfaces and 3D complex objects. Given its self-collimation optical features, the MIMI metamaterial is used for the characterization of the realized structures as well. A specific, noticeable case that has been addressed in this thesis is the realization of ultra-flat all-dielectric apochromatic broadband metalenses assisted, during the design, by a Deep Machine Learning algorithm and, for their fabrication, by the above mentioned enhanced TP-DLW process. Finally, the realized metalenses have been optically characterized in the visible spectrum ($300 - 1000\,nm$) confirming (as designed) fascinating features if compared with the already realized metalenses like the numerical aperture, extended focal length and depth of focus.
Chapter 1 introduces the main aspects of metamaterials, as well as, the isofrequency surface describing the dispersion relations of hyperbolic metamaterials, and different geometrical configurations that allow exploiting particular physical effects and behaviors in light-matter interaction. Then, stacked multi-layer materials and a particular family of those, εpsilon *N*ear *Z*ero, are presented. These metamaterials are a particular class of artificial optical structures consisting of a periodic arrangement of metallic and dielectric layers able to self-collimate and canalize light inside themselves. Finally, the chapter concludes with an overview of the plasmonic behavior in a simple

metal/insulator interface that produces surface plasmon polaritons. Then it considers the bulk plasmon polaritons in multi-stacked metamaterials and the gap surface plasmon in Fabry-Perot nano-cavities.
In Chapter 2, a simple and fast, yet robust, way to design metamaterials is evaluated as a function of their optical response and behavior. In fact, the first topic addressed in this chapter is ellipsometry and related advantages, to characterize nano-structures by retrieving the ellipsometric parameters Ψ and Δ, reflectance and transmittance and the complex refractive index $n - ik$. Then, the Transfer Matrix Method (TMM) has been detailed and used to code a homebuilt Matlab tool to predict the optical behavior as a function of the metamaterials design. On the same way, by using COMSOL Multiphysics, a Numerical Ellipsometer Analysis (NEA) has been realized. NEA covers the role of a robust tool to predict the optical response in much complex systems such as multi-layered materials with/without superstructures (gratings, holes, helices) placed above them. Some numerical simulations predicted by the NEA are experimentally validated by different cases with increasing system complexity. The plasmonic dispersion relations and the modal analysis have been addressed for dielectric cavities that support multi-spectral modes in the visible. Finally, in the last section, particular effects produced by MIMI cavities have been studied. Two key aspects related to the optical cavities are presented below. The first concerns the way they show hues / shades of color as a function of the cavity thickness and the involved material; the second one is a fast and effective way to identify the plasmons propagating inside these structures through the pseudo-dielectric function $< \tilde{\varepsilon} >$. These designed cavities present also particular effects like a large de-phasing well-known as Goos-Hänchen shift, that it is exploitable for extremely accurate sensing.
Chapter 3 begins by introducing the main concepts of one and two-photon lithography and describing the state of the art of the Two-Photon Direct Laser Writing (TP-DLW) process. Then, as reported in the previous chapter, it shows detailed aspects of optical-nano cavities and leverages on the MIMI properties and features to design an embedded device able to work at the two photon lithography process wavelength ($\lambda = 780nm$). The fabricated prototype is tested in terms of the incident beam waist modification by the evaluation of the Point Spread Function (PSF) reduction, measured by an homebuilt confocal setup equipped with a beam profiler. After its characterization, the MIMI device is used to realize 1D gratings compared with the ones fabricated through standard glass substrates. The reduction of 89% in height and 50% in width challenges our research product to reproduce the portrait *"The Lady with an Ermine"* by *Leonardo Da Vinci* that exhibits an high resolution level in terms of details and the nanoscale slicing in the 3D fabrication.
Chapter 4. The results obtained by the enhanced TP-DLW technique are exploited, in this chapter, to realize *all-dielectric apochromatic broadband "flatland" metalenses* with overall thickness less than 50nm. For their de facto two-dimensional nature, we call them "flatland" metalenses with the obvious reference to the famous Abbott's novel (*"Flatland: A Romance of Many*

Dimensions"). Next generation optics follow the trendsetting of miniaturized devices with extraordinary features as extended focal length and Depth of Focus (DOF), high Numerical Aperture and, last but not least, fast and easy way to produce them. In fact, this extremely flat design is the result of the novel two-photon direct laser writing (TP-DLW) process enhanced to hyper resolution performance by leveraging on the peculiar optical properties of our designed and developed ENZ metamaterials. Once fabricated, the characterization of the metalenses follows by means of a homebuilt setup equipped with beam-profiler and spectrometer. This measurement provided the characteristic values for these features like focal length $f = 1.14mm$, DOF in the range $|50 - 150|\mu m$ and the numerical aperture $NA = 0.087$.
In summary, the improved resolution of TP-DLW process presented in Chapter 3 is extremely significant for industrial applications in several fields such as anti-counterfeiting and flat optics, as shown in the last two Chapters of this Thesis work.

Introduzione

I metamateriali sono parte di una delle più recenti branche della ricerca emergente con un'ampia gamma di potenziali applicazioni utili in campi interdisciplinari che spaziano dalla scienza dei materiali, all'ottica, alle applicazioni industriali e, ultimo ma non meno importante, per il sensing e/o rilevamento dai rischi ambientali, generalmente inquinanti, sino alle cellule tumorali. I metamateriali presentano caratteristiche particolari, specialmente quando sono fabbricati come sistemi composti da strati multipli o nano cavità ottiche. Infatti, per le particolari caratteristiche presentate da questo tipo di materiali come gli elevati effetti di self-collimation e canalizzazione della luce, una straordinaria trasmittanza e comportamenti plasmonici aprono uno scenario molto ampio di applicazioni nanotecnologiche. L'applicazione principale affrontata in questa Tesi è relativa allo sfruttamento delle interessanti e intriganti caratteristiche dei sistemi metallo / isolante / metallo / isolante, noti anche con l'acronimo di MIMI, in configurazione di nano cavità ottiche realizzate su misura al fine di migliorare drasticamente la risoluzione del Processo di litografia con scrittura laser diretta a due fotoni (TP-DLW). La tecnica avanzata ricopre un ruolo importante nella nanotecnologia e nelle nuove frontiere dei nanomateriali, soprattutto per realizzare metasuperfici polimeriche, e quindi completamente dielettriche. Per questi motivi il concetto guida del lavoro presentato in questa attività di ricerca è quello di eseguire l'intero ciclo di realizzazione dei dispositivi MIMI, passando dalla loro progettazione, ottimizzazione, fabbricazione, quindi utilizzando questi dispositivi e il processo TP-DLW per la fabbricazione campioni di test risoluti come reticoli 1D, metasuperfici 2D e oggetti complessi 3D e, infine, caratterizzazione delle strutture prodotte. Un caso specifico notevole che è stato affrontato in questa tesi è la realizzazione di metalenses a banda larga apocromatiche completamente dielettriche ed ultra-piatte assistite, durante la progettazione, da un algoritmo di Deep Machine Learning e per la fabbricazione dal processo TP-DLW potenziato. Infine, le strutture realizzate sono state caratterizzate otticamente nello spettro visibile ($300 - 1000\,nm$) presentando caratteristiche affascinanti, se confrontate con le omologhe, come un'apertura numerica elevata, una lunghezza focale e una profondità di fuoco estese.
Il capitolo 1 introduce gli aspetti principali riguardanti i metamateriali, le superfici di isofrequenza che descrivono le relazioni di dispersione dei metamateriali iperbolici e diverse configurazioni geometriche che consentono di sfruttare particolari effetti fisici e comportamenti nell'interazione luce-materia. Quindi, vengono presentati i materiali multi-strato impilati e ne viene presentata una particolare famiglia/classe indicati come εpsilon *N*ear *Z*ero. Questi metamateriali portano alla fabbricazione di metamateriali con effetti particolari come l'auto-collimazione (self-collimation) e la canalizzazione della luce

al loro interno. Infine, il capitolo si conclude con una panoramica sul comportamento plasmonico partendo da una semplice interfaccia metallo/ isolante che produce polaritoni plasmonici di superficie, quindi si passa a considerare e studiare i polaritoni plasmonici di volume in metamateriali multi-stack e il plasmone di superficie in gap (cavitàă) nelle nano-cavitàă alla Fabry-Pèrot.
Nel Capitolo 2 viene valutato un modo semplice, veloce ma al tempo stesso robusto per progettare metamateriali in funzione della loro risposta ottica e del loro comportamento. Infatti il primo argomento trattato in questo capitolo è l'ellissometria ed i suoi vantaggi per caratterizzare nanostrutture acquisendo così i parametri ellissometrici *Psi* e *Delta*, la riflettanza R e la transmittanza T ed anche l'indice di rifrazione complesso $n - ik$. Quindi è stato approfondito il metodo delle matrici di trasferimento denominato TMM, dall'inglese Transfer Matrix Method, che successivamente è stato utilizzato per programmare uno strumento numerico nel linguaggio Matlab per prevedere il comportamento ottico in funzione del design e composizione dei metamateriali. Allo stesso modo, utilizzando COMSOL Multiphysics, è stata realizzata un'analisi numerica ellissometrica NEA, sempre dall'inglese Numeric Ellipsometer Analysis. Il NEA ricopre il ruolo di uno strumento robusto per prevedere la risposta ottica dei metamateriali con/senza sovrastrutture poste al di sopra di essi. Le simulazioni numeriche fatte con tale strumento considerando diversi casi ed aumentando la complessitàă del sistema sono state validate sperimentalmente e tali risultati sono riportati in questo capitolo. Le relazioni di dispersione plasmonica e l'analisi modale sono state valutate per le cavitàă dielettriche che supportano più modi nello spettro visibile. Infine, nell'ultima sezione sono stati studiati gli effetti particolari prodotti dalle cavitàă MIMI. In seguito vengono presentati due aspetti chiave legati il alle cavitàă ottiche, il primo riguarda come esse producono tonalitàă/ sfumature di colore in funzione dello spessore della cavitàă stessa e del materiale coinvolto; il secondo invece è un modo veloce ed efficace per individuare i plasmoni propagatisi all'interno di queste strutture attraverso la funzione pseudo dielettrica $< \tilde{\varepsilon} >$. Queste cavità progettate presentano anche effetti particolari come un alto sfasamento noto come Goos-Hänchen shift che è sfruttabile per lo sviluppo di sensori estremamente accurati.
Il capitolo 3 inizia introducendo i concetti principali della litografia a uno e due fotoni e lo stato dell'arte in merito alla tecnica di TP-DLW. Fatta questa prima introduzione si riprendono gli aspetti già trattati in dettaglio nel precedente e si utilizzano le proprietà e le caratteristiche dei MIMI per progettare un dispositivo integrato in grado di lavorare alla lunghezza d'onda del processo di litografia a due fotoni ($\lambda = 780nm$). Quindi, il prototipo fabbricato è stato testato in termini di come si modifica il beam waist della luce incidente quando attraversa tale substrato, tale valutazione è stata fatta considerando la riduzione della Point Spread Function (PSF) misurata grazie a un setup confocale auto-costruito dotato di beam profiler. Dopo la caratterizzazione tale dispositivo è stato utilizzato per produrre reticoli 1D al fine di paragonare il risultato ottenuto con quelli fabbricati su un substrato di vetro classico. La riduzione del 89% in altezza e del 50% in larghezza inducono la nostra ricerca ad un ulteriore test la riproduzione del ritratto *"La Dama con l'ermellino"* di *Leonardo Da Vinci* che mostra un alto livello di risoluzione

in termini di dettagli e di parametri usabili durante la fabbricazione 3D alla nanoscala come uno slicing di $20nm$.
Nel Capitolo 4 vengono illustrati i risultati ottenuti tramite il miglioramento in termini di risoluzione dalla tecnica di TP-DLW e come questi vengono sfruttati per realizzare metalenti. Queste sono completamente dielettriche, apocromatiche hanno il vantaggio di poter essere usate in una banda spettrale larga e sono caratterizzate da dimensioni in z di poche decine di nanometri, non più di $50nm$. Questo ci ha spinto a denominarle come "Flatland" in omaggio al noto racconto di Abbott, *"Flatland: A Romance of Many Dimensions"*. La tendenza seguita dell'ottica di oggi giorno e del futuro è rappresentata sempre più dai dispositivi miniaturizzati con caratteristiche incredibili come la lunghezza focale estesa, la profonditàă di fuoco (DOF), un'elevata apertura numerica e anche un modo semplice e veloce per produrli. Infatti questo design estremamente piatto è il risultato di un nuovo processo di scrittura laser diretta a due fotoni (TP-DLW) rivisitato in termini di prestazioni e di ultra risoluzione sfruttando le proprietàă ottiche peculiari dei metamateriali εNZ. Lo scopo di questo capitolo è quello di promuovere la progettazione delle metalenti mediante un design inverso condotto attraverso deep machine learning e la fabbricazione attraverso il dispositivo MIMI al fine di aumentare la risoluzione del processo di produzione. Una volta fabbricate le metalenti queste vengono caratterizzate utilizzando un setup ottico autocostruito dotato di beam-profiler e spettrometro. La lunghezza focale risulta pari a $f = 1.14mm$, il DOF è compreso tra $|50 - 150|\ \mu m$ e l'apertura numerica è pari a $NA = 0.087$. In conclusione l'alta risoluzione del processo TP-DLW, migliorata per mezzo di un substrato composto da metamateriale (come riportato nel Capitolo 3), è estremamente importante per applicazioni industriali in diversi campi come l'anti-contraffazione e l'ottica ultra-piatta come mostrato nei capitoli finali di questo lavoro di tesi.

Chapter 1

Main theoretical aspects

In this Chapter, I propose to introduce and illustrate the main theoretical concerns met in this Doctoral Thesis. I start by introducing metamaterials and peculiar aspects of these systems. Then, I focalize the attention on a particular class of metamaterials called Hyperbolic MetaMaterials (HMM) and the Epsilon Near Zero (εNZ) condition. Finally, I engage the physical aspects related to this kind of materials and explain in detail the dispersion relations about the Surface Plasmon Polaritons (SPPs), Bulk Plasmon Polaritons (BPPs), and Gap Plasmon Polaritons (GSPs), related to metal/dielectric interfaces within the εNZ metamaterials presented as stack of layers and optical nano-cavities.

1.1 Metamaterials: general point of view

A metamaterial (from the Greek word $\mu\epsilon\tau\alpha$ meta, meaning "beyond" and the Latin word materia, meaning "matter" or "material") is a material engineered to have a property that is not found in naturally occurring materials.[1–3] They are made by assemblies of multiple elements typically comprising basic materials like metals and plastics. The materials are usually arranged in repeating patterns, at scales that are much smaller than the typical length scales of the phenomena they influence. Metamaterials derive their extraordinary features not from the properties of the basic materials of which they are made, but from the way these materials are combined in the newly designed structures. Their precise shape, geometry, size, orientation and arrangement gives them their smart properties capable of manipulating electromagnetic waves: by blocking, absorbing, enhancing, or bending waves, to achieve benefits that go beyond what is possible with conventional materials. Appropriately designed metamaterials can affect waves of electromagnetic radiation or sound in a manner not observed in bulk materials.[4, 5] Those that exhibit a negative index of refraction for particular wavelengths have attracted significant research.[6–8] These materials are known as negative-index metamaterials. Potential applications of metamaterials are diverse and include optical filters, medical devices, remote aerospace applications, sensor detection and infrastructure monitoring, smart solar power management, crowd control, radomes, high-frequency battlefield communication and lenses for high-gain antennas, improving ultrasonic sensors, and even shielding structures from earthquakes.[9–11] Metamaterials offer the potential to create superlenses. Such a lens could allow imaging below the diffraction limit that is

the minimum resolution that can be achieved by conventional glass lenses. A form of 'invisibility' was demonstrated using gradient-index materials. Acoustic and seismic metamaterials are also research areas.[9, 12] Metamaterial research is interdisciplinary and involves such fields as electrical engineering, electromagnetics, classical optics, solid state physics, microwave and antenna engineering, optoelectronics, material sciences, nanoscience and semiconductor engineering.[5] An electromagnetic metamaterial affects electromagnetic waves that impinge on it or interact with its structural features. To behave as a homogeneous material, accurately described by an effective refractive index, its features must be much smaller than the wavelength of the impinging light. For microwave radiation, the features are on the order of millimeters. Microwave frequency metamaterials are usually constructed as arrays of electrically conductive elements (such as loops of wire) that have suitable inductive and capacitive characteristics. A typology of microwave metamaterial uses the split-ring resonator as unit cell.[7, 8] Photonic metamaterials, at nanometer scale, manipulate light at optical frequencies. To date, subwavelength structures have shown only few, questionable, results at visible wavelengths.[7, 8] Photonic crystals and frequency-selective surfaces such as diffraction gratings, dielectric mirrors and optical coatings exhibit similarities to subwavelength structured metamaterials. However, these are usually considered distinct from subwavelength structures, as their features are structured for the wavelength at which they work and thus cannot be approximated as a homogeneous material. However, material structures such as photonic crystals are effective in the visible light spectrum. The middle of the visible spectrum has a wavelength of approximately 560 nm (for sunlight). Photonic crystal structures have typical length scales that are generally half this size or smaller, that is $< 280\,nm$. Plasmonic metamaterials utilize surface plasmons, which are packets of electrical charge that collectively oscillate at the surfaces of metals at optical frequencies. The plasmonic metamaterials behavior will be detailed in section 1.3. Frequency selective surfaces (FSS) can exhibit subwavelength characteristics and are known as artificial magnetic conductors (AMC) or High Impedance Surfaces (HIS). FSS display inductive and capacitive characteristics that are directly related to their subwavelength structure [13]. Almost all materials encountered in optics, such as glass or water, have positive values for both permittivity ε and permeability μ. However, metals such as silver and gold have negative permittivity at shorter wavelengths. A material such as a surface plasmon that has either (but not both) ε or μ negative is often opaque to electromagnetic radiation. However, anisotropic materials with only negative permittivity can produce negative refraction due to chirality. Although the optical properties of a transparent material are fully specified by the parameters ε_r and μ_r, refractive index n is often used in practice, which can be determined from $n = \pm\sqrt{\varepsilon_r \mu_r}$. All known non-metamaterial transparent materials possess positive ε_r and μ_r. By convention the positive square root is used for n. However, some engineered metamaterials have ε_r and $\mu_r < 0$. Because the product $\varepsilon_r \mu_r$ is positive, n is real. Under such circumstances, it is necessary to take the negative square root for n. The foregoing considerations are simplistic for actual materials, which must have complex-valued ε_r and μ_r. The real

parts of both ε_r and μ_r do not have to be negative for a passive material to display negative refraction. Metamaterials with negative n have numerous interesting properties:[6, 14] Snell's law ($n_1 \sin\theta_1 = n_2 \sin\theta_2$), but because n_2 is negative, the rays are refracted on the same side of the normal on entering the material. Cherenkov radiation points the other way. The time-averaged Poynting vector is antiparallel to phase velocity. However, for waves (energy) to propagate, a $-\mu$ must be paired with a $-\varepsilon$ in order to satisfy the wave number dependence on the material parameters $kc = \omega\sqrt{\mu\epsilon}$. Negative index of refraction derives mathematically from the vector triplet **E**, **H** and **k**. For plane waves propagating in electromagnetic metamaterials, the electric field, magnetic field and wave vector follow a left-hand rule, the reverse of the behavior of conventional optical materials.

1.1.1 Hyperbolic Metamaterials

Hyperbolic Metamaterials raise significant interest in the scientific community, as "one of the most unusual classes of electromagnetic metamaterials" [15]. They represent a special category of systems able to present very particular behavior when impinged by an electromagnetic wave. They can be employed to realize useful functionalities in emerging meta-devices based on light. They show hyperbolic (or indefinite) dispersion, which originates from one of the principal components of their electric or magnetic effective tensor having the opposite sign to the other two principal components. Such anisotropic structured materials exhibit distinctive properties, including strong enhancement of spontaneous emission, diverging density of states, negative refraction and enhanced super-lensing effects. Initial studies of metamaterials concentrated on structures that possess both negative permittivity and negative permeability (known as double-negative media), as such structures are highly promising for subwavelength optics because they exhibit negative refraction [8]. In recent years, the focus of metamaterial research has shifted towards active and tunable metamaterials, as well as simplifying structures while preserving many of their unusual properties and functionalities. One class of metamaterials is highly anisotropic media that have hyperbolic (or indefinite) dispersion [16], as determined by their effective electric and/or magnetic tensors. Such metamaterials represent the ultra-anisotropic limit of traditional uniaxial crystals, and one of the principal components of either their permittivity or permeability tensors is opposite in sign to the other two principal components (as we write above). We report here the permittivity and permeability tensor[17]: $\varepsilon_{xx} = \varepsilon_{yy} = \varepsilon_{\parallel}$ and $\varepsilon_{zz} = \varepsilon_{\perp}$ $\mu_{xx} = \mu_{yy} = \mu_{\parallel}$ and $\mu_{zz} = \mu_{\perp}$ the other components are equal to **zero**. Here, the subscripts $\parallel$ and $\perp$ indicate components parallel and perpendicular to the anisotropy axis, respectively. In this section, we focus on electric hyperbolic structures with $\hat{\mu} = \mu_{\parallel} > 0$ and either $\varepsilon_{\parallel} < 0$ and $\varepsilon_{\perp} > 0$ or $\varepsilon_{\parallel} < 0$ and $\varepsilon_{\perp} < 0$. Their unique properties stem from the isofrequency surface of extraordinary (transverse magnetic polarized) waves (Fig. 1.1), which is given by

$$\frac{K_x^2 + K_y^2}{\varepsilon_{\perp}} + \frac{K_z^2}{\varepsilon_{\parallel}} = \left(\frac{\omega}{c}\right)^2 \tag{1.1}$$

Here, k_x , k_y and k_z are respectively the x, y and z components of the wave vector, ω is the wave frequency and c is the speed of light.

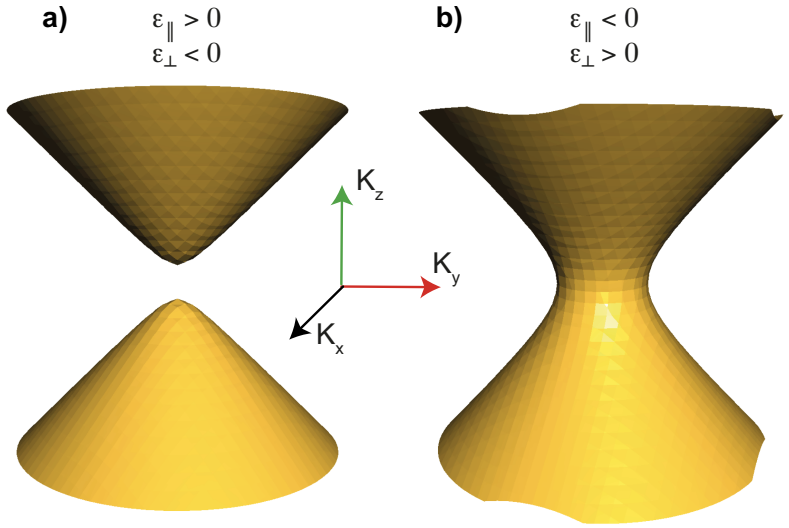

FIGURE 1.1: Isofrequency surfaces the dispersion relation of hyperbolic metamaterials. a,b Isofrequency surfaces given by $\omega(k)$ = constant for $\varepsilon_{zz} = \varepsilon_{\perp} < 0$, $\varepsilon_{xx} = \varepsilon_{yy} = \varepsilon_{\parallel} > 0$, this is denoted as Type I (a) and $\varepsilon_{\perp} > 0$, $\varepsilon_{\parallel} < 0$, the Type II (b).

It is considerably easier to produce hyperbolic structures than double-negative media, as the only essential criterion for hyperbolic structures is that the motion of free electrons be constrained in one or two spatial directions. Such structures were first experimentally demonstrated in a magnetized plasma in 1969 [18]. A few natural materials, including bismuth and graphite, exhibit hyperbolic properties in certain spectral ranges [19]. How to exploit these kind of metamaterials is reported in our general point of view. The hyperbolic metamaterials have been divided in two main class strongly connected to the isofrenquecy surfaces and their anisotropy, the first is named "type I" and is denoted from a dielectric behavior in the xy plane and a metal one in the orthogonal plane (hyperboloid two fold, $\varepsilon_{\parallel} > 0$ $\varepsilon_{\perp} < 0$) Fig.1.1a and the "type II" where the dielectric behavior is in the bulk and the metal one is in the plane, (hyperboloid one fold, $\varepsilon_{\parallel} < 0$ $\varepsilon_{\perp} > 0$) Fig.1.1b. Now, we want underline about different ways to design HMMs. In metals, the real part of the dielectric function is negative below the plasma frequency because the polarization response of free moving electrons is in the opposite direction to the electric field. In the hyperbolic regime, the components of the dielectric tensor are negative in only one or two spatial directions. This can be achieved by restricting free-electron motion to these directions. Hence, the most common realization of hyperbolic metamaterials is layered metal-dielectric structures (Indeed, we will focus our attention on these). Other metamaterials are fabricated as hyper-lenses, as multilayer fishnet, as nanorod arrays, as arrays of metal-dielectric nanopyramids and graphene metamaterials, just to name a few. Each possible systems are reported in Fig. 1.2.

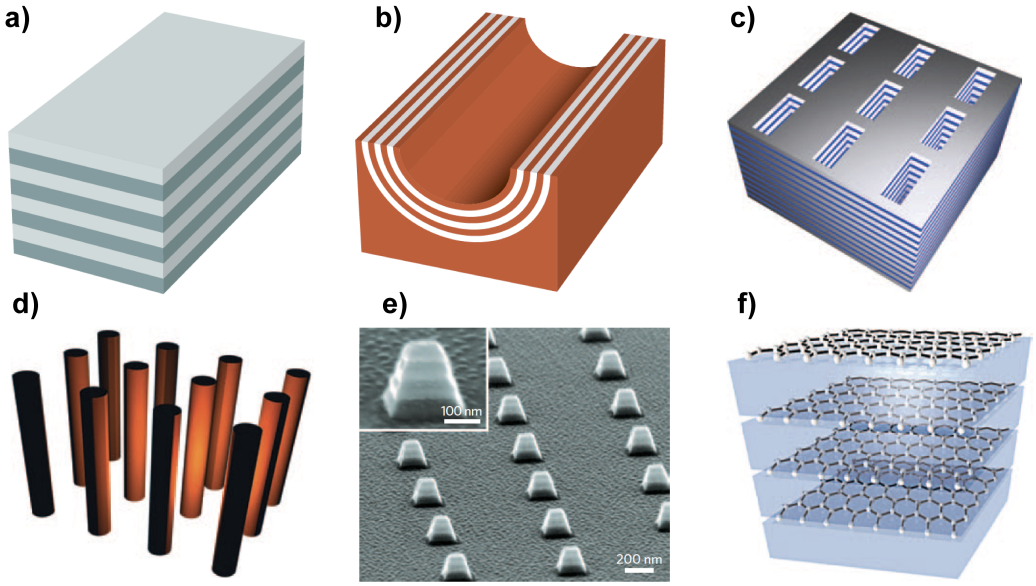

FIGURE 1.2: Examples of hyperbolic metamaterials. a) Layered metal-dielectric structure; b) hyper-lens; c) multilayer fishnet; d) nanorod arrays; e) arrays of metal-dielectric nanopyramids; f) graphene metamaterials. Reproduced with permission from [15].

1.1.2 Layered metal-dielectric structures

An example of layered metal-dielectric structure is shown in Fig. 1.2a. The components of the effective dielectric tensor parallel $\varepsilon_{\parallel}$ and perpendicular $\varepsilon_{\perp}$ to the anisotropy axis are given by. [20]

$$\tilde{\varepsilon}_{\parallel} = \frac{\tilde{\varepsilon}_m d_m + \tilde{\varepsilon}_d d_d}{d_m d_d}, \tilde{\varepsilon}_{\perp} = \frac{\tilde{\varepsilon}_d \tilde{\varepsilon}_m (d_m + d_d)}{\tilde{\varepsilon}_m d_d + \tilde{\varepsilon}_d d_m} \tag{1.2}$$

where d_m (d_d) is the thickness and ε_m (ε_d) is the dielectric constant of the metallic (dielectric) component, (see the Appendix A). By tuning these parameters such that $\varepsilon_{\parallel}\varepsilon_{\perp} < 0$, one can attain the hyperbolic regime. The effective medium approximation given by equation (1.2) is valid in the long-wavelength limit, namely, when the variation of the electromagnetic field over one period of the structure is small. However, the excitation of surface plasmon polaritons at the metal-dielectric interfaces causes the field to vary significantly on the scale of one period, even when the vacuum wavelength is much larger than the period. Hence, the approximation given by equation (1.2) may not be valid in certain spectral ranges. Plasmonic modes may have more complex shaped isofrequency contours that are neither elliptic or hyperbolic. This leads to both negatively and positively refracted beams being produced by light scattered at the metamaterial interface [20, 21]. Such effects can be described by using the effective tensor with spatial dispersion, that is, ε depends on the mode wave vector[22, 23]. Spatial dispersion implies a nonlocal response in real space, such that the electric field at one point in space induces polarization at another point. To the best of our knowledge, the first experimental demonstration of a layered

hyperbolic metamaterial was a hyper-lens. Negative refraction and hyperbolic dispersion were demonstrated in the mid-infrared region using a structure consisting of doped InGaAs (Indium Gallium Arsenide) and intrinsic AlInAs (Aluminium Indium Arsenide) layers [24]. Subsequently, numerous hyperbolic metamaterials have been demonstrated that consist of different metal/dielectric pairs. Suitable materials for layered hyperbolic structures have been evaluated in detail [25]. Metallic systems are generally considered preferable for optical frequencies, whereas semiconductors are considered to be optimal for lower frequencies, namely in the terahertz and nearinfrared regions [26]. Typically, the hyperbolic regime with $Re(\varepsilon_{\perp}) < 0$ is realized in a metallic system (Fig. 1.1b) [27]. An inherent problem of metal-based structures is Joule losses. One way to mitigate this problem is to use active media, so that the losses are compensated by the gain of the active media[28, 29]. An alternative strategy involves using unconventional plasmonic materials that have low losses in specific frequency ranges [30, 31]. Metal-dielectric structures may be naturally extended to the so called hyper-lens (Fig. 1.2b), which consists of a hyperbolic metamaterial on a curved substrate [32, 33]. As hyperbolic metamaterials support large propagating wave vectors, a hyper-lens may magnify subdiffraction-limited objects in the far field [34]. It is easier to realize a super-lens using planar plasmonic structures [35].

1.1.3 ϵNear Zero (and Pole) Metamaterials

An important "subclass" of HMM is represented by the epsilon-near-zero (εEZ) metamaterials. They are not different in fabrication when compared with the systems depicted in Fig. 1.2a; in fact, the most common are the layered ones. As the name suggest this kind of metamaterials are characterized by the permittivity assuming near zero values at one or more wavelengths. Due to their unique electromagnetic features, these metamaterials are of great importance in many applications at microwave and optical frequencies [36–41]. In fact, it is possible to obtain ϵNZ metamaterials at a single operating frequency. However, regarding practical implementations, ϵEZ metamaterials over a broadband operating frequency range are required, which is a challenge in both science and technology. In order to account this challenge, an efficient effective-medium theory (EMT) code is exploited to evaluate when we are in presence of an ϵEZ and which the operative wavelengths are. Our code allows evaluating both ε_1 and ε_2 permittivities (real and the imaginary parts, respectively) as a function of the layer thickness of the involved materials and the optical constants. According to the Maxwell-Garnett approximation [42, 43] for a N-layered system, we can calculate the effective complex dielectric constant $\tilde{\varepsilon}_{eff}$ using the following equation:

$$\frac{\tilde{\varepsilon}_{eff} - \varepsilon_1}{\tilde{\varepsilon}_{eff} + 2\varepsilon_1} = (1 - f_1)\frac{\varepsilon_2 - \varepsilon_1}{\varepsilon_2 + 2\varepsilon_1} \tag{1.3}$$

Where ε_1 and ε_2 represent the two phases involved in the system, in our case metal and dielectric material, whereas f is the volume fraction. When

considering a N-layerd structure, where the unit cell is a metal-dielectric bi-layer, f is calculated as the ration of the two layers thickness. The ε Near Zero systems exhibit outstanding quality as the non phase change (zero delay) of the impinging wave [44] and due to the $\varepsilon_e = 0$ the system is lossless [45, 46]. Here, in Fig. 1.3, the calculation is reported of the $\tilde{\varepsilon}_{eff}$ using the EMT developed in Matlab, by ourselves, for some metal-dielectric structures. We consider a ε Near Zero (and Pole) metamaterial constituted from Ag/Al_2O_3, Au/ITO, Ag/ITO, and Ag/AZO just to name a few, ITO stands for Indium-Tin-Oxide and AZO stands for Zincum-Oxide doped with the 2% in weight of Al_2O_3. An εNear Zero and Pole metamaterials as shown in the figure 1.3, present both type of HMM Type I and Type II, in fact, ε_e to be zero the $\varepsilon_{\parallel}$ and the $\varepsilon_{\perp}$ have to cross passing from $\varepsilon_{\parallel} > 0$ $\varepsilon_{\perp} > 0$ to $\varepsilon_{\parallel} < 0$ $\varepsilon_{\perp} > 0$, respectively, as is shown in the Figs. 1.3a,c,e . This kind of metamaterials give the possibility to canalize light within[47]. The self canalization and the high collimation effects represent two main aspects of this research dissertation and they are largely explained and exploited in the following sections and in the next Chapters.

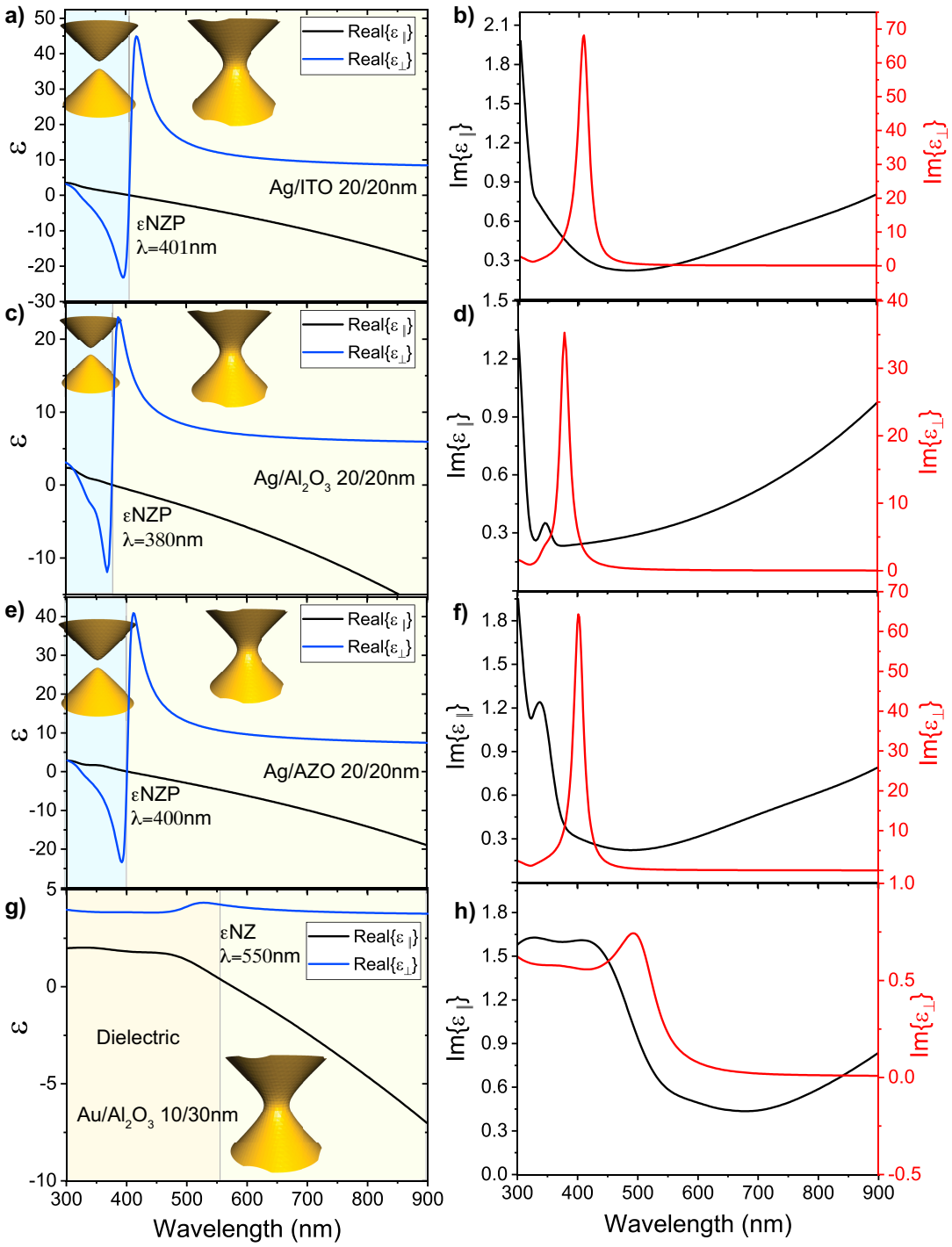

FIGURE 1.3: Figures a,c,e,f) show the behavior of the real part of $\varepsilon_{\parallel}$ and $\varepsilon_{\perp}$ calculated using the EMT. In the insets for each figure is reported the hyperbolic anisotropy sketch, the blurry blu area denotes the HMM type 1 and the blur yellow area denotes the HMM type 2. The figures b,d,f,h) show the behavior of the related imaginary part of $\varepsilon_{\parallel}$ and $\varepsilon_{\perp}$ also calculated using the EMT. The analyzed ε Near Zero and Pole HMM are the following, from the top to the bottom, Ag/ITO 20/20 nm, Ag/Al_2O_3 20/20 nm, Ag/AZO 20/20 nm and finally only an εNZ constituted by Au/Al_2O_3 10/30 nm.

1.2 Plasmons at metal/ dielectric interface, in metamaterials and optical nano-cavities

An important role in this research framework is covered by the Surface Plasmon Polaritons (SPPs), the Bulk Plasmons Polaritons (BPPs), and the Gap Surface Plasmons (GSPs) that are generated in presence of a metal-dielectric interface in εNZ(P) or general hyperbolic metamaterials [48]. Before explaining what happens inside metamaterials it is important to spend few words to better understand what is a plasmons and the difference that occurs between SPPs, BPPs and GSPs. Firstly, it is important to introduce a polariton that is an electromagnetic (EM) wave coupled to a polarization excitation in matter. When this coupled excitation is bound to the interface between two media it is called a surface polariton [49, 50]. A surface polariton is an evanescent electromagnetic wave that propagates along the interface and with an amplitude decaying exponentially into the two media. Surface polaritons are named surface plasmon polaritons (SPPs) when one of the media is a metal and the other a dielectric. SPPs are modes bound to and propagating along a metal-dielectric interface consisting of transverse magnetic EM waves (electric field oriented along the y-axis) that decay exponentially into both the metal and dielectric media (Figure 1.4). The tangential field components (along the z-

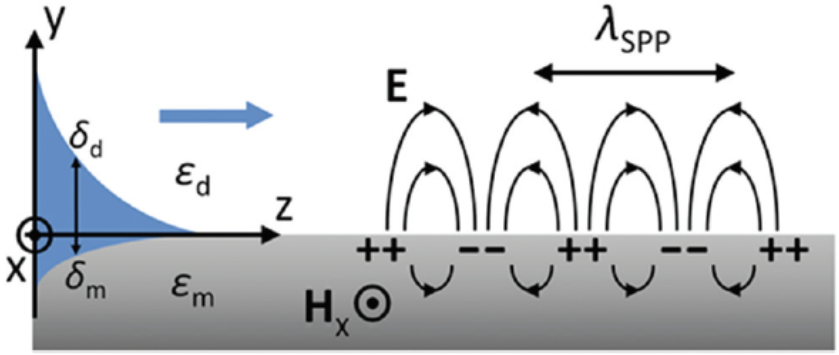

FIGURE 1.4: Sketch of the field components of a SPP supported by a metal-dielectric interface. The mode is transverse magnetic, exhibiting electric field components normal to the interface ($y-axis$) and along the propagation direction ($z-axis$). The mode profile (blue) represents the magnitude of the corresponding magnetic field, itself oriented along the $x-axis$, as a function of y. Picture readapted with permission from [50]

axis) are continuous across the interface and correspond to the wavevector K_z such that the SPP electric fields can be written as follows:

$$E(y>0) = \begin{pmatrix} 0 \\ E_y^d \\ E_z^0 \end{pmatrix} e^{i(K_{spp}z - wt)} e^{-y\sqrt{K_{spp}^2 - \varepsilon_d k_0^2}} \tag{1.4}$$

$$E(y<0) = \begin{pmatrix} 0 \\ E_y^m \\ E_z^0 \end{pmatrix} e^{i(K_{spp}z-wt)} e^{-y\sqrt{K_{spp}^2-\varepsilon_m k_0^2}} \tag{1.5}$$

where E_z^0 and $E_y^{d(m)}$ are the amplitudes of the electric field components in the dielectric (metal) medium, ε_m and ε_d are the dielectric constants of the metal and dielectric, respectively, K_0 is the free-space light wavenumber ($K_0 = \omega/c = 2\pi/\lambda$, where ω is the angular frequency and λ is the light wavelength in free space) and the SPP propagation constant, $K_SPP = K_z$, is governed by the SPP dispersion relation, $K_SPP(\omega)$, yet to be determined. The SPP EM waves are coupled to the free electrons of the metal surface and give rise to collectively oscillating charge separations that correspond to the EM fields. Since the electric field components should satisfy Coulomb's law $\nabla E = 0$, transverse electric EM waves (electric field oriented along the $x-axis$) cannot couple to the tangential electron oscillations along the z-axis at the metal surface and form SPPs. The normal field components (along the $y-axis$) can then be written in terms of the mutual tangential component:

$$E_y^d = \frac{iK_{spp}}{\sqrt{K_{SPP}^2 - \varepsilon_d K_0^2}} E_z^0 \tag{1.6}$$

$$E_y^m = \frac{iK_{spp}}{\sqrt{K_{SPP}^2 - \varepsilon_m K_0^2}} E_z^0 \tag{1.7}$$

By using the boundary condition $\varepsilon_d E_x^d = \varepsilon_m E_x^m$, the SPP dispersion relation can be found:

$$K_{SPP} = \frac{\omega}{c}\sqrt{\frac{\varepsilon_m \varepsilon_d}{\varepsilon_m + \varepsilon_d}} \tag{1.8}$$

where $\varepsilon_m(\omega)$ and $\varepsilon_d(\omega)$ denote the individual metal and dielectric material dispersions respectively, and it is evident that $K_{SPP}(\omega) >> K_0(\omega)$ for EM waves of the same frequency propagating in the dielectric. The SPP propagation constant relates to the effective refractive index of the SPP mode by $N_{eff} = K_{SPP}\lambda/(2\pi)$, with the real and imaginary parts determining the SPP wavelength, $\lambda SPP = 2\pi/Re\{K_{SPP}\}$, and the intensity-based propagation length, $LSPP = 1/Im\{2K_{SPP}\}$. The Fig. 1.5 shows the dispersion relation for the plasmonic modes of the Ag layer, in fact the silver layer for the low frequency, presents a SPP and for the other one it presents the bulk modes. It is important to remark that when we have bulk modes they become guided modes [51]. The most used dispersion relation for a simple metal-dielectric system has been analyzed, metamaterials, as well known, are composed by a stack of metal/dielectric layers with same or different thicknesses. On this way, the dispersion relations take different forms if they are referred to the HMM or structures that are made of metal- insulator- metal (MIM) layer sequences with the insulator thicker than the metal layers. In case of HMM or

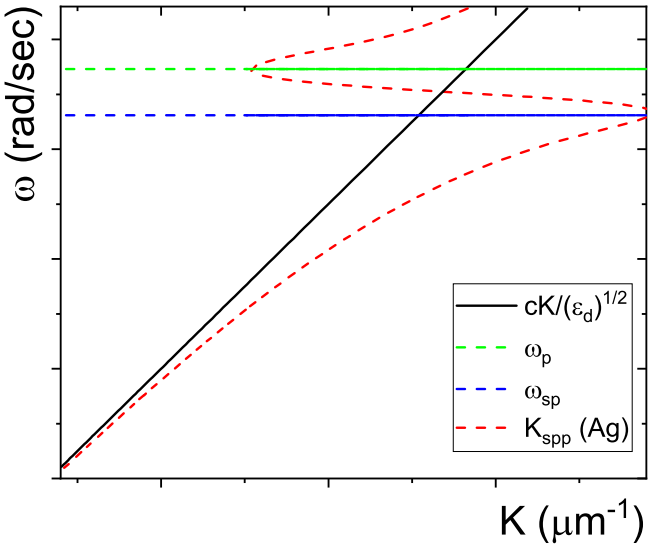

FIGURE 1.5: Dispersion relation calculated for a plasmon thin Ag layer according with the K_{SPP} relation (Eq. 1.12). $cK/(\varepsilon d)^{1/2}$ represents the light line, ω_p is the plasma resonance and the ω_{sp} is the surface plasmon resonance.

a stack of metal/insulator layer the dispersion relation is the following:

$$K^0_{BPP} = K_0 \sqrt{\frac{\varepsilon_m \varepsilon_d (t_d + t_m))}{t_d \varepsilon_m + t_m \varepsilon_d}} \tag{1.9}$$

where t_d and t_m are the dielectric and metal thickness of the involved layers. This equation can also written considering the diffraction order produces by the metamaterials or a superstructure (gratings, metagratings or for example helices) placed above as studied and detailed in [52, 53], the equation becomes:

$$K^n_{BPP} = K_0 \sqrt{\varepsilon_d \left[\frac{\lambda^2}{\pi t_d t_m}\right] \frac{\varepsilon_d}{\varepsilon_m}} \tag{1.10}$$

Optical nano-cavities like MIMs or MIMIs also present a very peculiar dispersion relation. In case of these systems, the dispersion relation plays a fundamental role especially to comprehend the strong coupling interaction between the multi-layered material and the impinging wave. Past studies demonstrate that metal-insulator-metal (MIM) systems present anomalous behavior for both polarizations (TE and TM) [50, 54–61]. MIMs present GSPs for the s-pol (TE) and SPP for the p-pol (TM), they occur because the system presents a dispersion relation that allows to guide and propagate plasmon polaritons inside the bulk dielectric cavity as a LSP (local surface plasmon) for the TE polarization and to propagate by exploiting the surface the SPP produced from the TM polarization. Nevertheless, The MIMs present

a peculiar optical behavior by selectively transmitting light in the UV-VIS-NIR spectrum. This particular feature is achieved without using diffraction gratings or other super-structures to couple in the impinging wavevector. In presence of an optical cavity, confined modes satisfy the general Fabry-Perot (FP) condition $\beta t_{cav} = m\pi - \phi$, where β is the complex wave-vector of the lightwave propagating within the cavity, m identifies the given mode generated inside the cavity, ϕ is the reflection dephase angle and t_{cav} is the cavity thickness. In this case, the FP relation, applied to a nano-cavitiy confined by metal layers,[62] is modified as in the following $\beta_{gsp} t_{cav} = m\pi - \phi$, where β_{gsp} is calculated by considering the dispersion relation of a general MIM structure. The dispersion relation involving the wave vector β can be written as:

$$tanh\left[\frac{\alpha_d t_{cav}}{2}\right] = -\frac{\varepsilon_d \alpha_m}{\varepsilon_m \alpha_d} \tag{1.11}$$

Here $\varepsilon_{m,d}$ are the dielectric constants of the metal and dielectric materials, respectively whereas t_{cav} is the thickness of the insulator cavity and $\alpha_{m,d} = \sqrt{\beta_{gsp}^2 - \varepsilon_{m,d} k_0^2}$. By solving the dispersion relation with the approximation $tanh(x) \approx 1 - 2e^{2x}$, it is possible to find the following expression for β_{gsp} [50, 54, 63]:

$$\beta_{gsp} = \beta_{spp}\sqrt{1 - \frac{4\varepsilon_d \varepsilon_m}{\varepsilon_m^2 - \varepsilon_d^2} exp(-\alpha_1 t_{cav})} \tag{1.12}$$

with

$$\alpha_1 = \alpha_0\sqrt{1 + \frac{4\varepsilon_m^2}{\varepsilon_m^2 - \varepsilon_d^2} exp(-\alpha_0 t_{cav})} \tag{1.13}$$

and

$$\alpha_0 = \sqrt{\beta_{spp}^2 - \varepsilon_d k_0^2} = \frac{k_0 \varepsilon_d}{\sqrt{-\varepsilon_m - \varepsilon_d}} \tag{1.14}$$

The value of β_{spp} is calculated as: Also in this case we can write the following dispersion relation for the surface plasmon polaritons (equal to Eq. 1.12):

$$\beta_{spp} = k_0\sqrt{\frac{\varepsilon_m \varepsilon_d}{\varepsilon_m + \varepsilon_d}} \tag{1.15}$$

The presented dispersion relations cover a fundamental role in the next Chapters and sections to calculate and evaluate the plasmonic behavior of the systems that will be addressed.

1.3 Subwavelength metamaterials for imaging and super-lenses

As above mentioned and demonstrated by Sir. J. B. Pendry, with metamaterials is possible to realize subwavelength imaging and superlenses. In particular, because of the very large components of their permittivity tensors, hyperbolic media showing nearly flat iso-frequency contours are beneficial for transferring the near field of a point source. Indeed, if a point source is

placed near a slab made from such a medium, the emitted evanescent waves with arbitrarily large in-plane wave vectors can excite propagating modes in the slab, which will transfer the near-field information to the opposite interface of the slab. The realization of such a set-up using different types of hyperbolic media has been suggested. One of the most promising applications of hyperbolic metamaterials is the hyper-lens. It permits the near field of an object (either an emitter or a scatterer) to be transformed into a far-field image, which can be processed by conventional optical devices. To explain the operation principle of the hyper-lens, it is instructive to assume cylindrical symmetry and to expand the electromagnetic field as a series of waves with fixed angular momentum m. As the angular momentum conservation law imposes the constant value of $m = k_\theta r$, the wave vector k_θ should increase as $1/r$ with decreasing radius. Thus, the vacuum dispersion relation $k_r^2 + k_\theta^2 = \omega^2/c^2$ensures that k_r will be imaginary for small radii, and hence the mode will be evanescent. However, for a hyperbolic medium, the dispersion relation becomes:

$$\frac{k_r^2}{\varepsilon_\theta} - \frac{k_\theta^2}{\varepsilon_r} = \left(\frac{\omega}{c}\right)^2 \tag{1.16}$$

This equation states that for any value of the tangential wave vector k_θ, the component k_r will be real; that is, modes with an arbitrarily large angular momentum m will propagate for an arbitrary radius r. The conventional hyper-lens is a hollow cylinder made from a hyperbolic medium (Fig. 1.2b). Evanescent modes with high angular momenta are radiated by an object inside the cylinder, and they carry near-field information about the object. They excite propagating modes inside the hyper-lens, which can be used to transfer the near-field information to the far-field region of the outer radius of the cylinder. The resolution Δ_{res} of such a device can be estimated using $\Delta_{res} = (R_{in}/R_{out})\lambda$, where R_{in} and R_{out} are the inner and outer radii of the cylinder, respectively[32]. Modifications of the original hyper-lens designed to enhance its imaging abilities have been investigated in several studies [64–68]. Some prototypes of these super-lenses have been realized for THz radiation, microwave and acoustic wave, in the visible visible range are exploited to realized a lens able to detect a nanoscale object. The hyper-lens consists of a curved stack of alternating Al_2O_3 and Ag layers that are 35 nm thick. To create a subwavelength object, the word "ON" was inscribed on a 50 nm thick chrome layer deposited on the inner surface of the hyper-lens. The object was illuminated with a laser beam (central wavelength, 365 nm; linewidth, 10 nm). The far-field image was focused onto the image plane by a conventional lens. Using this experimental configuration, a subwavelength resolution of 130 nm was achieved. Recently, an optical hyper-lens formed on a semispherical substrate has been demonstrated [65]. The structure operates at a wavelength of 410 nm, and it permits two 100 nm diameter dots separated by a distance of 100 nm to be resolved. Hyper-lenses are described in more detail in a recent review [69]. Hyperbolic Metamaterials should be use also to enhance the spontaneous emission and the related Purcell Factor [70, 71].

1.3.1 Collimation effect in ϵNear Zero and Pole metamaterials and Lens effect

As evidenced in the previous section, we highlight the possibility to exploit this class of metamaterials for self light collimation and/or canalization through the effective medium. As studied before by using the EMT evaluation and reported in literature, we can explain how an ϵNear Zero (and Pole) metamaterials is able to self-collimate the light through itself [17, 47, 72]. Light propagation inside a HMM can be rigorously described by means of the dyadic Green's function [73]. Such an analysis leads to the conclusion that light emitted in the direction of the extraordinary axis from a localized source placed on the top of a HMM, propagates within the HMM as a so-called resonance cone [74]. Such a concept is expressed where a 50% fill fraction Ag/ITO HMM is excited with a vertically oriented point dipole at 750 nm, falling in the hyperbolic region. The resonance cone is visible as two lobes propagating through the HMM, separated by a semi-angle θ. The propagation in resonance-cones is the spatial counterpart of the hyperbolic dispersion occurring in the iso-frequency contours of the dispersion relation. The aperture θ of the resonance cone can be calculated as follows [75]:

$$|\theta| = \sqrt{-\frac{\varepsilon_{\parallel}}{\varepsilon_{\perp}}} \tag{1.17}$$

If $\tilde{\varepsilon}_{\parallel} \to 0$ or $\tilde{\varepsilon}_{\perp} \to \infty$ or, even better, $\tilde{\varepsilon}_{\parallel} \to \wedge 0 \tilde{\varepsilon}_{\perp} \to \infty$, then $\theta \to 0$ and light is expected to propagate through the HMM as a well confined solitary wave *(soliton)*. Fig. 1.6a shows the value θ as a function of the wavelength, in a 50% fill fraction Ag/ITO HMM. Noticeably, at the ϵNZP wavelength equal to 414 nm, $\theta = 0$. However, a simple ϵNZ condition as in the case in which only $\tilde{\varepsilon}_{\parallel} \to 0$ is not sufficient to reach this extreme collimation effect. Fig. 1.6b shows the norm of the electric field for a 50% fill fraction Ag/ITO HMM. In this case, the electric field coming from a vertically oriented dipole is collimated in a highly confined soliton, whose FWHM *(Full Width at Half Maximum)* is about 50 nm. In Fig. 1.6c, the electric field norm of an $Ag/ITO\ 20/40\ nm$ HMM at the ϵNZ wavelength of 494 nm is presented. Clearly, even though for this latter HMM $\tilde{\varepsilon}_{\parallel} \to 0$, no super-collimation effect is present. Indeed, for an ϵNZP HMM it is always verified that $K_z = 0$. Therefore, light propagating inside the HMM in the ϵNZP regime experiences ideally no phase change and traverses the HMM as its front and back layer are in immediate contact. Obviously, losses present in the metal prevent such ideal condition from occurring and attenuation is present. One way of overcoming this drawback is compensating the losses by employing a suitably dimensioned fluorophore as a dielectric[72]. The super-collimation effect can be investigated by exciting the ϵNZP HMM with strongly localized light sources. Fig. 1.6d shows the confocal analysis of the transmission through a 50% fill fraction HMM made of $Ag/ITO\ 20/20\ nm$ five bilayers. In this experiment, light coming from a pulsed laser was focused on top of the HMM by means of a 100 $\times$ objective (0.75 NA) and collected via a 50 $\times$ objective (0.5 NA). No transmitted beam is detected when analyzing the sample at 530 nm, in the type II region, confirming the highly reflective behavior of

the HMM in this regime. Interestingly, even though it is known that shorter wavelengths are focused in smaller diameters (thus usually allowing higher resolutions), the FWHM of the transmitted beam at 355 nm (type I regime) is much broader than the one measured at 414 nm, being the ϵNZP wavelength for such HMM. This confirms the super-collimation effect occurring at the ϵNZP wavelength[47]. Such an effect is much more pronounced as much the excitation source approaches the periodicity of the HMM, ideally approximating the point dipole. An interesting possibility to approach such an experimental scenario is illuminating the εNZP HMM via Scanning Near field Optical Microscopy (SNOM). Such a technique makes use of nano-metric hollow tips whose hole diameter is in the range of few tenths of nanometers (60 or 90 nm). In order to numerically simulate the typical NSOM excitation by means of a Finite Element Method approach *(COMSOL Multiphysics)*, it is possible to excite the ϵNZP HMM from a nanometric slit placed at the top of the HMM. Fig. 1.6e shows the case of the same HMM as before, illuminated from a 40 nm slit (equal to the thickness of each bilayer that constitutes the HMM) placed on the top of the HMM at 414 nm (ϵNZP wavelength). Clearly, light propagates inside the HMM as a well-confined soliton, with a FWHM comparable to the period of the HMM. Noticeably, as confirmed in the inset of Fig. 1.6e, a propagation length of the super-collimated beam of more than 100 Rayleigh lengths is found. Now we want to introduce as a ϵNZ

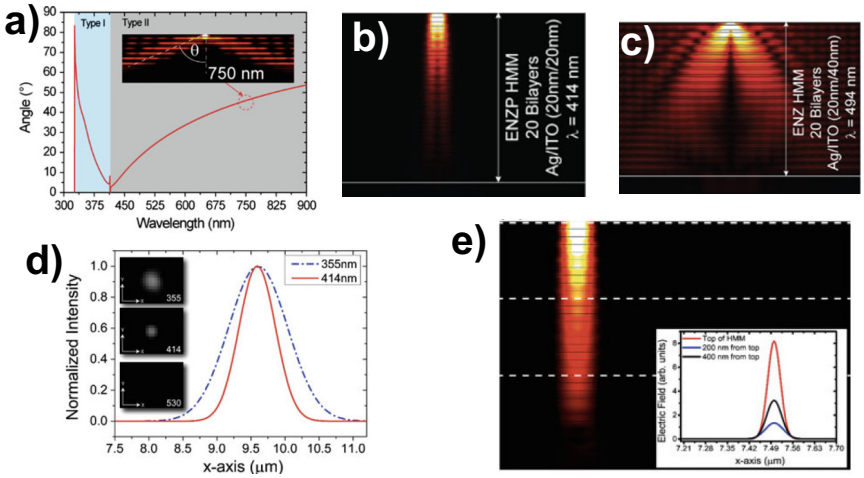

FIGURE 1.6: a) Resonance cone calculation for the considered εNZP HMM. b) Super-collimation at the εNZP wavelength and c) propagation through a simple εNZ HMM d) Confocal analysis of the εNZP HMM. Light impinging on the HMM at the ϵNZP wavelength shows a much smaller FWHM with respect to a shorter wavelength in the type I regime. e) Super-collimation through the HMM of light coming from a 40 nm width excitation slit. Propagation in the HMM lasts for more than 100 Rayleigh lengths. Adapted from Ref. [47]

HMM should be considered a high resolutive lens. The super-collimation effect explained above has the noticeable consequence of allowing extremely high-resolution imaging. In 2003, Ramakrishna et al. described the mechanism lying behind the super-resolution achievable in a similar system [76]. It

is convenient to decompose the electromagnetic radiation scattered or emitted in the x-y plane by a 2D object, into its spatial (k_x and k_y) and polarization (σ) Fourier components:

$$E(x,y,z,t) = \sum_{k_y,k_y,\sigma} E_\sigma(k_x,k_y,k_z)exp[i(k_x x + k_y y + k_z z - \omega t)] \tag{1.18}$$

Since k_x, k_y, and k_z are complex quantities, a further decomposition in real and imaginary components is possible. The real components describe the coarse details of the image. They are associated with propagating waves and constitute the low frequency content of the Fourier expansion. The finest details are, instead, included in the evanescent components, constituting the high-frequency content. The dependence on z of the amplitude of each Fourier component makes the image distorted in the x-y plane while propagating along z. Common dielectric lenses can account only for phase correction in the low-frequency details so that the high-frequency component evanescently decays, letting the nanometric high-frequency details to be lost. In order to deal with the evanescent, high-frequency field component, plasmonic materials are needed. Even a simple single layer of silver can be used to improve the resolution in the near field [77]. However, the single slab plasmonic lens results extremely sensitive to the absorption of the plasmonic layer. On the other hand, light propagating in a multilayered ENZP HMM has the special characteristic of evolving symmetrically in the metallic and dielectric slabs, causing the generation of the super-collimated soliton. Equation (1.5) reveals also that in an ENZP HMM, the component k_z is always equal to zero. Therefore, the phase-front of a wave propagating along the z-direction in such a material experiences no changes. The xy high-frequency nanometric Fourier components of the electric field, scattered or radiated from a 2D object placed at the top of the HMM, propagate as straight solitons within the HMM, appearing unvaried at the exit. The great advantage of this effect is that, in the limit of the near field, the resolution achievable in such a system is no more related to the classic diffraction limit but, rather, is equal to [76],

$$\Delta = 2\pi\varepsilon_2^m(\lambda)d \tag{1.19}$$

being ε_2^m the imaginary dielectric permittivity of the metal and d the thickness of the single slab. As demonstrated from Caligiuri et all[17, 47], it is possible to exploit the ϵNZP HMM as high-resolutive lens, they simulated and experimentally shown how is possible to collect the imaging of three nanometric objects placed on the top of this kind of structures. In particular, a monochromatic plane wave coming from an excitation slit of 500 nm, illuminates three polymeric element (n=1.45) positioned firstly on the top of a simple glass slab and then on the HMM, (the thickness of the glass slab is equal to whole HMM). The three elements are polymeric rectangles (height = 100 nm and width = 40 nm) separated by 40 nm from each other. They conducted the analysis at two different wavelengths, one at 350 nm (type I range) and the second one at 414 nm (super-collimation wavelength). Clearly, in the cases of glass slab as well as in that of the HMM operating as HMM of type one, no super-collimation occurred, and the light was spread. On the contrary,

when the HMM is illuminated at its εNZP wavelength, the super-collimation effect induces all the components of the image, coming from the three objects placed on the top of the HMM, to be perfectly preserved and accessible at the exit layer. It is worth noticing that, at the εNZP wavelength, the radiation propagates within the HMM almost unvaried. In order to experimentally demonstrate the possibility of reaching nanometric resolution with such systems, they proposed an experimental proof-of-concept of a real system. A single ITO/Ag bilayer, with a fill fraction of 50%, was fabricated, in order to collect a high transmissivity. The proposed experiment consists of a 1D grating realized with strips of 250 nm slit-width and periodicity of 500 nm, the grating was used as the structure that they collected at the exit focal plane of the HMM. A confocal analysis has been conducted illuminating at the same wavelengths proposed in the simulations. Noticeably, even though in principle confocal imaging shows higher resolution when conducted with shorter wavelength, they demonstrate that the grating is only visible when the experiment is carried out at the εNZP wavelength (414 nm).

1.4 Conclusion

In summary, this first Chapter covers the role to introduce the main aspects about the wide but extremely interesting word of metamaterials. It will serve us like a handbook to well understand the interesting and intriguing features of these kind of materials. It focuses the reader attention on the main aspects of metamaterials, such as their characteristic iso-frequencies, the effective medium theory and the related way to evaluate it, and last but not the least, the plasmonic dispersion relations that explain the phenomena arisen at each metal/ dielectric interface. I would like to highlight how metamaterials that are a particular class of optical structures human-made, consisting of a periodic arrangement of metallic and dielectric layers, allow breaking the resolution limit imposed by classic optics. In order to exploit these features, HMMs and optical nano-cavities can be designed to manifest the so-called dielectric singularity, ϵNZ(P). Such an extreme propagation regime allows to canalize the light inside the HMM or nano-cavities and reach a resolution limited only by the periodicity of the metamaterial; it is possible to resume it in the following sentence "the smaller the period, the higher the resolution".

Chapter 2

Metamaterials Design and Experimental Characterization

In this second Chapter, the main aspects about the ellipsometric spectroscopy and the main numerical methods used to design, predict and study the optical, photonic or plasmonic behavior of several kinds of metamaterials have been addressed. We begin analyzing the Transfer Matrix Method and its implementation in a versatile Matlab-based tool. Then, a next section will be devoted to explain the implementation of an ellipsometric technique in a Finite Element Method (FEM) thus realizing a simple, yet robust, method able to evaluate and predict, with a high level of accuracy, the optical properties of single and multi-layered nanostructures. The method has been validated by three case studies with increasing numerical complexity: (i) a single thin layer (20 nm) of Ag deposited on a glass substrate; (ii) a metamaterial composed of five bi-layers of Ag/ITO (indium tin oxide), with a thickness of 20 nm each; (iii) two asymmetric nano cavities (substrate/Ag/thick-ITO/Ag/thin-ITO). A thorough study of this latter configuration reveals peculiar metamaterial effects that can widen the actual scenario in nanophotonic applications. Numerical results have been compared with experimental data provided by real ellipsometric measurements performed on the above mentioned ad hoc fabricated nanostructures. The obtained agreement is excellent, suggesting this method as a reliable research tool to design multiband metamaterials able to work in a broad spectral range. Then, numerical and experimental results obtained in plasmonic Metal-Insulator nanocavities are reported. These latter systems are again composed by silver as metal, and two different materials as insulator, namely indium tin oxide (ITO) and zinc oxide (ZnO). The proposed nano-cavities exhibit extraordinary optical effects as extraordinary transmission, zero reflection at resonant wavelengths, and tunable color hue in dependence of the incident/viewing angles for different incident polarizations. These phenomena are related to the formation of surface plasmon polaritons and gap surface plasmons in the nano-cavities whose presence is evidenced by a remarkable sigmoidal behavior of the pseudo dielectric function, with epsilon-near-zero singularities in its real and imaginary parts. This function is directly calculated from the measured ellipsometric parameters Ψ and Δ and allows probing, in a fast and effective way, the existence of plasmonic modes. Moreover, the ellipsometric analysis of these systems also shows, in presence of these singularities, a pronounced dephasing between p- and s- reflected beams that can lead to a

Goos-Hänchen shift effect to be exploited for sensing applications. Thanks to their unusual optical properties, the proposed nano-cavities open a wide scenario of applications in fields like tunable color filters, optics, photonics, physical security and sensing.

2.1 Ellipsometry

In this section the main concept of ellipsometry as a variable angle spectroscopic technique is introduced. This technique allows evaluating the optical characteristics of a physical system composed of a single layer or more complex multi-material system. Before describing principle and functioning of an ellipsometer, it is convenient to shortly introduce the state of the art in literature regarding the importance of this technique. It is remarkable what a detailed insight can be acquired when performing spectroscopic ellipsometry of thin films and bulk materials,[78–80] including monitoring of film growth,[81] surface roughness,[82] detection of micro- and nano-structures on a surface,[83–85] and determination of general optical material characteristics [86–89]. The measured signal is the change in polarization as the incident radiation (in a known polarization state) interacts with the material structure of interest (reflected, absorbed, scattered, or transmitted). The polarization change is quantified by an amplitude ratio, Ψ, and a phase difference, Δ (defined below). Because the signal depends on the thickness as well as the material properties, ellipsometry represents, in principle, a universal tool for contact free determination of thickness and optical constants of films of all kinds [90]. Upon analysing the change of polarization of light, ellipsometry can yield information about layers that are thinner than the wavelength of the probing light itself, even down to a single atomic layer. Ellipsometry can probe the complex refractive index or dielectric function tensor, which gives access to fundamental physical parameters like those listed above. The technique is thus commonly used to characterize film thickness for single layers or complex multilayer stacks ranging from a few angstroms or tenths of a nanometer to several micrometers with excellent accuracy. Typically, ellipsometry is performed only in a reflection setup. The exact nature of the polarization change is determined by the sample properties (thickness, complex refractive index or dielectric function tensor). Although optical techniques are inherently diffraction-limited, ellipsometry exploits phase information (polarization state), and can achieve sub-nanometer resolution. In its simplest form, the technique is applicable to thin films with thickness L less than a nanometer to several micrometers. Most models assume the sample as composed of a small number of discrete, well-defined layers that are optically homogeneous and isotropic. Violation of these assumptions requires more advanced variants of the technique (see below). Methods of immersion or multiangular ellipsometry are applied to find the optical constants of the material with rough sample surface or presence of inhomogeneous media. New methodological approaches allow the use of reflection ellipsometry to measure physical and technical characteristics of gradient elements,

in case the surface layer of the optical detail is not homogeneous [91] Ellipsometry measures the complex reflectance ratio ρ of a system, which may be parametrized by the amplitude component Ψ and the phase difference Δ. The polarization state of the light incident on the sample may be decomposed into an s and a p component (with the s and p components respectively oscillating perpendicular and parallel to the plane of incidence). The amplitudes of s and p components, after reflection and normalized to their initial value, are denoted by r_s and r_p respectively (Fresnel coefficients). The angle of incidence is typically chosen close to the Brewster angle of the sample to ensure the maximum difference in r_p and r_s [92]. The Ψ and Δ parameters, measured from ellipsometry, are defined from the ratio of the amplitude reflection coefficients r_p over r_s for p- and s-polarizations:

$$\rho = \frac{r_p}{r_s} = \tan\Psi \cdot e^{i\Delta} \tag{2.1}$$

Thus, $\tan\Psi$ is the amplitude ratio upon reflection, and Δ is the phase shift (difference). (Note that the right side of the equation is simply another way to represent a complex number.) Since ellipsometry is measuring the ratio (or difference) of two values (rather than their absolute value), it is very robust, accurate, and reproducible. For instance, it is relatively insensitive to scattering and light fluctuations and requires no standard sample or reference beam. Ellipsometry is an indirect method, i.e. in general the measured Ψ and Δ cannot be converted directly into the optical constants of the sample. Normally, a model analysis must be performed, see for example the Forouhi Bloomer model - this is one weakness of ellipsometry. Models can be physically based on energy transitions or simply free parameters used to fit the data. Entire courses are taught in the modeling of the raw data. Direct inversion of Ψ and Δ is only possible in very simple cases of isotropic, homogeneous and infinitely thick films. In all other cases a layer model must be used, which considers the optical constants (refractive index or dielectric function tensor) and thickness parameters of all individual layers of the sample including the correct layer sequence. Using an iterative procedure (least-squares minimization), unknown optical constants and/or thickness parameters are varied. The calculated ellipsometer angle values which match the experimental data best provide the optical constants and thickness parameters of the sample. Ellipsometry has a number of advantages compared to standard reflection intensity measurements:

- Ellipsometry measures at least two parameters at each wavelength of the spectrum. If generalized ellipsometry is applied, up to 16 parameters can be measured for each wavelength.
- Ellipsometry measures an intensity ratio instead of pure intensities. Therefore, ellipsometry is less affected by intensity instabilities of the light source or atmospheric absorption.
- By using polarized light, normal ambient unpolarized stray light does not significantly influence the measurement, no dark box is necessary. No reference measurement is necessary.

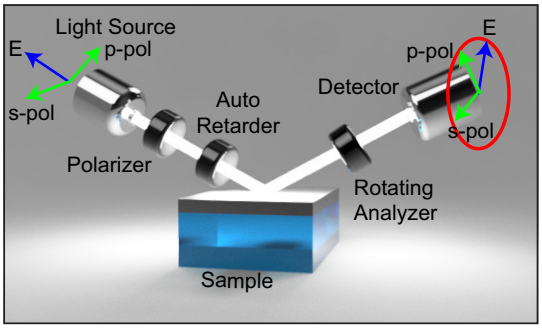

FIGURE 2.1: The sketch shows the real constitutive parts of an ellipsometer and the electromagnetic wave composed from both polarizations. Figure readapted from [93].

- Both real and imaginary part of the dielectric function (or complex refractive index) can be extracted without the necessity to perform a Kramers-Kronig analysis.

Ellipsometry is especially superior to reflectivity measurements when studying anisotropic samples.

2.2 Transfer Matrix Method

The *Transfer Matrix Method*, also indicated as *TMM*, is a numerical method used in optics to analyze the propagation of electromagnetic or waves through a stratified medium [94]. This is for example relevant for the design of anti-reflective coatings and dielectric mirrors. The reflection of light from a single interface between two media is described by the Fresnel coefficient equations:

$$\begin{aligned} t_s &= \frac{2n_1 cos\theta_1}{n_1 cos\theta_1 + n_2 cos\theta_2} \\ r_s &= \frac{n_1 cos\theta_1 - n2_c cos\theta_2}{n_1 cos\theta_1 + n_2 cos\theta_2} \\ t_p &= \frac{2n_1 cos\theta_1}{n_1 cos\theta_2 + n_2 cos\theta_1} \\ r_p &= \frac{n_1 cos\theta_2 - n2_c cos\theta_1}{n_1 cos\theta_2 + n_2 cos\theta_1} \end{aligned} \tag{2.2}$$

However, when multiple interfaces are present, the reflections themselves are also partially transmitted and then partially reflected. Depending on the exact path length, these reflections can interfere destructively or constructively. The overall reflection of a layer structure is the sum of an infinite number of reflections. The TMM is based on the fact that, according to Maxwell's equations, there are simple continuity conditions for the electric field across boundaries from one medium to the next one. If the field is known at the beginning of a layer, the field at the end of the layer can be derived from a

simple matrix operation. A stack of layers can then be represented as a system matrix, which is the product of the individual layer matrices. The final step of the method involves converting the system matrix back into reflection and transmission coefficients. Below is described how the transfer matrix is applied to electromagnetic waves (for example light) of a given frequency propagating through a stack of layers at normal incidence. This method can be generalized to deal with incidence at an angle, absorbing media, and media with magnetic properties. We assume that the stack layers are normal to the z, axis and that the field within one layer can be represented as the superposition of a $left-$ and $right-$traveling wave with wave number k,

$$E(z) = E_r e^{(ikz)} + E_l e^{(-ikz)} \tag{2.3}$$

$$H(z) = \frac{1}{Z_c} E_r e^{(ikz)} - \frac{1}{Z_c} E_l e^{(-ikz)} \tag{2.4}$$

Since there are two equations relating E and H to E_r and E_l, these two representations are equivalent. In the new representation, propagation over a distance L into the positive z, direction is described by the unimodular matrix:

$$\begin{pmatrix} \cos kL & iZ_c \sin kL \\ \frac{i}{Z_c} \sin kL & \cos kL \end{pmatrix} \tag{2.5}$$

and

$$\begin{pmatrix} E(z+L) \\ H(z+L) \end{pmatrix} = M \begin{pmatrix} E(z) \\ H(z) \end{pmatrix} \tag{2.6}$$

Such a matrix can represent propagation through a layer if k is the wave number in the medium and L the thickness of the layer: For a system with N layers, each layer j has a transfer matrix M_j, where j increases towards higher z values. The system transfer matrix is then $M_s = M_N.....M_2 * M_1$ Typically, one would like to know the reflectance and transmittance of the layer structure. If the layer stack starts at $z = 0$, then for negative z, the field is described as $E_L(z) = E_0 e^{ik_L z} + rE_0 e^{-ik_L z}, \qquad z < 0$, where E_0 is the amplitude of the incoming wave, k_L the wave number in the left medium, and r is the amplitude reflectance coefficient of the layer structure. On the other side of the layer structure, the field consists of a right-propagating transmitted field $E_R(z) = tE_0 e^{ik_R z}, \qquad z > L'$, where t is the amplitude transmittance, k_R is the wave number in the rightmost medium, and L is the total thickness. If $H_L = 1/ikZ_c dE_L/dz$ and $H_R = 1/ikZ_c dE_R/dz$, then we can solve

$$\begin{pmatrix} E(z_R) \\ H(z_R) \end{pmatrix} = M \cdot \begin{pmatrix} E(0) \\ H(0) \end{pmatrix} \tag{2.7}$$

in terms of the matrix elements M_{mn} of the system matrix M_s and obtain:

$$t = 2ik_L e^{-ik_R L} \left[\frac{1}{-M_{21} + k_L k_R M_{12} + i(k_R M_{11} + k_L M_{22})} \right] \tag{2.8}$$

and

$$r = \left[\frac{(M_{21} + k_L k_R M_{12}) + i(k_L M_{22} - k_R M_{11})}{(-M_{21} + k_L k_R M_{12}) + i(k_L M_{22} + k_R M_{11})} \right] \tag{2.9}$$

The transmittance and reflectance (i.e., the fractions of the incident intensity $|E_0|^2$ transmitted and reflected by the layer) are often of more practical use and are given by $T = \frac{k_R}{k_L}|t|^2$ and $R = |r|^2$, respectively (at normal incidence).

Coding a TMM in Matlab

The TMM is an outstanding tool for the design of HMM and εNZ(P) metamaterials. In the following, a way is presented to implement this physical method in a numerical code that can be efficiently exploited to design metamaterials. This method also represents a convenient tool in terms of computing resources to investigate in a fast way the optical response of a designed system before its realization. Indeed, by using the commercial software Matlab it is easy to implement a homebuilt code able to work as a TMM and predict the optical behavior of multi-stack metamaterials or more complex systems. The code begins with the input of a series of data like number of layers, incident angle, polarization of the electromagnetic wave (TE or TM) and thickness of each layer. Then, it evaluates the transverse wave vectors, the medium parameters and the system initializes the global scattering matrix. This latter rules on the main reflectance and transmittance parameters represented by $S11$, $S21$, $S12$ and $S22$. The $S11$ parameter quantifies how much of the wave applied to the input Port 1 reflects from the same input Port 1. $S21$ quantifies how much of that same applied wave transmits through the device to the output Port 2. $S12$ quantifies how much of a wave applied to Port 2 will transmit through to Port 1. Finally, $S22$ quantifies how much of the second applied wave reflects from Port 2. After that, a loop cycle starts and for each layer (the iteration i) the parameters mentioned above, including the scattering matrix are evaluated. Then again, each scattering matrix contribute is updated to a global one and when the number of layer is exhausted the loop cycle is completed. Finally the results obtained by the global scattering matrix is connected with the two layer that represents the external layer (i.e. air and the substrate), the source and it's polarization is calculated and it leads to evaluate the transmitted and reflected fields by the Fresnel coefficient within the transmittance and the reflectance. A block diagram of the TMM Matlab-code functioning is reported in the Appendix B.

2.3 Numerical ellipsometer by using COMSOL Multiphysics

A Finite Element Method (FEM) analysis gives the possibility to solve, starting from the partial differential equations (PDEs) governing the given system, various physical conditions. For example, it is possible to simulate problems of elasticity and applied strains, thermal heating and thermal transport,

fluid mechanics and chemical transport and, last but not least, problems related to the electromagnetic wave propagation and light-matter interactions [95–97]. During my Ph.D course, my attention was devoted to develop systems able to predict several physical behaviors in an all-in-one simulation. COMSOL Multiphysics represents a valid software tool to support this approach to scientific research. Before introducing how this tool is used in specific cases, it is convenient to start explaining how it works in the ellipsometric case[93]. Indeed, the proposed numerical ellipsometric analysis has been performed by using the COMSOL Multiphysics platform, that gives the possibility to use a 2D or 3D environment. The 3D geometry built in COMSOL is composed by a parallelepiped with a height of $3 \cdot d$, where d is the edge length which is typically comparable with the minimum wavelength value, in our case this is set to $\lambda = 400\,nm$. The choice of d is fundamental for the optimal propagation of the lightwave inside the system preventing any diffraction or boundary problems. The numerical setup of the NEA model is sketched in Fig. 2.2a, with the three blocks representing the superstrate (air), the substrate (glass) and the multi-layer system well in evidence. In COMSOL, sources or detectors of electromagnetic radiation are created by using ports by which the radiation enters or exits the simulated system. In our case, there is a port (Port_{in}) on the top from where the radiation is emitted and a port on the bottom (Port_{out}) that behaves as a detector. There are several kinds of ports: user defined, periodic, rectangular, circular, depending on the particular requirement of the physical problem. In order to model our system in the correct way, the xy plane is considered infinite. This choice can be reproduced in COMSOL by using periodic ports. In our model, a periodic port (representing the source) is placed on the top of the parallelepiped and it is configured as "active port". A second port is placed on the bottom of our geometry, representing the detector, and it is configured as "active-off port". Then, periodic boundary conditions (PBCs) are applied to the four faces of the geometry, along x and y directions (Fig. 2.2b) paired two-by-two. The PBCs ensure the above mentioned infinite conditions. An important role in the numerical system is carried out by the mesh that discretizes the problem. COMSOL Multiphysics gives the opportunity to set it as controlled by the physics, by selecting the option "physics-controlled the mesh" present in "physics study". A "normal mesh" is automatically generated by the software, depending on the minimal size present in the system, compared with the incident wavelength (Fig. 2.2c). To analyze simultaneously TE and TM polarized waves, the user has to add two "physics", belonging to the "Electromagnetic Waves, Frequency Domain" module (identified in the software as "emw"). The two distinct "physics" are used to evaluate the two reflectances R_p and R_s simultaneously, necessary to calculate the ellipsometric angles Ψ and Δ. We recall that ρ is defined as $\rho = \tilde{r}_p/\tilde{r}_s$; $\tilde{r}_p$ and $\tilde{r}_s$ are the complex Fresnel coefficients. Then, being $\rho = \tan(\Psi)e^{i\Delta}$, $\Psi = (arctan(r_p/r_s))$, where $r_{p,s}$ represent the real parts of the Fresnel coefficients ($r_{p,s} = \sqrt{R_{p,s}}$), while Δ is related to the imaginary part of ρ, $\Delta = [\Im(\ln r_p/r_s) + \pi]$. To obtain quantities comparable to the experimental curves, the variables have to be multiplied by $180/\pi$ to convert them from radians to degrees. During my Ph.D path, I also used this FEM software to solve problems that involved

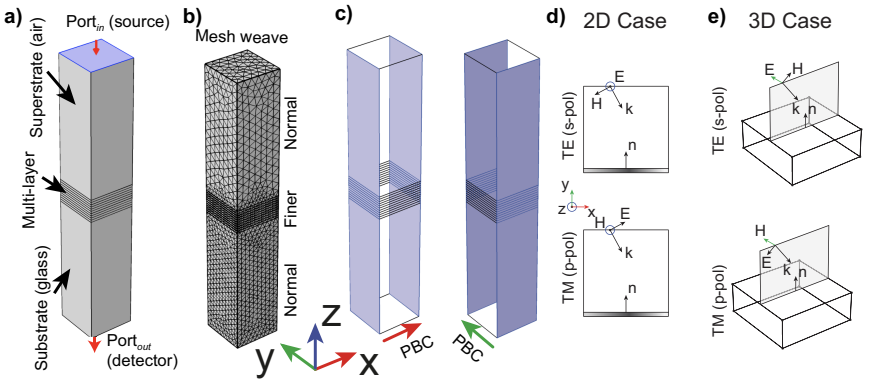

FIGURE 2.2: a) The main structure of the NEA model, it is realized from a parallelepiped divided in layers that constitute the superstrate, the layer of materials and the substrate. b) A sketch of the mesh directly controlled from the physics, the larger part are meshed with a normal weave while for the small parts has been used a fine mesh weave. c)Here it is shown the application direction of the periodic boundary condition from periodic port. d, e) report the 2D and 3D electric and magnetic field vectors drawing respectively. Figure readapted from the main paper and the supplementary electronic information [93].

physical aspects as : plasmonics, thermo-plasmonics and active-plasmonics (e.g. mechanical strain). In fact, it is possible to model a system where an electromagnetic wave impinges on a sample that was stretched by applying an external macro-stimulus (for example along the normal strain direction N). Then, we can collect the extinction cross section (σ_{ext}) as a function of the applied stretching and finally, by using the same wavelength that reaches the σ_{ext} maximum, to study the thermal effects on a single nanoparticle, or ordered array, or specific distributions of metallic nanoparticles [98–100]

2.4 Numerical and experimental examples of spectroscopic ellipsometry

In order to validate the effectiveness of the NEA modeling, in this section numerical predictions have been compared with both curves obtained by using the Matlab TMM code and results of measurements performed on the corresponding real samples. Several multi-layer systems have been designed, fabricated and characterized by an experimental ellipsometric analysis. The first and simplest system is a single Ag layer deposited on a glass substrate (20 nm thickness). The following system is a hyperbolic metamaterial [101] made of a stack of five alternated Ag/ITO bi-layers (ITO stands for Indium Tin Oxide) with the single bilayer having a thickness of 40 nm (20/20). The third system is characterized by a three-materials unit cell repeated three times. The unit cell is made of Al_2O_3 doped Zinc Oxide (AZO), ITO and Ag. The numerical task is particularly difficult because each of the three cells constituting the system has different thickness for each layer. The last and most complex system comprises an asymmetric optical cavity, with nanoscale features, also known as metal-insulator-metal (MIM).[102, 103] Starting from the glass substrate, this is composed of an Ag layer covered by a thick ITO slab, representing the dielectric cavity, and an Ag/thin-ITO bilayer on top. All samples have been experimentally fabricated by exploiting a DC sputtering technique. Then, for all cases the experimental reflectance, transmittance and ellipsometric angles Ψ and Δ have been measured by means of a M-2000 ellipsometer (J.A. Woollam). Figures 2.3a and 2.3b respectively show the numerical calculated and the directly measured reflectance and transmittance, as well as the corresponding numerical curves provided by the NEA and TMM simulations for the first case study. The reflectances, R_p and R_s curves, are measured and calculated by considering an incident angle $\theta_i = 50^\circ$, while the transmittance was measured and simulated at normal incidence. The minimum value at about $\lambda = 350\,nm$ in the reflectance curves (and the related maximum in the transmittance ones) is referred to the Ferrel-Berreman mode for a silver nanometric layer.[104] The difference of about 20% between the amplitude of experimental and simulated curves is due to the presence of the glass substrate in the real sample, partially considered in the simulated case. Indeed, in order to optimize the computational time, the size of the glass in the simulation was decreased to 1200 nm instead of the real 1.1 mm. The result is different only in absolute values but not in the general trend of the curves. Apart from that, the agreement between measurements and simulations is satisfactory. Figure 2.3c show the Ψ and Δ behavior, respectively. The second test of our NEA model has been conducted on a hyperbolic metamaterial (HMM) that, by alternating lossy metal layers to dielectric ones, acquires particular optical features. Thickness and composition of the nanolayers can be opportunely designed in order to exploit unusual optical properties in a desired spectral range. In fact, the particular design and choice of sizes and constitutive materials leads to the *epsilon-near-zero-and-pole* (ε_{NZP}) HMM [75, 105, 106], allowing extraordinary light confinement properties. The proposed HMM system is sketched in the inset of Figure

2.3d and is composed of five Ag/ITO bilayers $t = 20\,nm$ each one, characterized by a fill fraction of 50%. Figures 2.3d and 2.3e show, respectively, the numerical and experimental reflectances (R_p, R_s) and transmittance (T) calculated by the NEA and TMM model together with the comparison between experimental and numerical Ψ and Δ for the same sample (Figures 2.3f. Also in this case, all measured quantities find an impressive agreement with the numerical counterpart. Figures 2.3d-e report reflectance for both polarization s-pol and a p-pol wave, at $\lambda = 390\,nm$ is well evident how the p-pol wave is able to penetrate more efficiently through the HMM structure than in the s-pol case, being transmitted by the medium in accordance with the metamaterial prediction.[107–110] In the last considered case, we have simu-

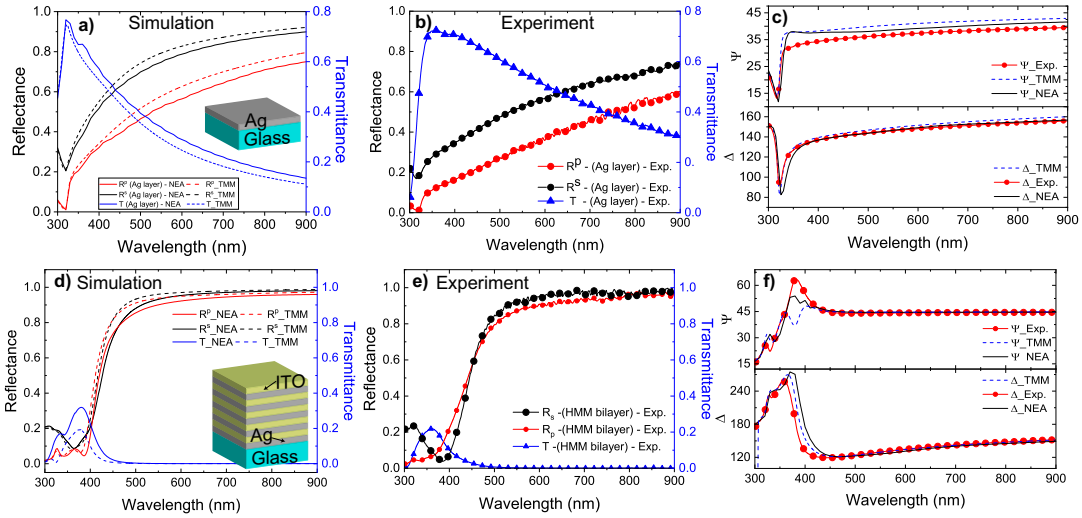

FIGURE 2.3: a-b) R_p reflectances at different angles of the incident light and T transmittances at the normal incidence, calculated by the NEA and TMM models and measured by ellipsometer for the single Ag layer. The inset of a) shows the analyzed structure constituted by a single metal layer. c) The experimental and numerical ellipsometer parameters Ψ and Δ for that system. d-e) R_p reflectances at different angles of the incident light and T transmittances at the normal incidence, calculated by the NEA and TMM models and measured by ellipsometer for the HMM. The inset of d) shows the analyzed structure constituted by five bilayers of Ag/ITO $20/20\,nm$. f) The experimental and numerical ellipsometer parameters Ψ and Δ for the HMM.

lated the optical behavior of an asymmetric multi-layer that does not respect the typical metamaterial fill fraction condition. In fact, when one of the layers is much thicker than the other ones, a nanometric cavity behavior comes in enabling confinement and re-direction of light. This kind of metamaterial opens a new challenge in obtaining nanometric devices with particular optical features suitable for applications. In our case, two different systems have been realized, able to work at one, two, three or more different wavelengths, depending on the thickness of the thick-dielectric layer, in this case ITO. The first nanocavity ($t_1 = 230\,nm$) is able to confine two different working wavelengths, $\lambda = 390\,nm$ and $550\,nm$, while the second one ($t_2 = 350\,nm$)

shows a three wavelengths confinement ($\lambda = 410\,nm$, $520\,nm$ and $750\,nm$). We indicated these systems as two- and three-bands metamaterials (2BMM and 3BMM, respectively) [93]. The two samples were fabricated by starting with a 20nm Ag layer deposited on the glass substrate. Then, different thick-ITO slabs (t_1 and t_2) were deposited. The light confinement is achieved by putting on top of the thick-ITO slabs a final Ag/thin-ITO (20/20) bilayer of 40nm total thickness, obtaining the final 2BMM and 3BMM systems, respectively. The two configurations present unique optical behaviors also verified by the numerical model. The experimental analysis has been carried out as a function of the incident angle (50°, 60° and 70°), under which the p-pol reflectances have been measured (Figures 2.4c and 2.4d refer to the 2BMM and the 3BMM, respectively). As the incident angle increases, a blue shift of the reflectance dips is observed, due to the surface gap plasmons (gsp) able to establish guiding modes in the ITO thick slabs with t_1 (2BMM) and t_2 (3BMM) thicknesses. In presence of an optical cavity, confined modes satisfy the general Fabry-Pérot (FP) condition $\beta t_{cav} = m\pi - \phi$, where β is the complex wave-vector of the lightwave propagating within the cavity, m identifies the given mode generated inside the cavity, ϕ is the reflection dephase angle and t_{cav} is the cavity thickness. In this case, the FP relation, applied to a nano-cavitiy confined by metal layers,[62] is modified as in the following $\beta_{gsp} t_{cav} = m\pi - \phi$, where β_{gsp} is the dispersion relation that we had treated in Chapter 1 section 1.3.1. The obtained modes confirm the results shown in Figure 2.4a: for $m \sim 3$, $\lambda = 390$nm, while $\lambda = 550$nm corresponds to the mode $m \sim 2$. For the 3BMM ($t_{cav} = 350$nm), the results derived from Figure S2d are in agreement with those shown in the electric field maps of Figure 2.4b: $m \sim 4$ is related to $\lambda = 410$nm, $m \sim 3$ to $\lambda = 520$nm and $m \sim 2$ to $\lambda = 750\,nm$. These confined modes are depicted as black curves on the electric field distribution maps reported in Figures 2.4a-b. A qualitative confirmation of this fact is given by the spectral position of the dips present in the reflectance curves (Figures 2.4c-d) that correspond to the working wavelengths mentioned above, for the 2BMM and the 3BMM, respectively. The curves reported in Figures 2.4e-2.4f highlight a value of transmitted light overcoming, for the first system, 60% at $\lambda = 550\,nm$ in case of both experiment and simulation. The second cavity presents instead a larger difference at $\lambda = 520\,nm$ between experiment and simulation, even if the transmitted signal still reaches a noticeable 50% value in the real case. We underline that, in specific spectral windows, the presented systems show transmittance values proportionally much higher than in a single Ag layer (20nm). However, it should be noted that, passing through a nano-cavity, light runs into two metal layers (20nm each) and two (thick and thin) ITO slabs, corresponding to hundreds of nanometers (Fig. 2.4a, blue squares). The surprisingly high signal transmitted by these asymmetric nano-cavities thus evidences their optical behavior as originating from an unusual effective medium. The slight amplitude mismatch between experimental and numerical reflectance dips and transmittance peaks observed in Figures 2.4d and 2.4f (3BMM) is probably due to a collapse of the ITO slab in the Ag layer, causing an overall

reduction of their effective thickness. The field maps and reflectance for s-pol, as well as the comparison of Ψ and Δ between experiments and numerical simulations, are reported in the ESI (Figure S3); the reflectance curves are characterized by the same number of dips also for this "out-of-plane" polarization. The trend of Ψ presents two or three sigmoidal features corresponding to the number and position of dips in reflectance for both polarizations (R_p and R_s). Same behavior is present in the phase-shift reported in the Δ curves (Figures S3e and S3f). It is worth noting that the interesting

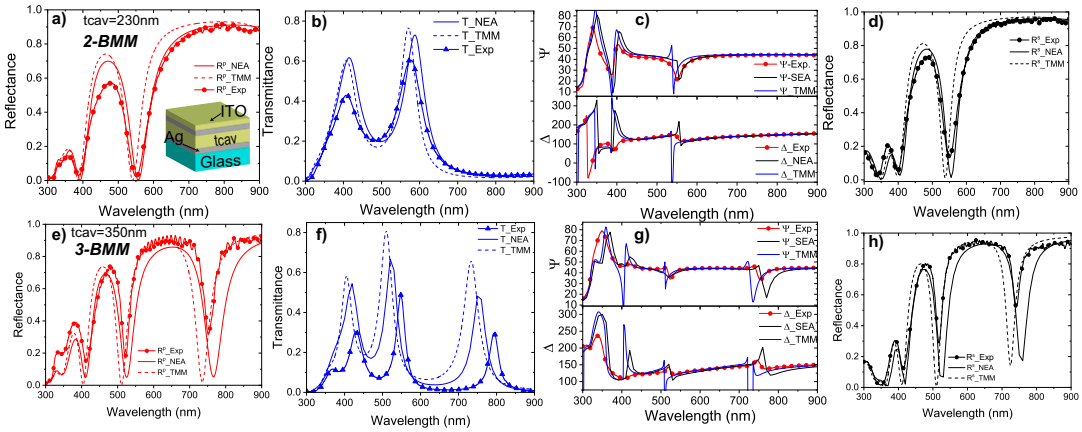

FIGURE 2.4: a-b) R_p reflectances at different angles of the incident light and T transmittances at the normal incidence, measured and calculated by the NEA and TMM models for the 2BMM. The inset of a) shows the analyzed structure where the thickness of the dielectric layer placed between the two metal varying its thickness. c) The experimental and numerical calculated ellipsometer parameters Ψ and Δ for the 2BMM and d) the R_s measured and numerically calculated. e-f) R_p reflectances at different angles of the incident light and T transmittances at the normal incidence, measured and calculated by the NEA and TMM models for the 3BMM. g) The experimental and numerical calculated ellipsometer parameters Ψ and Δ for the 3BMM and h) the R_s measured and numerically calculated.

simultaneous presence of dips in the p- and s-pol reflectance curves shown by this MIM structure is independent from the impinging light polarization direction. As such, these results can be exploited to realize sensors or photovoltaic cells able to work in a wide UV-VIS-NIR range.[111–117] On this way, the 2BMM and 3BMM have been analyzed according with the relation dispersions, already presented in the Chapter 1 section 1.3. In Figures 2.5a and 2.5c the dispersion relations of the 2BMM and the 3BMM are reported, respectively. By considering a general *Fabry-Pérot condition*, the modes allowed by each cavity are evaluated and shown in Fig. 2.5b (2BMM) and 2.5d (3BMM), showing also the permitted regions due to the dielectric light line ($k_0 n_d$, blue lines). In order to complete the numerical analysis of the 3BMM structure, we performed a parametric study of reflectance and transmittance of the system as a function of wavelength (λ_i) and incidence angle (θ_i) of the incoming EM wave in the visible range. The resulting reflectance map, shown in Figure 2.6a, reveals the coupling between the impinging light and the 3BMM, evidenced by the three permitted wavelength bands for incident angles ranging between 0° and 85°. Position and number of these bands,

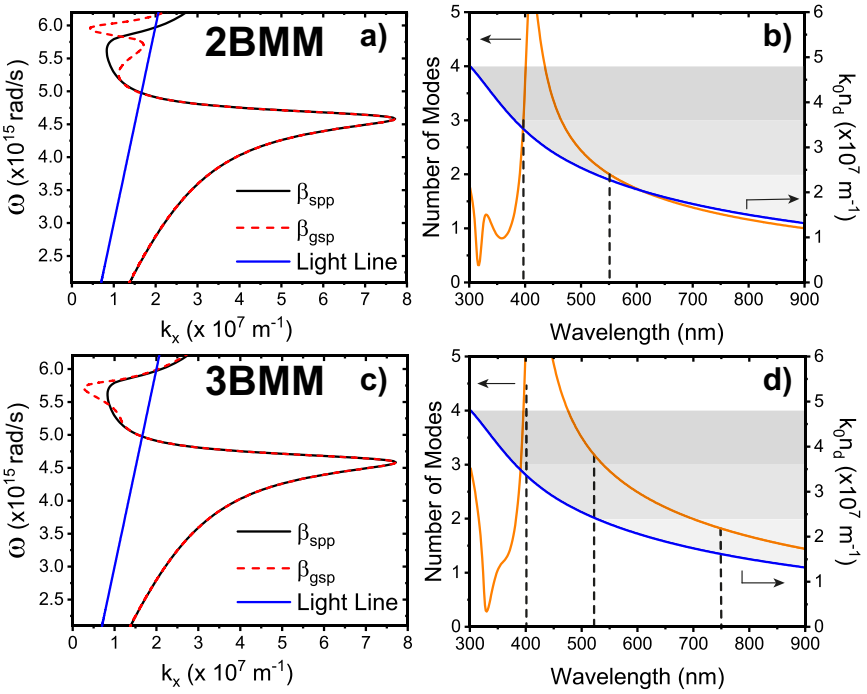

FIGURE 2.5: Plots of the dispersion relations of the a) 2BMM and c) the 3BMM. b-d) Modal analysis for the two systems (orange curves), with the permitted region delimited by the dielectric light line (blue curve). Figure readapted from reference [93]

as already explained, are strongly related to the thickness of the cavity. For instance, if the thickness is reduced to about $200 - 300\,nm$, the dip located around $\lambda = 750\,nm$ disappears, as shown by the 2BMM (Figure 2.4a); for a thickness of about 400nm the wavelength of the same dip is instead shifted around $\lambda = 800\,nm$. By keeping fixed the cavity thickness, the spectral position of the reflectance dips can also be influenced by the presence of a material on top of the 3BMM surface. This suggests the utilization of this system as a sensor for refractive index variations. In order to verify this possibility and carry out a further performance check of the developed tool, we numerically designed another 3BMM structure with $10\,nm$ of AZO placed on its top surface. For the test, the more sensitive confined mode ($m \sim 2$ at $\lambda = 750\,nm$) has been selected. The Brewster angle is calculated by the NEA model as reported in Figure 2.6b for both polarizations. By impinging at the Brewster angle (60°, white dashed line in Figure 2.6a) and p-polarized light on the structure, the reflectance curve obtained in presence of the AZO coating (dashed-dot red line in Figure 2.6c) shows a well evident redshift of about 10nm with respect to the curve without coating (black solid line in Figure 2.6c). As a final remark, the exploitation of a generic N-BMM structure for applications presents many benefits: i) position and amplitude (depth) of the transmittance (reflectance) are directly correlated to the thickness of the ITO slab; ii) these transmittance peaks (reflectance dips) have been obtained without the presence of 3D structures on the material surface to couple the impinging light in; iii) the system is independent from the impinging light

polarization; iv) the fast and cost-effective fabrication process used to realize the structures.

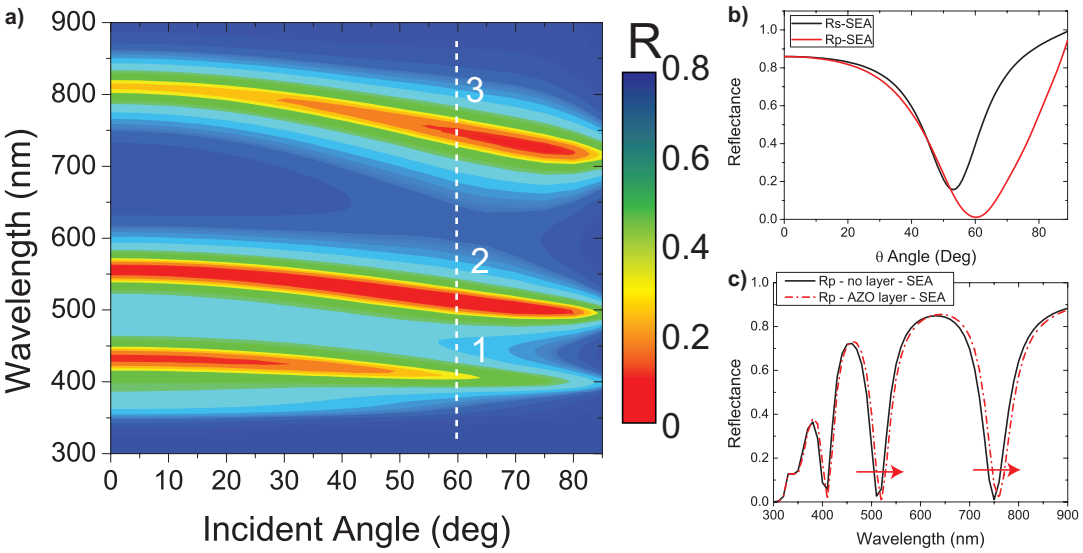

FIGURE 2.6: a)Reflectance map calculated by varying the incident wavelength λ_i and angle θ_i. The dashed white line drawn on the field map indicates the position of the Brewster angle for this structure that has been used as the incident angle in the numerical simulations whose results are reported in the graph. b) The evaluation of the Brewster angle for p- and s-polarization at $\lambda = 750\,nm$. c) R_p reflectances calculated for the sensor realized by using the 3BMM with and without an AZO coating layer of $10\,nm$ on its top surface (solid black and dashed-dot red lines, respectively).

2.5 Color gamut a macroscopic effects of plasmonic modes inside optical nano-cavities

After this introduction and demonstration about the numerical models used to predict metamaterials behavior, it is easy to comprehend how the NEA tool is precise and useful to numerically predict the behavior of whatever designed structure. Before explaining the roadmap that guides to the macroscopic effect arising from nano-cavity metamaterials, we briefly introduce the actual state of the art about these systems summarizing what has already been explained for multi-layered metamaterial behaviors. This is needed in order to understand what happens in these peculiar and interesting systems. As mentioned above, a great deal of scientific interest is aimed to systems as MIM, MIMI due to the anisotropic permittivity that classifies these metamaterials as ε_{NZ} [47, 101, 118]. As described in the previous section, when the inner dielectric layer is thicker (hundreds of nanometers) than the metal ones (tens of nanometers), the system behaves as an optical nano-cavity. Such systems allow efficient concentration and confinement of electromagnetic energy, making them suitable for numerous implementations in light emission

and detection [119], photovoltaics [120–122], Bragg reflection [123, 124], plasmonic devices [103, 125], for optics and related applications [124, 126, 127], telecommunications [125, 128], and many others [102, 129, 130]. Under a physical point of view, when metal/ insulator and insulator/ metal interfaces are close to each other, the dispersion curve of the single interface splits into high and low energy modes [131]. This gives the possibility to excite surface plasmons by a free space wave without requirement of momentum matching, but simply by perpendicularly impinging to the bare metallic endface of the MIM [132]. At the interfaces of the MIM, spontaneous surface plasmon polaritons (SPPs) arise, whose electric field overlaps within the insulator layer. However, due to the matching of the field symmetry, only the low energy mode is excited in the MIM system (using a p-polarized electromagnetic wave). In case of a MIMI system, it is instead possible to excite both low and high (guided) energy modes, respectively with p- and s-polarized light. [133–135]. In presence of the hybridization of the SPPs, excited at the two metal interfaces and decayed in the thick dielectric layer, it has been numerically and experimentally demonstrated the formation of gap surface plasmons (GSPs) related to high energy modes[58, 131, 136–138]. Although several studies of GSPs are reported in literature, the fabrication of nanometric gaps with high reproducibility is still not trivial. Here we show how the spontaneous propagation of Gap Surface Plasmons (GSPs) and Surface Plasmon Polaritons (SPPs) in metal/ insulator/metal/insulator system lead to the variation of reflected and transmitted colors [139]. These studies start considering all aspects involved in these optical nano-cavities, firstly we have to investigate the main theoretical aspect related to the systems and then the experimental ellipsometry that lead to a new fast and effective way to determine if the structures are able to generate GSP and SPP. According with our recent studies and the numerical tools presented above we studied the modes inside the system when the metal layer is fixed and the dielectric layer changes its thickness. This study produces a map where the dielectric thickness versus the wavelength shows maximum and minimum in reflectance or transmittance for a fixed angle. Once, the map is collected we can proceed to study the modal analysis as presented in the Chapter 1 section 1.3.1, this analysis leads us to be sure that the mode inside the cavity is just the first the 0^{th} order. In order to investigate the single mode propagation, we evaluate using the NEA tool a reflectance (or transmittance) map for an incident angle of 50°. The maps reported in the figure below show for a small dielectric thickness a single mode confined between the two metal walls, then when it increases the modes m confined inside the nano-cavity due to the Fabry-Pérot behavior pass from $m = 1$ to $m = 4$ in the visible spectrum. Figure 2.7a shows the modes for a MIMI composed as Ag/ITO/Ag/ITO and we studied the coloring effects for two different thickness of the dielectric gap. The first one is studied to have a reflectance dip in the blu and the second in the green, this consideration lead us to choose the dielectric gap thickness of 65 nm and 85 nm respectively. The other considered case is a MIMI composed by Ag/ZnO/Ag/ZnO due to the relevant use of this dielectric in the nano-science. ZnO is largely used in nano-science thanks to its excellent features

in photovoltaics [140, 141], extreme non linearity applications as second harmonic generation [142, 143] and photocatalysis [144, 145] just to name a few. Figure 2.7b shows the reflectance map for a single mode in a cavity made by ZnO at a resonant wavelength of $\lambda = 532\,nm$. In order to establish which kind of metamaterials has been realized, an EMT analysis for a cavity system shows that these systems are εNZ metamaterials across the wavelength of the single mode showing also two spectral region where the cavity presents a type I hyperbolic behavior before the cross point and a type II after that. For the three considered cavities the EMT analysis is reported in Figure 2.7d-f. In

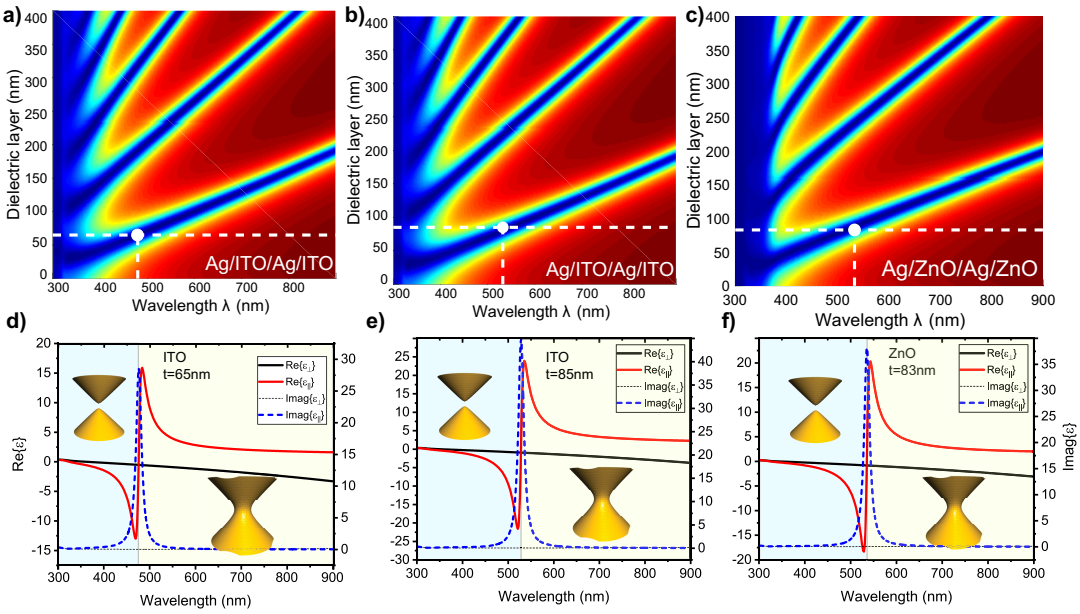

FIGURE 2.7: Calculated reflectance, using NEA analysis, at incident angle of 50° varying the dielectric layer between the metals ones. The vertical dashed lines indicate the resonant wavelengths. a) For the MIMI made by ITO it has been evaluated the case with a thickness of $t = 65\,nm$ and b)for ITO $t = 85\,nm$, c) for ZnO $t = 83\,nm$. The dashed white lines represent for each case the desired single mode at one specific wavelength. d-f) The EMT analysis for the three cavities made by ITO and ZnO respectively have been reported.

order to confirm the plasmonic behavior of these cavities and the presence of a plasmonic mode at the selected wavelength for each cases the dispersion relation have been calculated and displayed in In Figure 2.8 a-b for the ITO cavity $t = 65\,nm$ and $t = 85\,nm$ respectively, and c) for the ZnO one $t = 83\,nm$. As a confirmation of that we evaluated the modal analysis using the already calculated dispersion relation and this study displays a perfect match between the integer mode $m = 1$ at the resonant wavelength. In Figure 2.8d-f are reported the evaluated modal analysis for the three considered cases.

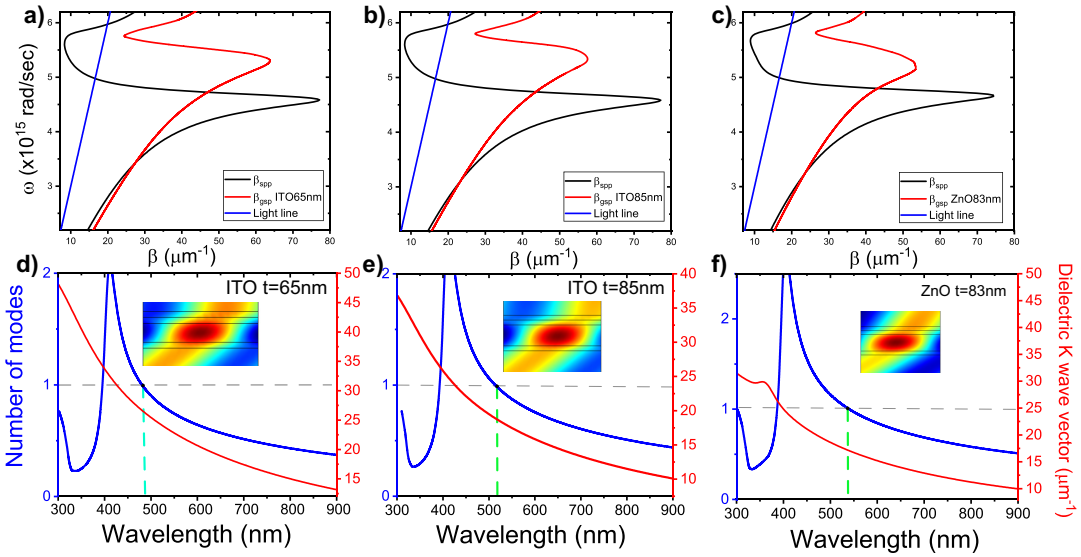

FIGURE 2.8: Calculated dispersion relation according with the Fabry-Pérot condition for a MIMI cavity composed by a) ITO $t = 65\,nm$, b) ITO $t = 85\,nm$ and c) ZnO $t = 83\,nm$. The related mode analysis (d-f) for the three considered MIMI cavities. The vertical dashed lines indicate the resonant wavelengths. The insets show the related mode profile evaluated for each structure by using COMSOL Multiphisycs.

2.6 Pseudo dielectric function $< \tilde{\varepsilon} >$ in MIMI cavity: an effective way to recognize the plasmonic resonances

The ellipsometric characterization of the proposed systems reveals very interesting optical features such as extraordinary transmittance ($T_{p(s)}$)[146] and 0% reflectance ($R_{p(s)}$) for both exciting polarizations (p and s). As demonstrated in the following, these phenomena are related to the formation of SPPs and GSPs whose presence is evidenced by a remarkable sigmoidal behavior of the pseudo dielectric function, with singularities in its real and imaginary parts. The pseudo dielectric function is calculated as $< \tilde{\varepsilon} >=< \varepsilon_1 > -i < \varepsilon_2 >= sin^2\theta_{inc}[1 - tan^2\theta_{inc}((1-\rho)/(1+\rho))^2]$[88, 147, 148], where θ_{inc} is the incident angle of the probe light whereas $\rho = tan(\Psi)e^{-i\Delta}$. Due to the presence of ρ in the expression of $< \tilde{\varepsilon} >$, this is directly related to the measured Ψ and Δ, and so to the R and T by the Fresnel coefficients. The self-momentum matching propagation of plasmonic modes in the fabricated nano-cavities is observed at naked eye through the appearance of bright colors whose hue varies by changing incident light and viewing angles[149–152]. As demonstrated in recent studies, this color hue variation is mainly due to the modes stored inside the cavity [153], or to the presence of metagratings inside the dielectric layer [154], while the absorption at one specific wavelength arises from the specific resonant mode [155]. Although several studies of GSPs are reported in literature, the fabrication of nanometric gaps

with high reproducibility is still not trivial. Finally, the ellispometric analisys of these systems also shows a pronounced de-phasing between p- and s- reflected beams that can lead to a Goos-Hänchen shift effect[156–158]. Indeed, this phase shift results in a lateral spatial shift between the two reflected beams with perpendicular polarizations. The counterpart of this effect for circular and elliptical polarization is the Imbert-Fedorov effect[159]. As demonstrated in previous works[160, 161], the phase shift appears when resonant modes are induced within an optical dielectric cavity, as in the proposed systems. Thanks to these effects, the proposed systems can be involved in a wide scenario of research topics such as nano-photonics applications[157], sensitive detection of biological molecules [162–164], or for the phenomenological study of the lateral reflection for both polarizations[165]. The numerical design and the experimental investigation evidenced a substantial difference between a classical MIM and a MIMI systems configuration. The latter, in fact, presents a pronounced sigmoidal shape in Ψ and Δ behavior, enabling the study of the plasmonic excitation effects and the dephasing that can induce the Goos-Hänchen shift. The comparison between numerical reflectances of both polarizations, Ψ and Δ, for a MIM and MIMI systems is shown in Figure S3. The first one is made by 20 nm of silver, 65 nm of ITO between the two metals while for the MIMI another ITO layer of 20 nm is deposited on the last one of silver. The first realized MIMI (A) (made by Ag/ITO/Ag/ITO layers) is composed of ITO layers of thickness $t_1 = 65\,nm$ and $t_2 = 20\,nm$, respectively (see inset of Figure 2.9a). The experimental measurements show transmittance values around 50% for normal incidence close to the resonance wavelength of $\lambda = 500\,nm$ (dark blue line with symbols), see Figure 2.9a. On the other hand, the reflectance (p-polarization) at 50°, 60° and 70° is almost zero around the resonance wavelength. This leads to the particular feature observed for the Ψ and Δ parameters (Figure 2.9b-c). In fact, Ψ and Δ present a drastic jump with a significant sigmoidal shape centered at $\lambda = 480\,nm$, enhanced for this particular MIMI at 70° (see Figure 2.9b-c, blue curves). The Ψ and Δ parameters highlight the presence of a plasmonic excitation for high and low energy modes at the resonant wavelength, especially when the system is excited with an incident angle of 70°. In the second MIMI (B) system, the first ITO layer is increased to $t_1 = 85\,nm$ (see inset of Figure 2.9d) while the thickness of the other layer remains unchanged. The increase of the first ITO layer of only 20 nm leads to the shift in the resonant wavelengths of 50 nm, where the main transmitted peak is now at $\lambda = 550\,nm$, with a value of almost 50%. The reflectance dips (p-polarization) at 50°, 60° and 70° are almost zero around the resonance wavelength ($\lambda = 532\,nm$, see Figure 2.9d). The parameters Ψ and Δ for this system presenting a thicker ITO layer exhibit the same behaviors of the previous case (see Figs. 2.9e-f), but less pronounced. This feature can be exploited in future applications related, for example, to the Goos-Hänchen shift [163, 164]. This comparison highlights the possibility to easily modify the resonant wavelengths without affecting the performance of the system. In order to identify in a quantitative way the colors related to the experimental curves, a in-house developed Matlab script has been written to calculate and plot the colors related to the

experimental curves on a CIE chromaticity xy-coordinates map [166]. The reflectance curves collected at different angles ($50° - 70°$) are directly identified by some hues of violet (the white dot close to R_{50}-R_{60}-R_{70}) and the transmittance at 0 angle of incidence gives a blur white indicated on the map with T_0. For a complete understanding of the color variation as a function of the resonant wavelengths, numerical transmittance and reflectance values have also been calculated for various incident angles and evidenced by squares on the Gamut plot as shown in Figures 2.9g-h. In case of numerical transmittances, the incidence angles vary from 0° to 80° and are indicated by red squares labelled as T_0 to T_{80}. The CIE chromaticity xy-coordinate maps have been evaluated for both ITO-based MIMI starting from the experimental curves. In Figure 2.9g it is evidenced, for the MIMI (A), that transmitted (T_0) light is a kind of blue while the reflected colors appear quite yellow at different angle from 50° to 70° (R_{50}-R_{60}-R_{70}). For the MIMI (B), see Figure 2.9h, the light that passes through is green (T_0) while the reflections are purple (R_{50}-R_{60}-R_{70}). A further confirmation about the behavior of these two systems

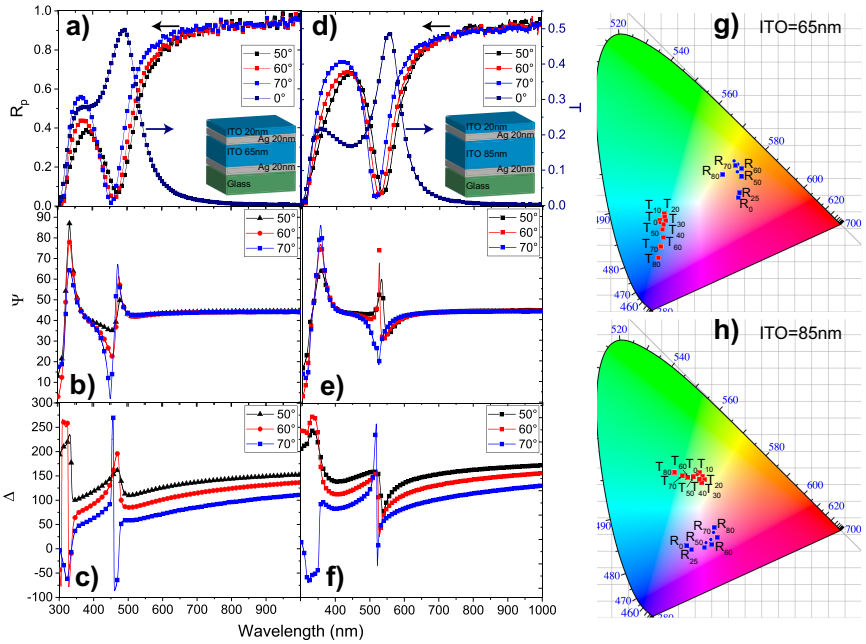

FIGURE 2.9: a) Reflectances (p-pol) and transmittance at different incident angles for the MIMI (A) (Ag/ITO/Ag/ITO)composed of ITO layer $t_1 = 65\,nm$, the inset reports a schematic view of the whole fabricated system with the related thickness of each layer. b,c) Ψ and Δ for MIMI (A) with ITO layer $t_1 = 65\,nm$. d) Reflectances (p-pol), and transmittance at different incident angles for the MIMI (B) composed of the ITO layer with $t_1 = 85\,nm$, the inset shows the whole fabricated system with the new layers thickness. d,e) Ψ and Δ for the MIMI (B) with ITO layer $t_1 = 85\,nm$. g-h) The CIE chromaticity xy coordinate plots with the corresponding points for the measured transmittance at 0° (T_0) and reflectance at different angles from 50° to 70° ($R_{50} - R_{60} - R_{70}$) for the two ITO-based MIMI. The red and blue squares indicate the points related to numerical transmittances and reflectances, respectively. Figure readapted from reference [139].

ITO-based is given by the zero reflection in the s polarization at the resonant wavelengths see Figure 2.10 a and d. In order to support the experimental results, the two reflectances (p- and s-pol), transmittance, as well as Ψ and Δ, have been numerically evaluated and reported in Figure 2.10b-c and e-f for the MIMI (A) and MIMI (B). A further investigation, performed using

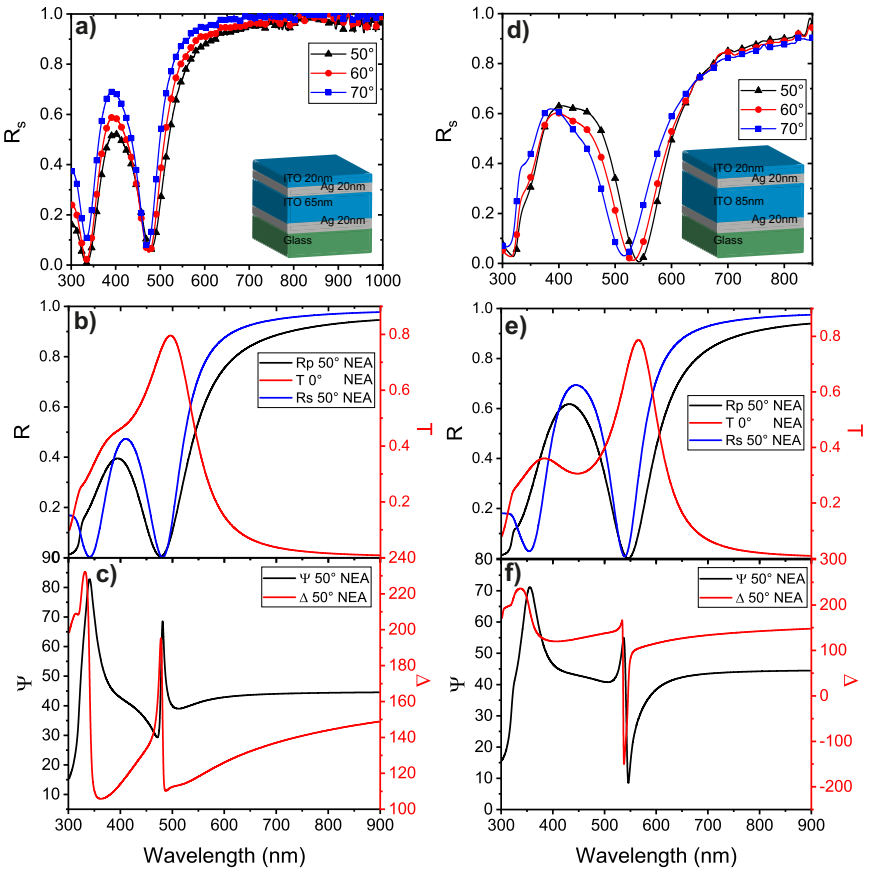

FIGURE 2.10: a) Reflectance (s-pol) at different incident angles for the system made by the ITO slab of 65 nm. b,c) Numerical results for reflectances (p and s-pol) and transmittance, Ψ and Δ. d)Reflectance (s-pol) at different incident angles for the system made by the ITO slab of 85 nm. e,f) Numerical results for reflectances (p and s-pol) and transmittance, Ψ and Δ.

COMSOL Multiphysics, concerns the study of the interaction of the electromagnetic field ($\mathbf{E}$) with the entire system, that is at the base of the formation of the coupled plasmons. Figure 2.11 shows the electric field maps, at resonance ($\lambda = 480\, nm$) and out of resonance ($\lambda = 700\, nm$), for the MIMI (A) for an incidence angle $\theta = 50°$. In particular, it is possible to observe that most part of the electric field at the resonance is confined in the dielectric layer of the nano-cavity, exhibiting a single (high or low energy) mode, while the remaining part passes through the system, see Figures 2.11a-c. In fact, as highlighted in the first section, a p-pol incident wave induces the formation of the main low energy mode from the SPPs hybridization, that decays inside the dielectric cavity, while the s-pol wave excites a high energy mode (GSP). On the contrary, the out of resonance condition causes the total reflection of the electromagnetic field, with no interaction with the ITO cavity

layer (see Figures 2.11b-d). The electric field maps related to the MIMI (B) at the resonant wavelength ($\lambda = 532\,nm$) are illustrated in Figures 2.11e-g and out of resonance ($\lambda = 700\,nm$) in Figures 2.11f-h. In order to investi-

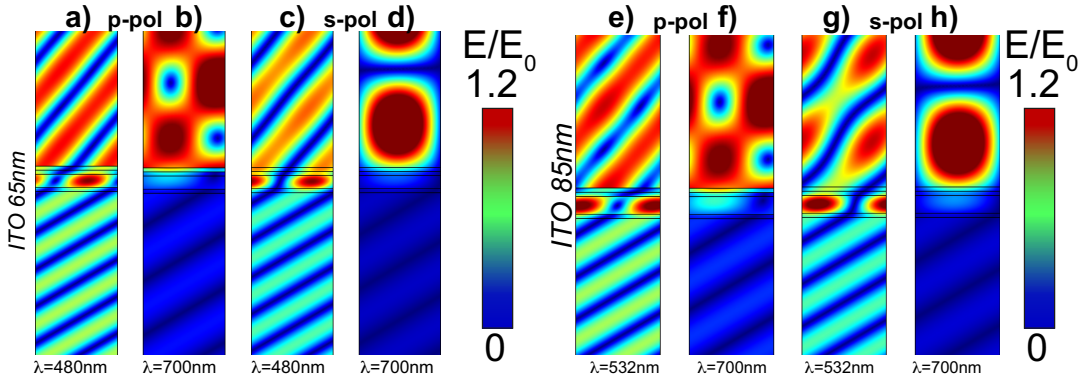

FIGURE 2.11: Electric field maps for the MIMI(A) composed of Ag/ITO/Ag/ITO with thicknesses of $20/65/20/20\,nm$ respectively evaluated at an incidence angle of 50°. a , c) at the resonant wavelength of $\lambda = 480\,nm$ for p- and s-polarization where the resonant mode inside the ITO nano-cavity is shown. b, d) Out of resonance at $\lambda = 700\,nm$ for both polarizations. Electric field maps for the MIMI(B) composed of Ag/ITO/Ag/ITO with thicknesses of $20/85/20/20\,nm$ respectively evaluated at an incidence angle of 50°. g , h) at the resonant wavelength of $\lambda = 532\,nm$ for p- and s-polarization where the resonant mode inside the ITO nano-cavity is shown. f, h) Out of resonance at $\lambda = 700\,nm$ for both polarizations. Figure readapted from references [139].

gate how the plasmonic coupling is strongly related to the color change as a function of the incident/viewing angles, experimental measurements of the real and imaginary part of the pseudo dielectric function are reported. These quantities are identified in the following as $< \varepsilon_1 >$ and $< \varepsilon_2 >$. Figure 2.12a reports the pictures of the MIMI (A) showing different colors as a function of incident/viewing angle, how it is observed in bottom and upper-right frames. At small angles, instead, the system lets a blue color pass through it, while the reflected light appears gold (upper-left frame of Figure 2.12a). The dashed white line indicates the real MIMI sample. As a consequence of the behavior of Ψ and Δ, the shape of the pseudo dielectric function, especially in its imaginary part $< \varepsilon_2 >$, shows an abrupt change in proximity to the resonance wavelength. The intrinsic formation of GSPs (high energy modes) and SPPs (low energy modes) inside the cavities produces a sign change in the $< \varepsilon_2 >$. In fact, it becomes negative when the dispersion curve matches the GSP and positive for the losses generated by the SPP. This unexpected change at the resonant wavelengths can be used to recognize, in a fast and effective way, the presence and spectral position of plasmon modes into the whole system. The $< \varepsilon_2 >$ graph for the MIMI (A) presents the abrupt change at the resonant wavelength ($\lambda = 480\,nm$) for incident angle of 60°, while the other excited mode (with very low value) is observed around the Ferrel-Berreman mode of silver ($\lambda = 327\,nm$)[104], see

Figure 2.12b. In case of the MIMI (B), the observed colors are different, passing from green to purple, as illustrated in bottom and upper-right frames of Figure 2.12c. At small angles, the system now allows seeing through it with a green colored shadow whereas the reflected light is purple (upper-left frame of Figure 2.12c). These features are related to the increased thickness of the cavity layer and thus to the different resonant wavelength. The experimental $< \varepsilon_2 >$ curve, reported in Figure 2.12d, confirms the position of the resonant wavelengths that cause the system coloring, around $\lambda = 532\,nm$ for an incident angle of 70°, whereas a moderate second excited mode is observed at $\lambda = 380\,nm$. The Ferrel-Berreman mode is still present. In order

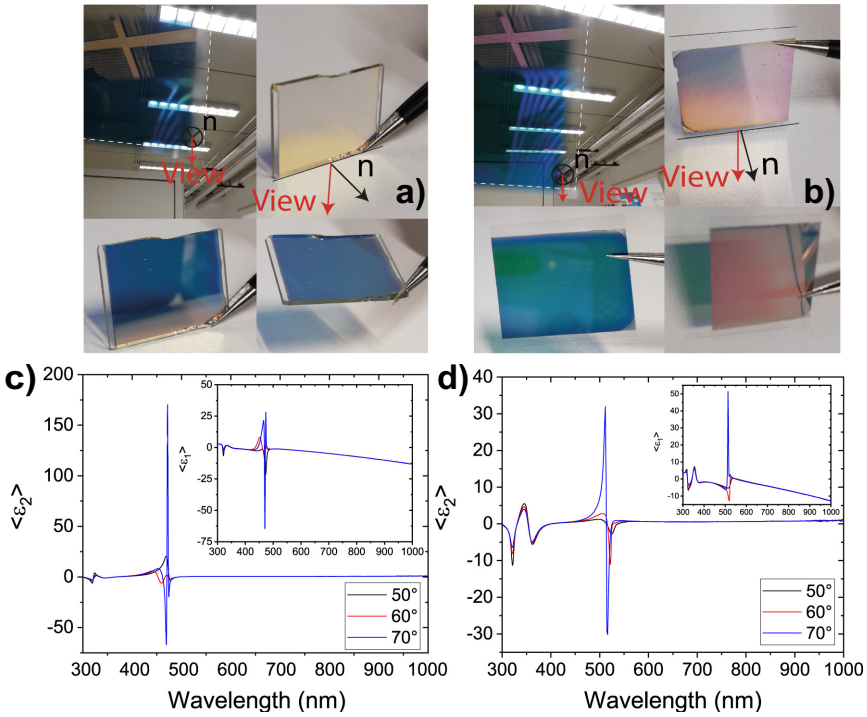

FIGURE 2.12: a) The four pictures are referred to the MIMI (A). The color of the MIMI passes from blue to gold when observed in transmission or in reflection, respectively. b) The graph reports the $< \varepsilon_2 >$ at three different incident angles while the inset depicts the $< \varepsilon_1 >$.c) The pictures are referred to the MIMI (B). The nano-cavity color passes from green to purple when it is observed in transmission or in reflection, respectively. d) The graph shows the $< \varepsilon_2 >$ at three different incident angles, while the inset shows the $< \varepsilon_1 >$ behavior. Figure readapted from reference [139].

to enhance the performance of the plasmonic MIMI nano-cavities, ZnO has been used as insulator element instead of ITO. ZnO is largely used in nanoscience thanks to its excellent features in photovoltaics [140, 141], extreme non linearity applications as second harmonic generation [142, 143] and photocatalysis [144, 145] just to name a few. The nano-cavity is now composed of Ag(20 nm)/ZnO(83 nm)/ Ag(20 nm)/ZnO(20 nm), see the inset of Figure 2.13b. The proposed MIMI presents the same optical properties of the previous one: experimentally measured transmittance at normal incidence reaching 55% at the resonant wavelength ($\lambda = 530\,nm$), and 0% reflectance around

$\lambda = 520\,nm$ (Figure 2.13a). As for the systems with ITO, GSPs and SPPs arise inside the ZnO MIMI when an s-polarized wave is reflected from the surface, R_s presenting a value close to 0% at the resonance wavelength ($\lambda = 530\,nm$), see Figure S6a. These features (R_p and $R_s \sim 0\%$) are associated to a sharp Ψ and Δ behavior close to the same wavelength (Figure 2.13b-c), paving the way to exploit the enhanced Goos-Hänchen shift for sensing applications. As done for the previous cases, the CIE chromaticity xy-coordinates have been calculated and reported in Figure 2.13d. The ZnO-based MIMI presents purple-pink color hues for the reflectances indicated with the white dots on the plot $R_{50} - R_{60} - R_{70}$, while the transmittance related point T_0 identifies a green component. The numerical transmittances and reflectances at different incident angles have been calculated and the related points reported in the CIE chromaticity xy-coordinate maps with red and blue squares, respectively. This nano-cavity, due to the prominent behavior of Ψ and Δ at each incident angles, presents a remarkable angle-dependent color change, passing from green to shades of purple. In comparison to the ITO-based systems, one resonance allows transmitting the green hue of light, producing instead a purple reflection, as visible in Figure 2.13e. This ZnO-based system works better as filtering component at the resonant wavelength due to the less influence of the Ferrel-Berreman mode. In this system, the pseudo $< \varepsilon_2 >$ is about one order of magnitude larger than for the ITO-based MIMIs, reaching absolute values of about 500 around $\lambda = 530\,nm$, and for an incident angle of 50° (Figure 2.13f). It is remarkable that at an incident angle of 60° and 70°, the sign change in $< \varepsilon_2 >$ is still present with values comparable to the ITO-based system. This noticeably high singularity can be used to identify the presence of plasmonic modes inside the εNZ nano-cavity.

Due to their self-momentum matching, the proposed MIMI systems allow realizing sub-wavelength plasmonic cavities. They can be exploited for future applications as sensors, especially considering the giant enhanced Goos-Hänchen shift that can be reached and its effects [164, 167, 168], as well as for photovoltaics layers, plasmonic color filtering for CMOS sensors [169], plasmonics for multiple uses [170], active nano-optics [171–175]. The strong Ψ or Δ optical responses (as well as the sharp pseudo dielectric function) could be exploited also as physical unclonable functions, used as fingerprints in anti-counterfeiting applications. [176–178].

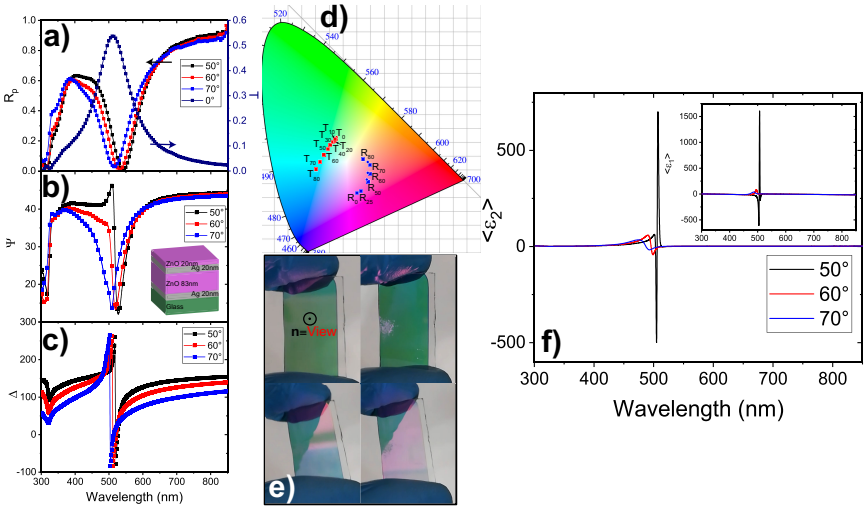

FIGURE 2.13: a) Reflectances (p-pol), and transmittance at different incident angles for the MIMI (Ag(20 nm)/ ZnO(83 nm)/ Ag(20 nm)/ ZnO(20 nm)). b,c) Ψ and Δ curves for the fabricated nano-cavity, the inset reports a schematic view of the MIMI with the related thickness of each layer. d) The CIE chromaticity xy coordinate plots with the corresponding points for the measured transmittance at 0° (red dot T_0) and for the reflectance at different angles from 50° to 70° (blue dots $R_{50} - R_{60} - R_{70}$). The red and blue squares indicate the points related to numerical transmittances and reflectances, respectively. e) Pictures referred to Ag/ZnO/Ag/ZnO system taken at different incident/view angles. f) $< \varepsilon_2 >$ at three different incident angles, while the inset shows the $< \varepsilon_1 >$ curves. Figure readapted from reference [139].

2.7 Conclusion

In conclusion of this Chapter, I would like to remark that most of the obtained results were possible because of the reliability of the numerical predictions obtained by exploiting the NEA numerical tool developed by myself and my coworkers. In fact, a comprehensive optical analysis of different nanoscale structures has been presented. As a crucial test-bed of the tool, optical features as reflectance, transmittance, as well as the ellipsometric angles Ψ and Δ have been calculated in presence of systems with increasing structural complexity, from single metal layers to asymmetric multi-layers behaving as optical nano-cavities for light. The latter configuration shows a peculiar metamaterial behavior originating from its unusual effective medium properties, that can be efficiently exploited in sensors applications. Indeed, in specific spectral windows, the asymmetric multi-layer with a full thickness of hundreds of nanometers shows a hyper transmission of light with respect to a single 20 nm-thick Ag layer. The resulting comprehensive analysis of considered nanoscale systems has shown an excellent agreement between numerical and experimental curves. This confirms the effectiveness of the tool as a significant instrument for nanotechnology design and fundamental research in nano-science. Then, by exploiting this same numerical tool, I fabricated different samples with very interesting optical features such as: color gamut, zero reflectance, extraordinary transmittance, sigmoidal behavior of

the parameters Ψ and Δ, and peculiar singularities in the real and imaginary part of the pseudo dielectric function, $< \varepsilon_1 >$ and $< \varepsilon_2 >$, at the resonant wavelengths. These noticeably high singularities permit to identify the presence of plasmonic modes inside the εNZ nano-cavities. Due to its double metal-insulator interface, the MIMI configuration, exhibits high (GSP) and low (SPP) energy modes which can be excited in free space without momentum matching. Hence, all the optical properties of the the proposed MIMI nano-cavities allow using them as sensors due to the remarkable dephasing that paves the way to exploit an enhanced Goos-Hänchen shift. Furthermore, the spontaneous color enabling behavior provided by the propagation of plasmonic modes in these nanocavities represents a promising possibility for filtering, physical unclonable functions and photonics applications.

Chapter 3

The MIMI device prototype for the Hyper Resolution in two photon direct laser writing (TP-DLW) process

In this Chapter, I am going to highlight how the main aspects detailed in the previous chapters play a fundamental role to fabricate structures with nanoscale features by exploiting a two-photon direct laser writing (TP-DLW) lithography process enhanced to hyper resolution capability by an ε_{NZ} metamaterial substrate. The metamaterials detailed in the previous Chapter (MIMIs) represent an open challenge in the applied nano-material science. Here, I am interested to exploit their extraordinary optical features to fabricate a substrate behaving as an on-chip device. Thanks to the high collimation enabled by the extraordinary ε_{NZ} metamaterial features, ultra-thin dielectric hyper resolute nano-structures are within reach. Once, the design of the MIMI is done to exploit this features, a first attempt of hyper resolution is shown fabricating 1D gratings. With respect to the standard direct laser writing approach, a size reduction of 89% and 50%, in height and width respectively, is achieved with the height of the structures adjustable between 5 nm and 50 nm. The possibility to improve the resolution of the two-photon lithography leads to a novel open scenario of meta-surfaces fabrication and on site devices. Then, to complete the overview of new fascinating hyper resolute two photon polymer curing, a highly detailed dielectric bas-relief (500 nm of full height) of Leonardo Da Vinci's *"Lady with an Ermine"* has been realized. The proof-of-concept result shows intriguing cues for the current and trend-setting research scenario in anti-counterfeiting applications, flat optics and photonics.

3.1 One and two-photon lithography

In this first section we resume the main principles of one and two-photon lithography process in order to easily understand how myself and coworkers succeeded to find a way to improve the resolution of that process. Optical lithography is one of the most used and developed micro-fabrication technique [179–181]. The technique is based on the use of a photo-resist: a mixture of a reactive monomer, a solvent and a photo-initiator, spread in

liquid phase onto a solid substrate. By tuning the resist viscosity when a spin-coating process is used, a thin film, of thickness finely controlled, typically in the range 0.5 - 100 μm, is deposed on a substrate. On such film, features are impressed with ultraviolet (UV) light exposure through a mask. Resists are available in positive and negative tone. A hole in the mask will create a hole in a positive tone photoresists, whereas it will create a pit in a negative tone photoresist [181]. Let us focus on this last family (the other behaves in the symmetrical way): when a negative tone photo-resist is irradiated with ultraviolet light, the photo-initiator creates free radicals, whose interaction with the nearby monomers generates a crosslinking chain reaction. Polymerization keeps on propagating until either two different interacting radicals form a stable species, or the radicals are quenched due to interaction with non-inert gas present on the environment. To obtain high-quality results, polymerization has to occur completely during the UV light exposure. Therefore, it is mandatory to perform the process under an inert gas atmosphere and to exactly tune it according to the characteristic of the selected photo-resist. It has to be considered that photo-lithography works efficiently if applied on thin film. Light goes through the holes inside of the mask, but diverts inside the bulk of the photoresist film, according to its thickness. The mask screens the areas of the film that aren't to be exposed and structures 1D or 2D can be created in the photo-sensitive resin, with a resolution down to few micrometers, diffraction limited. The exposed resin polymerizes and the remaining non-exposed material is removed bathing the sample in a solvent. As a result, it is obtained a strongly adhering layer of controlled thickness, structured in islands reproducing the shape of the uncovered areas in the mask. This pattern can be hence used as a protective layer in a subsequent wet hatching process, as in the case of the silicon chips in the microelectronic domain, or as a mold in order to imprint the features in another material (soft lithography) [181]. The last is the standard technique used for fabricating microfluidic devices, where the microfluidic network is impressed in a polydimethylsiloxane (PDMS) block. PDMS is the most widely used silicon-based organic polymer, and is particularly known for its unusual rheological properties, allowing to fill and reproduce even the finest details, down to few nanometers. Because of his chemical-physical properties, PDMS is widely used in microfluidics [182–185], opto-fluidics [186, 187] and bio-technologies [188], as it is optically clear and biocompatible. A chrome on glass mask, with the desired patterns, was put upon the cooled photo-sensitive films, taking care to face the chrome side to the resist film. Polymerization was performed by using a led UV source ($\lambda = 365\,nm$), with output intensity of $1.18 mW/cm^2$ and exposure time of 10 min. A post-exposure baking at 95°C for 5 minutes was performed in order to complete the polymerization of the exposed areas. The film was left to cool for 10 minutes, and developed in a bath of 1-Methoxy-2-propyl acetate for 5 minutes, then the solvent was washed out with a bath in isopropyl alcohol (IPA) for 10 seconds. A hard-backing step at 145° C for 30 minutes was carried out to better fix the structures on the substrates and to ensure that their mechanical properties don't change during thermal treatments.

Two-photon Absorption

Direct laser writing (DLW) is a laser scanning fabrication technique allowing to maskless print structures into a photoresist, with a resolution depending solely on the output power and beam waist of the used laser beam [189–191]. When the optical absorption is governed by single photons processes, this technique allows for 3D patterning with resolutions down to typically few microns, in the same order of that given by the mask lithography. A huge improvement is achieved combining DLW with the two-photons absorption (TPA). In fact, exploiting the dependence of the TPA on the squared intensity and the presence of a threshold, features of hundreds nanometers, thus well below the diffraction limits can be created. TPA is an optical process, theoretically predicted in 1930 by Maria Goeppert-Mayer [192], and then experimentally observed in 1961 by Kaiser and Garret [193]. As shown in Fig. 3.1, a photon absorption excites a molecule from the ground energy level to a singlet excited energy level E_e, according to the process:

$$\Delta E = E_e - E_g = \hbar\omega_a \tag{3.1}$$

Where $\hbar$ is the reduced Planck constant, ω_a is the angular velocity of the absorbed photon. The excited singlet level is typically unstable, therefore the system may lose energy and decay to a more stable intermediate energy level E_i, from which it may create a chemical bonding with other activated molecules, or it may release energy in a radiative (through an emitted photon which will have $\omega_e < \omega_a$), or non-radiative (local heating) way. According to the Goeppert-Mayer's theory, the molecule may also be excited by the simultaneously absorption of two photons $\hbar\omega_k$ and $\hbar\omega_l$. This is a optical non-linear process involving the third order susceptibility, much smaller the main term responsible of the ordinary optics. Therefore, in order to observe TPA, a huge photon density is required [189–191], as in the case of a tightly focused laser beam. In general, TPA has to fulfill the condition:

$$\Delta E = \hbar\omega_a = \hbar\omega_k + \hbar\omega_l \tag{3.2}$$

In this case, the system is firstly excited to a virtual level E_v, whose lifetime $\Delta t \sim \hbar/\Delta E_k$ is typically in the order of 10^{-15}s, and then to the excited level E_e. If a single laser source is used, each photons has energy:

$$\hbar\omega_k = \frac{\hbar\omega_a}{2} = \frac{\Delta E}{2} \tag{3.3}$$

The activation rate through TPA is strongly different in respect to the single photon absorption (SPA). For organic photo-resist, typical values of the SPA cross-section σ are in the order of $10^{-16}cm^2$, while the TPA cross-section σ_2 is in the order of $10^{-50}cm^4s$ [189]. The SPA cross-section σ can be calculated according to Beer's law:

$$I(x) = I_0 e^{-\alpha c x} \tag{3.4}$$

Where: I is the laser intensity, $\alpha = \sigma N$ is the SPA absorption coefficient, N is the molecular number density, c is the molecular concentrations and x the

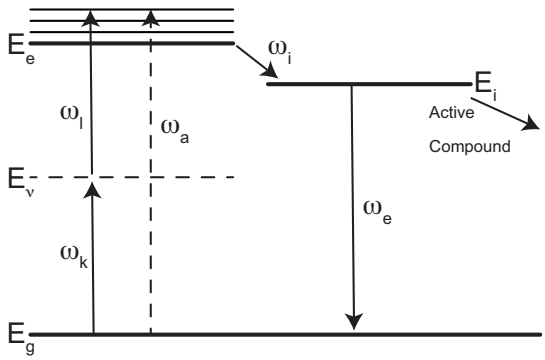

FIGURE 3.1: Energy level diagram for a molecule excited by a single photon (dotted line) or by two photons (straight line), from the ground level to an excited level. In both case, the compound may be activated or may release energy through radiative or non-radiative processes. Figure readapted from reference [189]

path length. In the TPA case the eq. 3.4, becomes:

$$I(x) = \frac{I_0}{1 + \beta c x I_0} \tag{3.5}$$

In which $\beta = 10^{-3}(\sigma_2 NAc)/\hbar\omega$ is the TPA absorption coefficient, NA is the Avogadro number, and σ_2 the TPA cross-section. If follows that σ_2 is a function of the square of the laser intensity [190].

Two-photon Polymerization

Through the TPA process, when an ultrafast near infrared (NIR) laser is focused on a UV-sensitive resin, polymerization is activated only in a very small volume inside the focus. This is the smallest polymerizable volume, usually called volume pixel (voxel) and defines the resolution of the photo-polymerization process [189–191]. Two-photon polymerization (TPP) presents two energy thresholds, as shown in Fig. 3.2. The first one is the polymerization threshold, which depends on the laser intensity and the material cross-section σ_2. Only the portion of the Gaussian profile of the laser intensity that exceeds the threshold leads to local polymerization. Thus, the voxel dimensions strongly depend on the incident laser beam intensity. The second threshold is defined by the onset of the optical breakdown of the polymer: when the laser intensity is higher than this threshold, explosions can even occur and the resin is permanently damaged. Sweeping the laser beam into the photo-resist, is thus possible to create bi- and three-dimensional polymeric structures, whose resolution is given by the size of the voxel. A prediction of the diameter and length of a voxel is thus necessary to create refined 3D objects. The diameter d and the length l of the voxel are:

$$d(P,t) = r_{\omega_0}\sqrt{ln(4\frac{P^2 t}{\nu t_L (r_{\omega_0}\pi \cdot \hbar\omega)^2}\frac{\sigma_2}{ln(\frac{\rho_0}{\rho_0 - \rho_{th}})})} \tag{3.6}$$

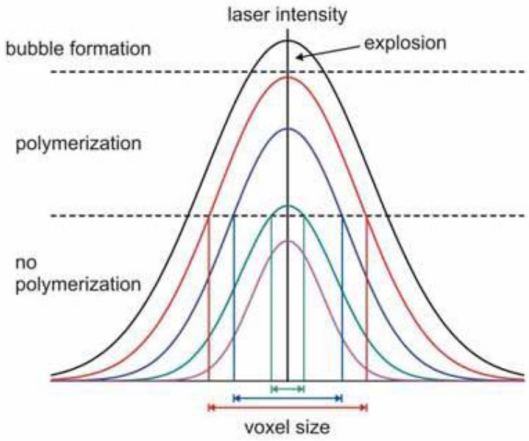

FIGURE 3.2: Laser intensity dependency of the voxel size. If the laser intensity is below the polymerization threshold no polymerization happens, else only the portion of the Gaussian beam higher than the threshold will lead to the voxel polymerization. Over the second threshold, the resist explodes and is permanently damaged. Figure readapted from reference [189]

$$l(P,t) = 2z_R\sqrt{\sqrt{ln(4\frac{P^2t}{\nu t_L(r_{\omega_0}\pi\cdot\hbar\omega)^2}\frac{\sigma_2}{ln(\frac{\rho_0}{\rho_0-\rho_{th}})}}} \tag{3.7}$$

The voxel length and diameter depend then on the laser power P, the exposure time t and the TPA cross-section σ_2. The other terms are related to the materials and optical system used. $r_{\omega_0} = 0.61\lambda/N.A.$ is the beam waist, $z_R = \pi r_{\omega_0}2/\lambda$ is the Rayleigh length, ν the pulsed laser repetition rate, t_L the single pulse width, $\hbar\omega$ the energy of the incident photon, $\sigma_2^* = \sigma_2/ln[\rho_0/(\rho_0?\rho_{th})]$ is the effective cross section for the TPA, ρ_0 and ρ_{th} are the initial density and the threshold density of radicals respectively.

Two-photon Direct Laser Writing: from the standard technique to the new implementation

The TP-DLW by Zeiss (NanoScribe) system used presents a femtosecond Ti:Sapphire ($\lambda = 780\,nm$) laser connected to an inverted microscope. The laser beam is focused on the sample through a $63X$ or $25X$ objective, with N.A. respectively of 1.4 and 1.1. 3D structures can be fabricated both through the glass, and by the diving the objective in the resist (Fig. 3.3a). During the printing process, the working distance of the objective (typically $350-400\mu m$) has to be taken in consideration when the TP-DLW is performed through the glass. Moreover, since the writing process occurs plane by plane, to create the highest parts of a structures, the laser beam has to go through the objects already created and is attenuated, generating smaller effective voxels. By working with the objective immersed in the resin, it is possible to create 3D object with theoretically no vertical limits (Fig 3.3b). However, fluid-dynamic effects may occur while moving the lens and affect the final result. Here, after this wide but necessary introduction of the two-photon polymerization I want to explain how is possible to increase the resolution in

terms of voxel sizes. To improve the lithography process I, with my coworkers, exploited a MIMI deposited by DC sputtering on a classical substrate used for the TP-DLW (Fig. 3.3c). Nowadays, the science of nanotechnology moves forward to rich some goals in the super resolution direction [180]. Systems involved chemical reagents to increase the resolution as the modification of the photo-resin [194], or more complex process as the modification of the initiation and deactivation polymerization by a gain medium achieving a resolution of $\sim \lambda/20$ [195]. Some results are also achieved by the TP-DLW in terms of 3D structures but at the microscales[194], they are exploited in order to perform the already existing technique, these are used for fiber tip fabrication [180] and high resolution of 3D systems in hydrogels [196]. As reported from *Zhang et al.* [194] the progress of femtosecond laser direct writing in the last decades the results that merit some notes reach results as resolution of 100 *nm* for microstructures by the use of radical quenchers [197], 40 *nm* fro micro-devices by an activation beam [195], of 25 *nm* and 20 *nm* for MEMS and micro-optics by the scan speed manipulation and self-smoothing effect [198, 199], the use of photosensitive sol-gel for micro-optics [200], just to name a few. Another way is possible exploiting the mechanical strategy as the change of the interface hight, in that case is possible to reach a results of a single line width and hight around 100 *nm* [201].

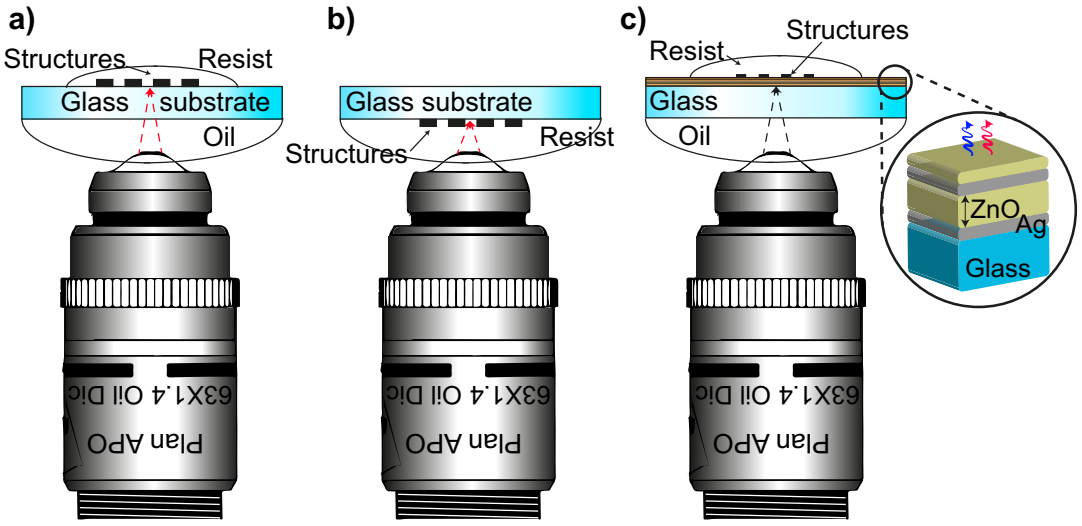

FIGURE 3.3: The sketch shows the two main approaches for TP-DLW and our implementation. a) Laser writing from the bottom using a matching oil and the photo-resin on the top substrate, b) the object is dipped into the resist. c) The sketch presents the coating MIMI metamaterials on the substrate that allows enabling the hyper resolution in the TP-DLW process.

Our proposed implementation can be result useful thanks the simplest way of utilization. It is a completely different approach, it involves optical epsilon-near-zero (ε_{NZ}) nano-cavities in a metal/ insulator/ metal/ insulator (MIMI) configuration [139] deposited on a standard coverslip already used in the TP-DLW processes. These systems pave the way for the realization of very versatile devices with unusual optical features. In this chapter, the

extraordinary self-collimation of light, enabled by a MIMI plasmonic metamaterial, is proposed as a ground-breaking possibility to improve the resolution of TP-DLW lithography [202, 203]. In particular, nanostructures with typical sizes of few tens of nanometers are within reach in few minutes writing time. It also exploits the near field but it does not require a SNOM tip or an aperture to confine the incident electric field as done in past study [204]. As well know, near field is widely used for super resolute imaging and the two-photon is exploited especially by fluorescence [205–207].

3.2 MIMI device for TP-DLW process

As illustrated in Fig. 3.3c, it is possible to drastically increase the resolution in terms of voxel sizes by using a MIMI directly deposited on a classical glass substrate used for the TP-DLW. The inset reports a schematic view of the MIMI constituted of a silver layer with thickness $t_{Ag} = 30\,nm$, a thicker ZnO layer working as an optical nano-cavity (t_{cav}), another silver layer with the same (t_{Ag}) thickness and a final thin ZnO layer ($t_{ZnO} = 30\,nm$). In order to obtain the hyper-resolute TP-DLW process, it is necessary that operating/writing wavelengths ($\lambda = 780\,nm$ and $\lambda = 390\,nm$) are let through the MIMI nano-cavity as depicted on the sketch of Figure 3.4a. By using a Finite Element Method (FEM) model, based on numerical ellipsometer analysis (NEA)[93], and by varying the thickness of the dielectric nano-cavity (t_{cav}), it is possible to retrieve the thickness value to obtain the minimum in reflectance and the maximum in transmittance for a normally incident wave at the two above mentioned wavelengths. In our case, the cavity thickness is 160 nm that actually supports the plasmonic resonant modes marked with dashed white lines in the reflectance and transmittance maps reported in Figure 3.4b and Figure 3.4c, respectively. A further validation of the occurrence of double modes is provided by a modified effective medium theory (EMT), taking into account the experimental retrieved dielectric constant and the thickness of each layer [208, 209]. Here, the implemented EMT reports the modified $\tilde{\varepsilon}_{\parallel}$ and $\tilde{\varepsilon}_{\perp}$ equations:

$$\tilde{\varepsilon}_{\parallel} = \frac{\tilde{\varepsilon}_{m1}d_{m1} + \tilde{\varepsilon}_{d1}d_{d1} + \tilde{\varepsilon}_{m2}d_{m2} + \tilde{\varepsilon}_{d2}d_{d2}}{d_{m1}d_{d1}d_{m2}d_{d2}} \tag{3.8}$$

$$\tilde{\varepsilon}_{\perp} = \frac{\tilde{\varepsilon}_{d1}\tilde{\varepsilon}_{m1}\varepsilon_{d2}\tilde{\varepsilon}_{m2}(d_{m1}d_{d1}d_{m2}d_{d2})}{\tilde{\varepsilon}_{m1}d_{d1} + \tilde{\varepsilon}_{d1}d_{m1} + \tilde{\varepsilon}_{m1}d_{d2} + \tilde{\varepsilon}_{d2}d_{m1} + \tilde{\varepsilon}_{m2}d_{d2} + \tilde{\varepsilon}_{d2}d_{m2}} \tag{3.9}$$

This analysis shows the double ε_{NZ} behavior of the proposed MIMI nano-cavity presenting the zero crossing point between the real perpendicular $Re\{\varepsilon_{\perp}\}$ and parallel $Re\left\{\varepsilon_{\parallel}\right\}$ dielectric constant very close to the two operating wavelengths, see Figure 3.4d. In case of off-normal light incidence on the same MIMI (θ_i varying from 0° to 80°), reflectance and transmittance curves are reported in Figure 3.5. Experimental curves are measured by analyzing the fabricated MIMI by means of a V-VASE ellipsometer Figure 3.5a, c, e ,g for reflectance and transmittance p- and s-pol, respectively, while the numerical analysis is performed again by the NEA model Figure 3.5b, d, f, h. The

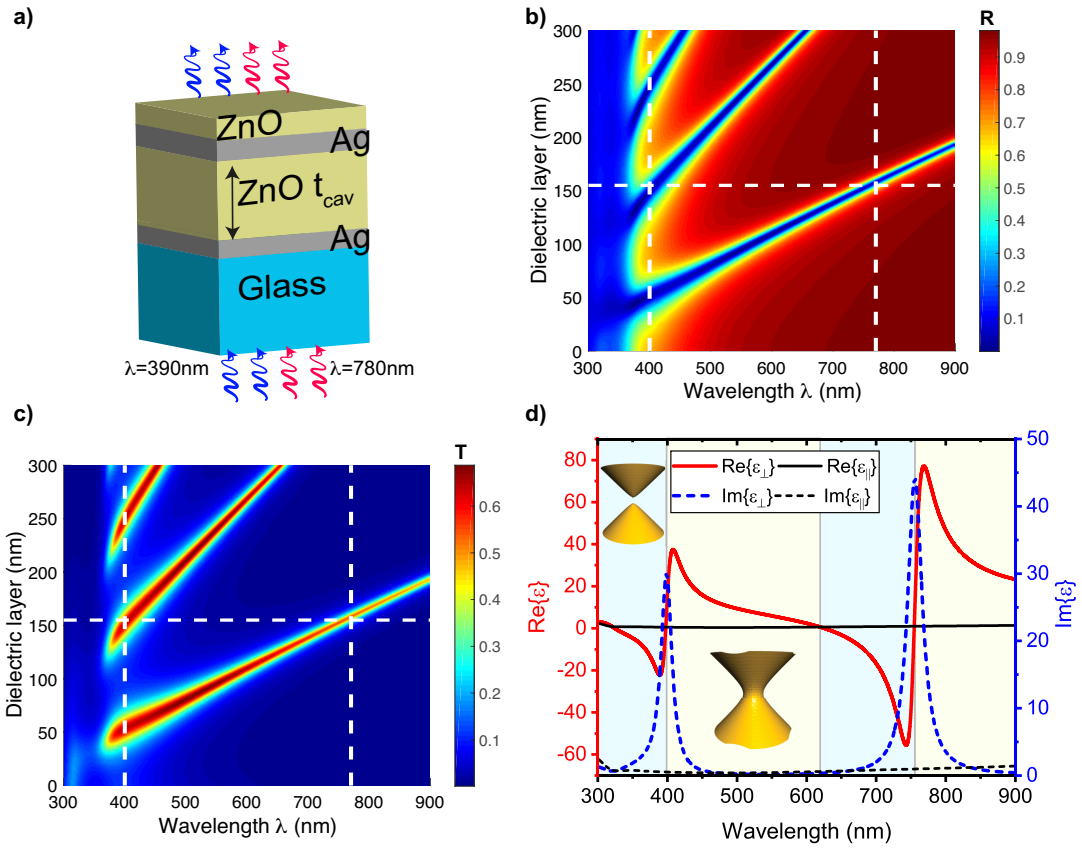

FIGURE 3.4: a) A sketch of the MIMI nano-cavity. b-c) Numerical reflectance and transmittance map, respectively, at normal incidence varying the ZnO thickness that constitutes the optical nano-cavity. The value of $t_{cav} = 160\,nm$ has been choose to obtain a minimum in reflectance and maximum in transmission at $\lambda = 400\,nm$ and $\lambda = 780\,nm$. d) Effective medium theory (EMT) calculated for a four layer system showing the ε_{NZ} modes at the two resonant wavelengths. Figure readapted from reference [202, 203].

high-level reliable agreement between numerical and experimental results confirms the possibility to exploit the MIMI for TP-DLW with a focused ($\lambda = 780\,nm$) laser beam at normal incidence. As reported in these studies, the use of a MIMI system allows enabling the two modes for the s-pol and not only for the p-pol this feature offers the possibility to use it for a TP-DLW source with TE or TM polarization. As reported in past studies and in Chapter 1 the ε_{NZ} metamaterials have the remarkable ability to canalize and collimate light[210–214]. The propagation of light within these metamaterials has been described in section 1.2.1. For the considered MIMI nano-cavity, the $\theta_{res-cone}$ (see equation 1.5) has been calculated using the parallel and perpendicular dielectric constant retrieved by the EMT. As reported in Figure 3.7a, the MIMI nano-cavity presents two points where the resonant cone angle is zero meaning that, for $\lambda \sim 400\,nm$ and $\lambda \sim 770\,nm$, the light passing through the MIMI remains completely collimated. However, the operating/writing wavelengths present a resonant cone angle of max 5° as highlighted by the grey squares. The latter indicate wavelengths in a range of $\pm 10\,nm$ respect to

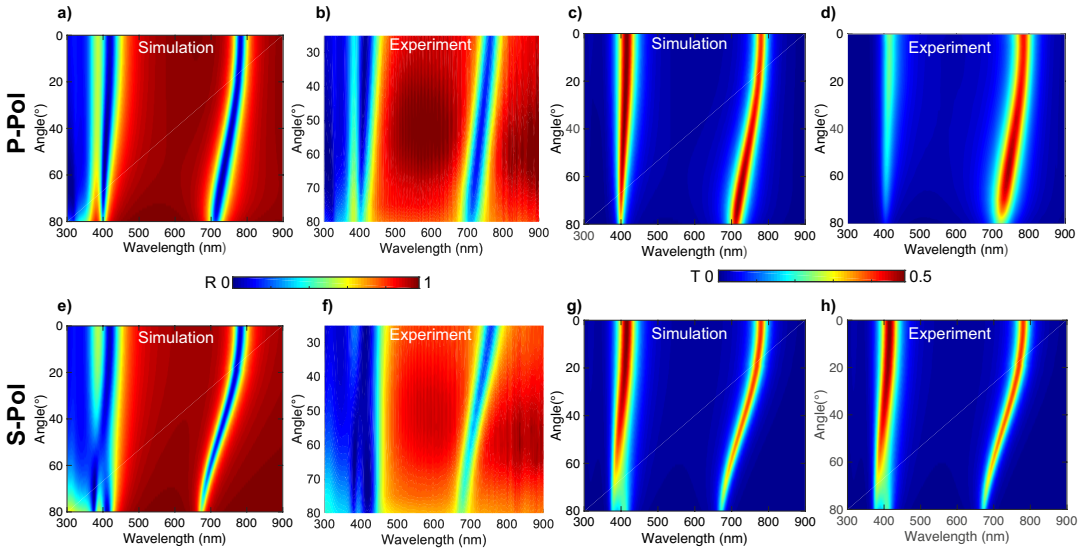

FIGURE 3.5: a-b) Numerical and experimental reflectance p-pol, c-d) numerical and experimental transmittance p-pol e-f) Numerical and experimental reflectance s-pol and g-h) numerical and experimental transmittance s-pol map at different incident angle for the MIMI device showing the two minimum and two maximum respectively at $\lambda = 400\,nm$ and $\lambda = 780\,nm$.

the wavelength where the resonant cone angle is zero. Due to the incident angle independency in the EMT and $\theta_{res-cone}$ calculation, the mismatch in terms of desired and evaluated wavelengths is not worrisome. The $\theta_{res-cone}$ and the beam behavior is experimentally confirmed by the use of a homebuilt confocal setup. The optical setup used to analyze the Point Spread Function (PSF) characterization is composed as following. A collimation line for the white light that is produced by from a Xenon lamp is realized with a 40X objective and a fiber coupler mounted on a 3-axis stage. The collimated beam is sent to the main confocal line. On the same optical path, it has been placed another 3-axis stage with a 10x/50x objective used to focalized the beam on the sample (S) under investigation. Then, a 32x objective collects the signal from the sample and collimates it into the detector that is represented by a beam profiler (BP) Thorlabs BC106N-VIS spectral range from 350 nm to 1100 nm mounted on a double-axis stage. A lens collects the signal from the objective and sent it on the BP ccd. In the middle of this path there is the sample mounted on a holder stage that allows controlling micrometer movement. The sample is moved forward and backward along Z in order to collect the beam divergence. Between the fiber collimator and the first objective it has been placed a beam splitter that sends the light from lamp or from the lasers in the main path. The laser line is composed by different lasers. For example a blue laser impinges on a dichroic mirror (DM1) that reflects the green and leads both lasers on a beam splitter (BS1) that collects the red laser and sent all lasers on the second beam splitter (BS2). In order to measure the input power a flip mirror (FM) is placed after the 32$\times$ objective and the signal is sent on a Thorlabs power meter (Pm) head (model S130VC). The whole described setup is depicted in Figure 3.6.

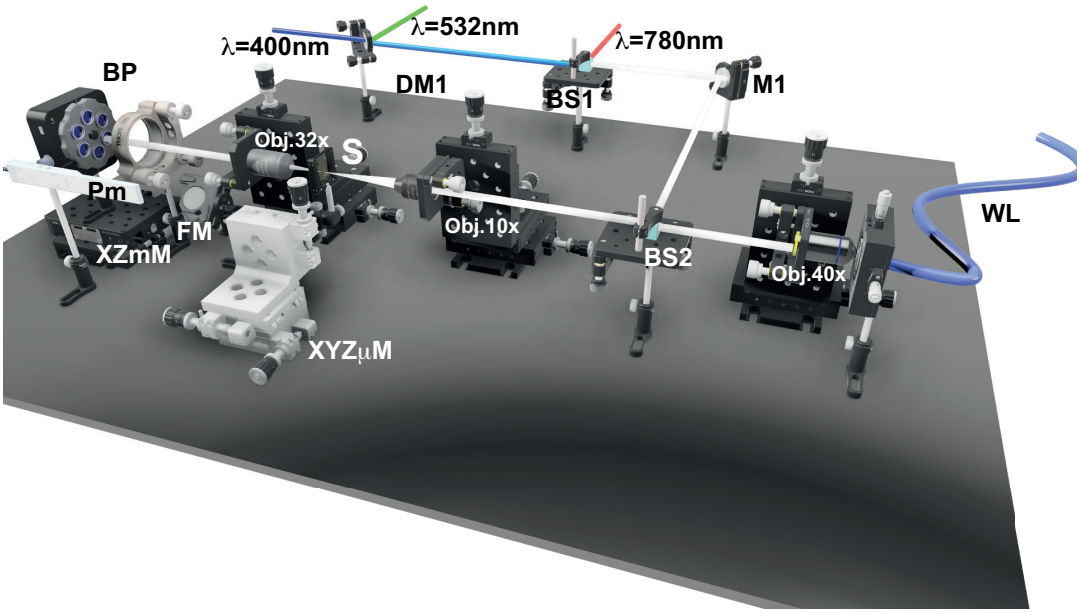

FIGURE 3.6: Schematic view of the optical setup used to fully characterize the produced PSF through the MIMI device and the bare glass substrate

The MIMI is compared with a standard glass substrate (glass coverslip $22X22X0.15mm$) used in TP-DLW, the produced focalized spot is measured in order to estimate the beam shrinking by the point spread function (PSF) as illustrated in Figure 3.7b and c for an input objective of $50X$ and $10X$ respectively. The experimental intensity maps are reported in Figures 3.7d-g. The beam with wavelength of $\lambda = 400\,nm$ and $\lambda = 780\,nm$ passing through the MIMI presents a reduction of the initial full width at half maximum (FWHM) of $1\mu m$ and about $0.9\mu m$, respectively, which corresponds to a reduction of 36% when collected with a $50\times$ input objective. In case of a $10\times$ input objective, the beam reduction that occurs is about 20% as detailed in the field maps and PSF reported in Figure 3.7h-m.

3.3 Results of the hyper resolute TP-DLW lithography

In this section, I am going to show in detail how a standard TP-DLW process can be enhanced to hyper resolution by the presence of a MIMI nano-cavity. In particular, several attempts of fabrication with diverse dimensional features have been performed. A significant example in this direction is the realization of an array of 1D gratings, pitch $400\,nm$ on top of the MIMI previously deposited on a glass coverslip substrate. In case of a bare glass substrate, the focusing interface selected to start the laser writing process is established between the resin and the glass; in presence of the MIMI, instead, the interface is selected between the first silver layer and the glass. The use of an array permits to characterize each elements as a function of the laser power (LP), which varies from $12mW$ to $\sim 25mW$, and the scan speed (SS) which

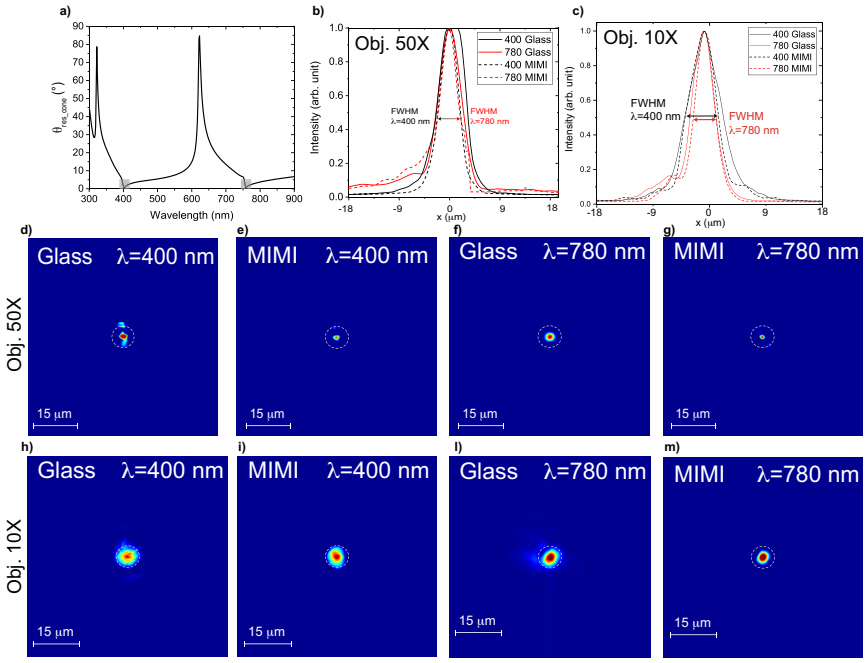

FIGURE 3.7: a) Calculated resonant cone angle of the fabricated MIMI. b-c)The experimental PSF reveals a beam shrinking of about 36% and 20% in the MIMI nano-cavity with respect the bare glass for the two input objectives. Experimental transmitted spot through the bare glass and MIMI nano-cavity at $\lambda = 400\,nm$ and at $\lambda = 780\,nm$, acquired through the beam profiler, d-g) for the four considered cases with the $50x$, and h-m) with the $10x$ input objective. Figure readapted from reference [202, 203].

varies from $2mm/s$ to $10mm/s$. The topography analysis conducted using a confocal microscope Zeiss LSM 780 equipped with an AFM head-stage. The AFM measurements are performed with high resolute tips with precision of $\pm 2\,nm$. Each scan has been collected at high resolution of 1024x1024 px in order to reduce any background noise and it ensures to collect very high quality data. A comparison between the AFM measurements performed on the structures realized through a simple glass coverslip and through the MIMI nano-cavity is shown in the Figure 3.8. The difference between the standard TP-DLW process and the MIMI configuration stands out immediately offering the possibility to clearly trace straight lines without defects (Figures 3.8a and b). A comparison between two fabricated gratings, using $LP = 20mW$ and $SS = 4mm/s$, has been done based on the raw images of the AFM profile. As illustrated in Figure 3.8c, a remarkable difference in terms of height and width of each grating element is present, with height values passing from $H \sim 420\,nm$ to average $\tilde{H} \sim 30\,nm$ for the grating obtained through the bare glass or with the MIMI configuration, respectively. The latter shows, also, a half width of only $\tilde{H} \sim 30\,nm$. In Figure 3.8d, it is reported an AFM image of a grating realized using the lowest laser power and the fastest scan speed producing an $\tilde{H} \sim 7\,nm$ and a width $\tilde{W} \sim 150\,nm$.

In order to complete and better understand the comparison on both substrates, the size of each grating element contained in the test array has been

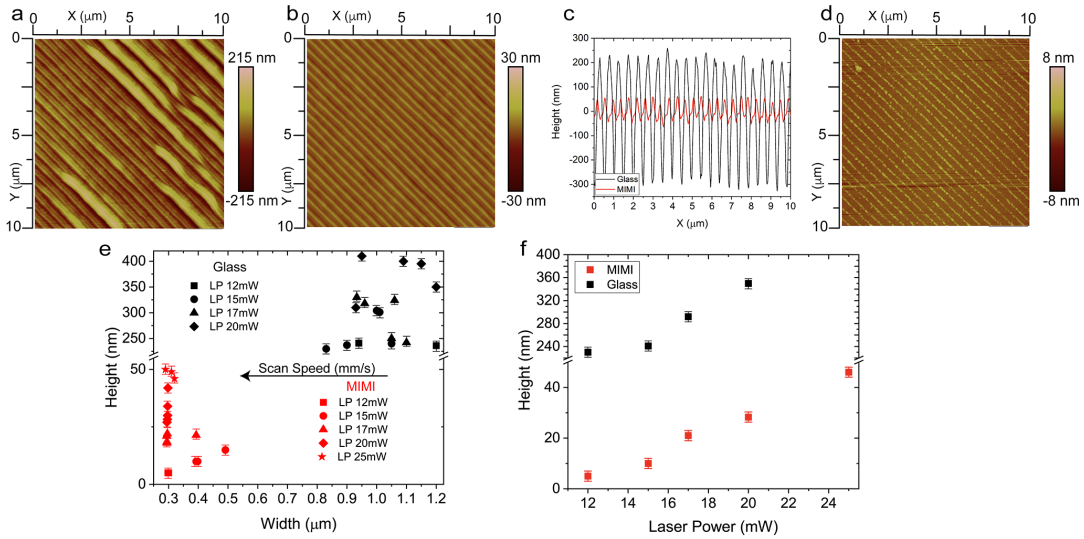

FIGURE 3.8: AFM morphology of a fabricated grating, pitch 400 nm with a Laser Power (LP) of 20 mW and a Scan Speed (SS) of 4 mm/s a) through the classical glass substrate and b) through the MIMI nano-cavity. c) Profiles comparison of the two fabricated grating. d) Grating realized through the MIMI nano-cavity using a LP of 12 mW and a SS of $4mm/s$ producing an element height of $\sim 5 \pm 2\, nm$. e) Height and Width for all the fabricated gratings at different laser power and scan speed using the glass substrate (black symbols) and the MIMI (red symbols). f) Height as function of the LP for glass (black square) and MIMI (red squares) substrates showing an average reduction of $\sim$ 89%. Figure readapted from reference [202, 203].

collected and reported in the graph shown in Figure 3.8e. The latter evidences an interesting and remarkable difference between the grating sizes produced by the two configurations. In fact, an improved resolution of $\sim$ 89% and $\sim$ 50% in terms of height and width is obtained, respectively. A further validation has been done by comparing the produced element height at different laser powers. The trend is similar for both substrates maintaining equal the difference that occurs between them as presented in Figure 3.8f.
The proof of concept of the reliability of the proposed technique, able to force the beam self-collimation during writing process, is the fabrication of particularly complex three-dimensional TP-DLW objects. The MIMI functionality has been challenged in producing a polymer bas-relief version of the famous Da Vinci's portrait *"Lady with an Ermine"* (Figure 3.9a). The choice to realize a bas-relief has been done considering that the process involves a 3D lithography and this portrait also contains very tiny details only reproducible in presence of hyper resolution. The first step is to create a computer-aided design (CAD) of the portrait image to be used in the TP-DLW process. The obtained design is shown in Figure 3.9b. The full height of the portrait is chosen as $H_z = 500\, nm$ that is divided in 25 slices of 20 nm thickness each. The optical microscopy image, collected by using unpolarized white light and a $40X$ objective, clearly underlines the contours of the portrait and evidences details like face, dress, hand, ermine and necklace (Figure 3.9c). This high quality optical image is also the consequence of the self-collimation of

the microscope impinging light, passing through the sample and reaching the objective, that experiments the lens effect of the ϵ_{NZ} metamaterial, as demonstrated in previous works[34, 215–218]. AFM morphology characterization has been done showing the bas-relief height $H \sim 500\,nm$ and the very impressive quality of this enhanced TP-DLW fabrication, as reported in Figure 3.9d. Since the resist used in the writing process is fluorescent, the col-

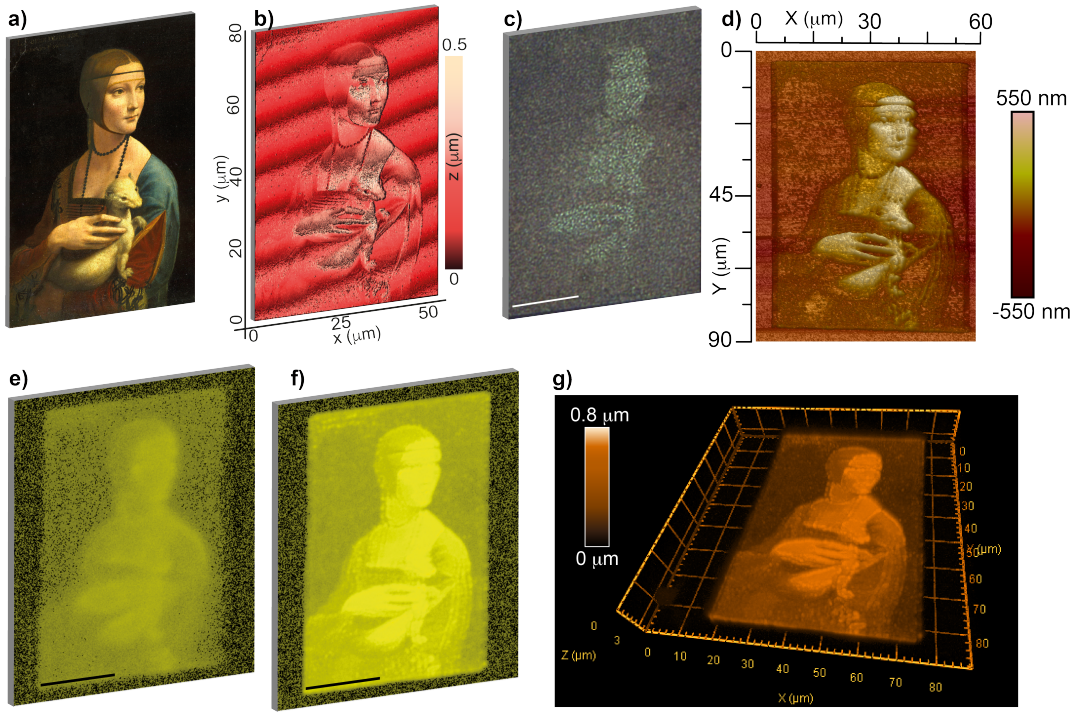

FIGURE 3.9: a) Original portrait and b) TP-DLW software model of the bas-relief *"Lady with an Ermine"*. c) Optical image of the realized 3D sample collected with an objective with magnification 40X through the MIMI substrate and enlighten from the top. d) AFM morphology of the fabricated sample. e-f) Emission confocal images of the bas-relief. In particular e) reports the base of the 3D print showing the silhouette of the "Lady". f) Image collected close to the top ($H_z \sim 0.5\mu m$) of the portrait and some details are shown as the hand, the shoulders, and parts of dress and face. g) A whole 3D sample image has been reconstructed highlighting the reliability to "print" very well all particulars at the nanoscale. The scale-bar in each picture is 20 μm.

lection of the whole bas-relief (Figure 3.9e-f) is also obtained by means of a fluorescence confocal microscopy analysis performed with a slicing of 10 nm along the z-axis. The fluorescence confocal 3D image has been acquired using a confocal microscope (Zeiss LSM790) equipped with a 3D piezoelectric scanner. A 488 nm laser was focused on the cover-slip through a 40$\times$ air objective, which allows a spatial resolution of 200 nm, and a z-resolution of 10 nm. The emitted light collected by the objective is sent to a beam-splitter and adequately filtered. Finally it passes through a pin-hole and is collected by a tunable detector that in this case is set in the range 550-600 nm. This imaging method allows to easily recognize at the minimum height the silhouette of the "Lady" (Figure 3.9e). Then by increasing the $H_z \sim 0.5\mu m$, the

frame shows the details present on top of the sample, as illustrated in Figure 3.9f. Finally, once the z-stack is completed, by using the proprietary software is possible to recombine all acquired images producing their full overlap and the final picture reported in Figure 3.9g. The preliminary test highlights the reliability of the hyper resolute 3D TP-DLW with slice distance of 20 nm and a high level of details reproduced in a very small volume. This technique is foreseen as a valuable possibility to realize anti-counterfeiting tags in the recent research framework of physical unclonable functions.

3.4 Conclusion

In this chapter, it has been reported a novel technique to enhance the writing resolution of a standard TP-DLW process by implementing an ad-hoc designed ENZ metamaterial. The application framework of this finding is expected to be very wide. Among the various possibilities, this approach is exploitable for 2D lithography at high resolution in the fabrication process for electronics, nano-fluidics, and optic devices. The MIMI structure reveals interesting features as the possibility to tune during the fabrication its optical response and shift transmittance peaks or reflectance dips. The diffraction-free ability of the ε_{NZ} metamaterial enables an extraordinary collimation of the writing laser light and hence the hyper resolution of the TP-DLW. In fabricating test structures like 1D gratings, a reduction of the voxel size of about 89% and 50%, for height and slit width respectively, is observed corresponding for the height of the grating to a reduction from $250 \pm 2\,nm$ to $5 \pm 2\,nm$. The proposed technique gives its best when more complex 3D structures are considered. a hyper-resolute bas-relief version of the famous Da Vinci's portrait *"Lady with an Ermine"* with a full height of only 500 nm divided in 25 slices of 20 nm thickness each. These new frontier results find immediate application in the trendsetting scenario of physical unclonable functions and flat-optics. These results pave the way for the next step represented by a far reaching application of the hyper resolute TP-DLW to fabricate all-dielectric metalenses with very interesting features as achromaticity, the broad working spectrum and the very high level of miniaturization.

Chapter 4

All-Dielectric Apochromatic Broadband Metalenses: Design, TP-DLW fabrication and Characterization

The purpose of this chapter is to show how the developed novel technique for hyper resolution of the TP-DLW process can be efficiently exploited for the fabrication of all dielectric ultra-flat metalenses. Because of their nanometric sizes, these metalenses present very fascinating and intriguing features as achromaticity and broad spectral working range. In order to understand the strong potential of this new optical element a brief state of the art is presented. In fact, Metalenses offer the ground-breaking opportunity to realize highly performing low-weight, flat and ultra-thin, optical elements which substantially reduce size and complexity of imaging systems. Today, a major challenge in metalenses design is still the realization of achromatic optical elements ideally able to focus a broad wavelength spectrum at a single focal length. In order to feature out the design and to optimally solve achromaticity issues, I present a numerical system that exploits the inverse design mediated by deep machine learning and a FEM (COMSOL Multiphysics) analysis based on the near field analysis and the beam envelop method. After that, I improved the photo-polymerization process, as described in Chapter 3, in order to realize these metalenses with the most possible accuracy and resolution. This aspect is highly relevant considering that a two-photon process is able to pattern a single metalens within a time shorter than a minute. Several characterizations have been exploited, by the use of optical microscope, atomic force microscope and a homebuilt confocal microscope able to evaluate the beam profile, the focal length and the depth of focus (DOF) when the metalenses are impinged from a single laser, a multiple lasers and white light. These characterizations on the fabricated metalenses, based on a completely flat and ultra-thin design, show intriguing optical features. Overall, achromatic behavior, focal length of $1.14\,mm$, a numerical aperture $NA = 0.087$, depth of focus of hundreds of microns ($|50 : 150|\,\mu m$) and total thickness of only few nanometers ($\sim 30\,nm$) allow considering the design of novel and efficient imaging systems in a completely new perspective. In fact, this results has great significance for the practical and industrial application of flat and fully planar metalenses.

4.1 Metalenses: the state of art

In recent years, the development of optical elements at the nanoscale raises a huge and wide interest in material science for the many physical and chemical aspects involved in the fabrication and the return in applied fields because of the relevant optical properties that obviously contribute to the research on perfect flat lenses (a sketch is shown in Figure 4.1) and phase change systems[219–221], or interferometric effects exploitable for sensing [222]. In this section we highlight the main aspects of metalenses, considered as a special case of metasurfaces, evidencing limits and benefits[223]. Until now, the most significant contribution in this research field was given by *F. Capasso and his research group*. They exploited different possibilities until achieving achromatic broadband metalenses with flat design patterned on large area [224–227]. The background research on metalenses and their development is long and complex with a sensitive leap made in the last decade. Some studies started from linear metasurfaces able to work in the IR spectrum. Then, discreet patterns have been involved to mime classical lenses, going to reconstruct the phase shift normally given by the surface curvature [228–230]. The replacement of bulk refractive optical elements with diffractive planar components enables the miniaturization of optical systems. However, diffractive optics suffer of chromatic aberrations due to the dispersion of the phase accumulated by light during propagation, some examples are presented in Figure 4.1b-c. In this case, it has been shown that this limitation can be overcome with a simple engineering wavelength-dependent phase shift imparted on the metasurfaces distribution, and a device designed in that way should deflect three wavelengths by the same angle. These options imply to consider the focal length (f) and the beam deflection calculated under a new point of view. In fact, it is necessary to consider the number of discreet elements (N), the size of those (Λ) ones involved in the structure and the total area occupied by the metalens(R_N^2) [231]. Similar metalenses, realized by Capasso et al., were initially constituted by metal sub-elements replaced later on by dielectric ones: an example is given by an array of SiO_2 nanoscopic conical bulges with base diameter of few hundreds of nanometers and height of around 2 μm[232]. But as reported in literature this system is fabricated by electron beam lithography (EBL) or Deep UV lithography (DUV) and its immediately to know that to pattern large area with this method its extremely time-consuming to manufacture with high resolution, as the samples produced in Figure 4.1c. Obviously, the number of researchers that begin to study and improve this kind of metalenses and metasurfaces for several applications are very huge. They are investigating the possibility to improve metalens using it as diffractive elements [233–235], the use of vary focal systems to obtain multiple focal length to correct the achromaticity[236, 237] for imaging [238, 239], the use of multiple small metalenses [240], and until the quantum electrodynamics [241]. We do not have to forget that some examples of flat lenses coming from the past, in 1748 *George-Louis Leclerc* developed the original idea dividing a lens surface into concentric rings in order to

reduce the weight significantly. In 1821 this idea was adopted by Augustin-Jean Fresnel in the construction of lighthouse lenses. After that, some examples have been proposed from them reaching the well known Fresnel Zone Plates (FZP) lens, a sketch is represented in Figure 4.1a-center. According with FZP lens I proposed a new simplest design of these in order to develop a flat metalenses completely made by polymer and to produce them in a very short time. About this last progress I, and my research group, deposited a whole ultra-flat but very performing metalenses preprint [203, 242].

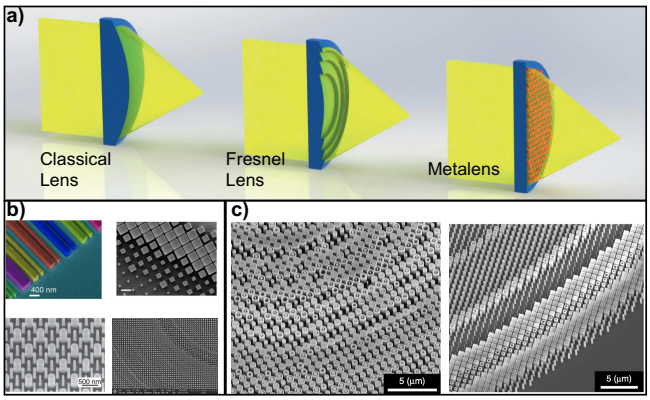

FIGURE 4.1: The Figure depicts the state of art, a) shows the evolution of optics element from a classical lens to metalaneses passing through the Fresnel ones (Sketch readapted from reference [223]). b) is an examples of different realized metasurfaces and metalenses as already presented by [226]. c) depicts two complicate examples of all dielectric metalenses realized by EBL, (taken from [235]).

4.2 Metalenses design assisted by Deep Machine Learning

The metalenses proposed in this doctoral thesis reproduce the optical behavior of a classic lens by means of low-loss dielectric metasurfaces. However, their functionalities go beyond those of classical lenses by introducing a variety of optical modes enabling dispersive phase compensation and chromatic aberrations suppression [232]. In order to efficiently design the metalenses, their geometrical parameters are retrieved through an inverse design method mediated by deep machine learning (DML). The latter exploits the "GLOnets" [243] and generative adversarial networks (GANs) to realize the target refractive index pattern. In detail, the algorithm iteratively modifies geometrical features of polymeric nanoridges, like height H, width W, period Λ and maximum transverse dimension u (Figure 4.2a), until the metalens acquires the desired optical function. The range of sizes, within which these parameters can vary, are derived from the study reporting the hyper resolved TP-DLW technique [202]. In particular, height and width for each element vary by few tens and few hundreds of nanometers respectively, more details are reported in the following lines. These parameters such as

the geometrical ones, the wavelength, the focal length, and the deflection angle represent the main inputs of the neural network used in the GLOnets (Metanet code). Here, we designed and optimized an ensemble of polymer nano ridges that operates across a wide range of wavelengths in the UV-NIR range. This code builds on analysis of conditional GAN that can optimize only a single device in a training session. This means that focal length and wavelength are fixed, while the other parameters are continuously changed from the input array values. The thickness of the nano ridges is varied in the range from $H \sim (5 : 40 \pm 2)\, nm$ and the incident light is TM/TE-polarized. For each device, the nanoridge pattern period (Λ) is divided into segments $N = \Lambda/W$ where $W \sim (200 : 500 \pm 2)\, nm$ represents the nanoridge width. For each segment, the refractive index of polymer or air is considered. The nanoridge pattern deflects normally incident light to a direction meeting the focal point (Figure 4.2 a). The optimization scope is to maximize the deflection efficiency of the metalens given an operating wavelength ranging from 400 to 1000 nm and an outgoing angle ranging from 40° to 80°. A schematic representation of our conditional GAN flow chart is presented in Figure 4.2b. The input are the operating wavelength λ, the geometrical parameters H, W and Λ, the desired focal length (f), the maximum transversal dimension (u) and the near field equation. In fact, At each iteration, the developed GAN algorithm modifies the geometrical parameters to let the nanoridges design converge to desired focal length $f = (1 : 1.2\, mm)$ and $u = (0 : 100\, \mu m)$. At this point of the design, the spatial distribution of the nanoridges is 1D. The metalens with cylindrical symmetry is obtained by revolving the nanoridge pattern around its propagation axis, see Figure 4.2c. The GAN uses the actual geometrical parameters and the considered wavelength to calculate the produced electric near field $E(x_0, y)$ and compare it with the one that would be produced by an equivalent (same focus distance) classic lens. For each considered wavelength, namely 405 nm, 532 nm, 633 nm, 780nm and 1000 nm, the calculated geometrical parameters that satisfy the comparison within a certain error are stored, as well as some examples of the developed element arrangement are reported in Figure 4.2d. There, the black/white strip-image represents the output design that is the refractive index profile $n(u)$ of the device. By exploiting the following *Fresnel diffraction formula*, the calculated near field $E(x_0, y)$ can be used to obtain the far field envelope $E(f, u)$ of the wave propagating from the metalens.

$$E(u, f) = \frac{1}{\sqrt{\lambda}} \int_{-\infty}^{\infty} E(x, y_0) e^{-i\pi y^2/(\lambda f)} e^{-i\pi u y/(\lambda f)} dy \tag{4.1}$$

where $u/(\lambda f)$ is the spatial frequency, $E(x, y_0)$ and $E(u, f)$ are the electric field amplitude distributions at the exit plane $x = x_0$ and the focal plane $x = f$, respectively. From the above analysis, the metalens structure has the following retrieved parameters: total radius $u = 100\, \mu m$, period $\Lambda = 1\, \mu m$, height and width of the nanoridge element $H = 30$ and $W = 200$ respectively. In order to avoid hole diffraction, the inner center of the metalens is filled with lines. The algorithm has to satisfy a high efficiency value for each

considered wavelength and for different deflection angles θ. Figure 4.2d reports the most efficient evaluated element disposition patterns for some cases $\lambda = 405\,nm$, $\lambda = 532\,nm$, $\lambda = 633\,nm$, $\lambda = 1000\,nm$. For a bunch of iterations, the code returns a histogram with the efficiency reached for each disposition, as reported in Figure 4.2e. Finally, all the best data is stored and matched to obtain the element sizes that satisfy the initial condition as already discussed above. The enormous advantage of design algorithms coupled with the TP-DLW cad software is represented by the direct conversion of the produced design sketch into the instruction file for the TP-DLW writing for a quick and efficient metalens fabrication. By using the previous formula with the re-

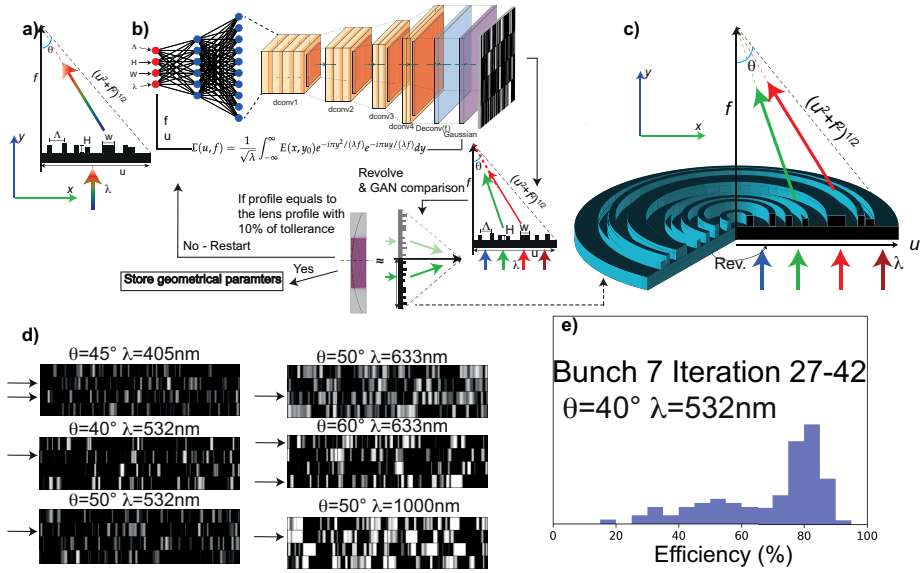

FIGURE 4.2: Global optimization based on a generative neural network (GAN) opportunely modified. a) Schematic view of nano ridges that constitutes the metalens. b) Schematic representation of the conditional GANs code for metalens generation. The generator is built by a neural network, deconvolution layers (dconv) and a Gaussian filter. An identity shortcut connection is also used by the electric near field equation. The input of GANs code are the device's geometrical parameters as height (H), width (W), period (Λ) and finally wavelength (λ). During each iteration of training, a batch of devices is generated and for each device efficiency gradients (g) are calculated using forward electromagnetic simulations. These gradients are propagated through the network to update the weights of neurons (W_n). The GAN verifies that the near field E(x; y0) produced by the metasurface satisfy the Fresnel diffraction formula (E(u; f)). Then, the GAN algorithm compares the electrical near field of the actual geometrical parameters and the considered wavelength with the one of a classical lens having the same focal length. Only the parameters that respect the fixed condition over the focal length and the maximum lens transversal dimension at multiple wavelengths are stored. c) Revolved sketch of the constitutive elements. d) Examples of produced element disposition in function of wavelength and deflection angle, varying the height, width and period of the constitutive metalens element. e) Histogram efficiency used to chose the element disposition. Figure readapted from reference [203, 242].

trieved geometrical parameters, the beam profile along the propagation XZ plane is evaluated at the resulting common focal length of 1.14 mm for each considered wavelength; obtained results are reported in Figure 4.3a. Figure 4.3b reports a further analysis conducted calculating the electric far field maps for each considered wavelength by means of a beam envelope model based on Rigorous Coupled Wave Analysis (RCWA). Each beam envelope is calculated along the propagation plane XZ together with its corresponding focal spot image ($z = f = 1.14\,mm$) in the transverse XY plane. The performance of a generic imaging system can be quantified as well by calculating its point spread function (PSF). The PSF amplitude of a lens can be defined as the transverse spatial light intensity variation of the image received at the focal plane (FP) when the lens is illuminated by a perfect plane source [244] (Figure 4.3c). It is worth noting that the results obtained using the different methods is quite impressive: each wavelength profile converges to the focal plane with a Full Width Half Maximum (FWHM) lower than the diameter of the whole metalens. The PSF, calculated in the XY focal plane, shows a sharp FWHM presenting values close to $\sim 1\,\mu m$ for all considered wavelengths (Figure 4.3c). Thereafter, the depth of focus (DOF), or the distance from the focal point to the position where the intensity profile drops to half its maximum, is evaluated from the electric far field maps. This results close to 50 μm for shorter wavelength and more than 200 μm for longer ones, as indicated by dashed green lines drawn on Figure 4.3b. A representative sketch of the metalens able to work at different wavelengths is reported in Figure 4.3d. According with the performed numerical simulation and past studies, the designed metalenses present also a zero phase shift at the focal length [226, 245]. This feature covers a fundamental role in the broadband achromatic lens projection. In fact, in order to ensure the zero phase shift of the proposed metalenses for each considered wavelength, numerical simulations and the corresponding analysis have been done as reported in Figure 4.4a-e. It is close to $0rad$ for all wavelengths at the focal length of $f = 1.14\,mm$; similar results have been already presented for different achromatic metasurfaces[226, 245]. The phase is calculated as the argument of the electric field component along the propagation axis ($arg(\mathbf{E}_y)$. The maximum transverse dimension of the nanoridges pattern "u", equal to 100 μm, is the center of the metalens and the phase has been evaluated using a cut line at the calculate focal distance common for all wavelengths. The phase shift, according with past studies, results equal to $\phi(x) \sim 2\pi n_{eff}(x)t/\lambda$, where x represents the dimension along the lens diameter with a maximum extension equal to $x = 2 * u$. When this equation is imposed equal to zero for each wavelength, the broadband achromatic lens design process starts [231, 246, 247]. In order to clarify the connection between the already studied metalens systems and our GAN implementation, it is necessary to consider the phase equation written as a function of the radial coordinate r resulting equal to $\phi(x) = -2\pi/\lambda_d(\sqrt{(r^2 - f^2)} - f)$, with $r = \sqrt{(u^2)}$. Fixing f and the maximum lens radius $r = u = (0 : 100)\,\mu m$, it is possible to run the GAN code until all conditions are respected, obtaining the element sizes (H,W, Λ) as already explained above. A comprehensive overview about the phase calculation and metalens design with different numerical tools are reported in ref [247].

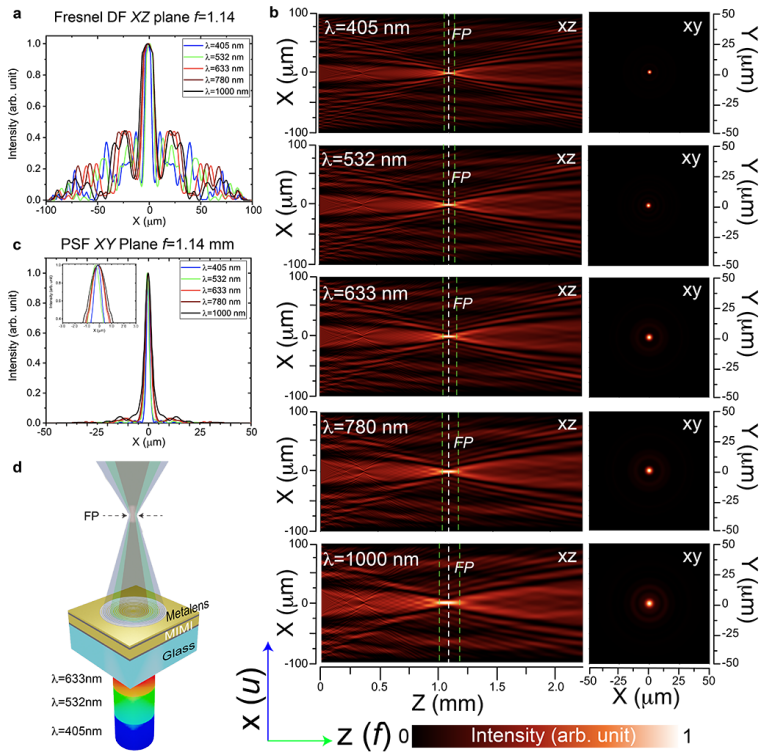

FIGURE 4.3: a) Beam envelope at the focal plane (common for five different wavelengths) calculated through the Fresnel diffraction formula by using the near field $E(x, y_0)$ distribution provided by the GAN algorithm. b) Electric field maps evaluated by using the beam envelope model based on Rigorous Coupled Wave Analysis (RCWA) for five different wavelengths along the propagation XZ plane together with its corresponding focal spot image (XY plane). c) Beam profile retrieved at the common XY focal plane (FP, $f = 1.14\,mm$) by calculating the Point Spread Function (PSF); d) Schematic view of numerically designed apochromatic metalens. Figure readapted from reference [203, 242].

Metalenses fabrication by TP-DLW

Once designed, the metalenses are fabricated exploiting the enhanced two-photon direct laser writing (TP-DLW) technique which adopts a metal-insulator-metal-insulator (MIMI) nano-cavity for the hyper resolution performance (sketch in Figure 4.3d). In the last years, the TP-DLW technique has emerged as a new frontier for micro- and nano-fabrication, often replacing electron beam and UV lithography. It is actually used to realize miniaturized efficient bulk optics [248]. However, the present technology performance needs to be pushed to its limits to achieve the required patterning of all dielectric metasurfaces like ultra-thin diffractive optical elements [219, 249] or complex circular structures made by single pillars [250]. The results reported in chapter 3 demonstrate that a substantial improvement of the TP-DLW capabilities is obtained when the process is upgraded through the exploitation of a MIMI nano-cavity. The introduction of the MIMI metamaterial in the TP-DLW process represents a ground-breaking technological leap: typical sizes of few tens and few hundreds of nanometers in height and slit width[202],

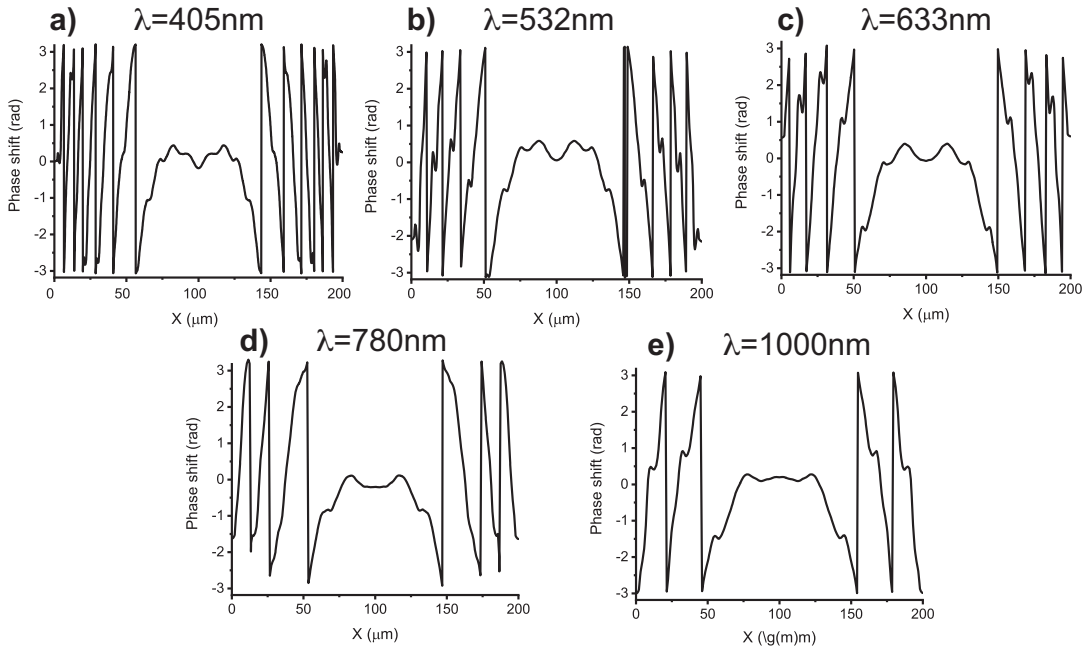

FIGURE 4.4: The phase shift analyzed for different wavelengths at the same focal length and along the lens diameter. The analyzed wavelengths are: a) 450 nm, b) 532 nm, c) 633 nm, d) 780 nm and finally e) 1000 nm.

respectively, are easily achievable and the fabrication of all dielectric ultra-thin nano-structures, as flat metalenses, is obtained in a fraction of the time required by other standard processes. The array of (5X4) metalenses considered in this work has been fabricated in less than five minutes thus confirming the fast fabrication procedure as extremely useful for mass production and application in end-user imaging devices[240]. The nano-cavity has been deposited by DC sputtering on glass substrate with thickness of $\sim$ 100 μm) and it is constituted starting from the glass as follow: 30 nm Ag layer, 160 nm ZnO cavity, 30 nm Ag layer and 30 nm ZnO layer. The system is placed in front of the two-photon source. This lithography apparatus is used to define the metasurface lens pattern in a drop of photo-sensitive resist placed on top of the nano-cavity. The laser power used for the process is equal to 20mW and the scan speed is 4000 μm. After the writing process, the whole system (nano-cavity with cured and uncured photo-resin) is soaked in a bath of propylene glycol methyl ether acetate (PGMEA) for 15 minutes and then cleaned in a bath of isopropanol alcohol (IPA) for other 5 minutes.

4.3 Morphological and microscopic characterization

After writing and development steps, a morphological characterization on the fabricated metalenses has been performed using an Atomic Force Microscope (AFM), the acquired image are reported in Figure 4.5a. By showing a width $W \sim 200\,nm$ and a height of only $H \sim 30\,nm$, the AFM profile

of each circle (Figure 4.5b) confirms the ultra-thin characteristics of the proposed metalens. Finally, Figure 4.5c-f report an optical microscopy analysis conducted on the matrix of metalenses, evidencing their details. Image in Figure 4.5c has been acquired with a magnification of 20x while, the inset shows the zoom (50x) of a single structure. Successively, according with the peculiar feature of the nano-cavity [139], a single metalens has been observed using a band pass filter (BPF) centered at three different wavelengths, two close to the double ε_{NZ} resonances and one far from them. The first test has been performed by using a filter centered at $\lambda_{BPF} = 390\,nm$, see Figure 4.5d. In this condition, the structure is very clear and it is also possible to distinguish horizontal lines in the inner circle of the metalens (Figure 4.5d). These lines fill the inner center of the metalens to avoid hole diffraction. The same test has been repeated with a BPF centered at $\lambda_{BPF} = 450\,nm$, now the structure appears blur and the circles broad (Figure 4.5e). Finally, the image reported in Figure 4.5f has been collected by using a BPF centered at $\lambda_{BPF} \sim 780\,nm$. As expected, the system appears again very clear and the features of each structure are highly defined. The high resolution at blue and infrared wavelengths is an effect related to the double resonances of the MIMI nano-cavity and a direct consequence of the zero light spreading of its the ε_{NZ} property [202]. Further details about the unusual optical behaviour of ε_{NZ} metamaterials can be found in past studies[74, 75, 215–217].

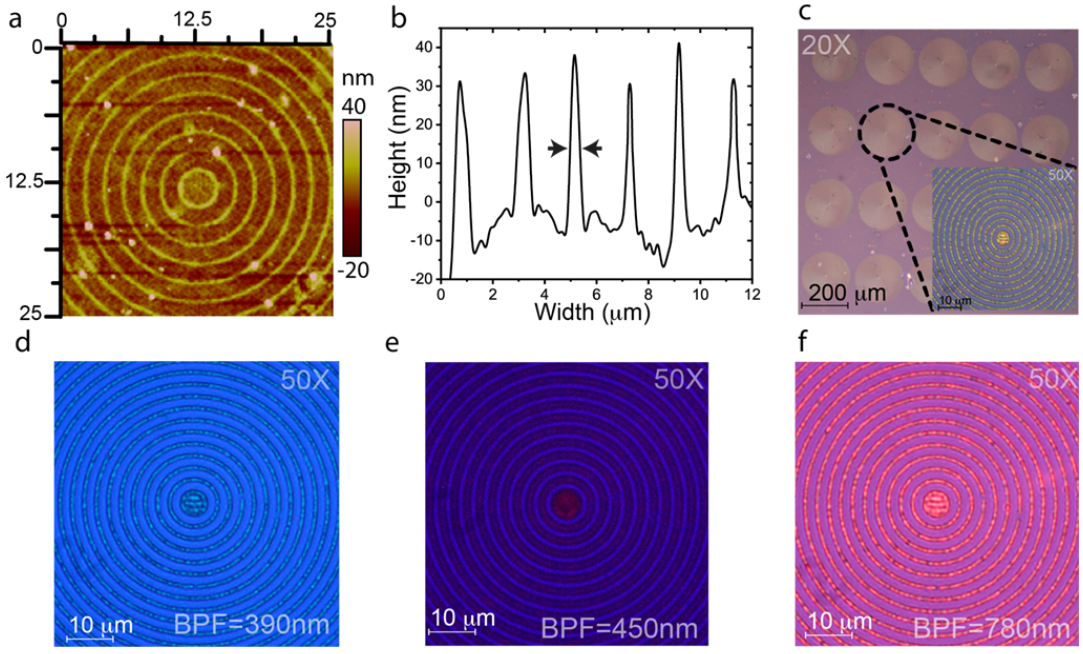

FIGURE 4.5: a) AFM morphological characterization of the metalenses with b) the related height and width profile obtained from a transversal cut. c) Optical image of the metalenses matrix acquired with microscope with magnification 20x, (zoom at 50x in the inset). Particular of one metalens at 50x observed using band pass filter (BPF) at d) 390 nm, e) 450 nm and f) 780 nm. Figure readapted from reference [203, 242].

4.4 Experimental Results: All-dielectric metalenses optical carachterization

A complete optical characterization of the fabricated metalenses, exploiting the confocal home-built setup shown in Figure 4.6a, has been performed. The use of a beam profiler (BP) permits to collect, at the same time, the intensity of the signal, the beam profile, high quality 2D pictures of the sample and a 3D reconstruction made by the intensity, as largely done in past studies [227, 245, 251]. The focal length, the beam divergence and the point spread function (PSF) analysis has been performed using continuous wave three lasers (3L), namely a blue one at $\lambda = 405\,nm$ (BL), a green one at $\lambda = 532\,nm$ (GL) and red one at $\lambda = 633\,nm$ (RL), and a white light source originating from a Xenon lamp (WL) with intensity of $50\mu W/mm^2$. First of all using the presented setup the metalens focal length has been estimated. The confocal homebuilt setup has been used allowing to remove the optical elements that are not necessary for the complete measurement 4.6b-c. The first step consists to place the sample containing the metalens in the optical path of the confocal configuration (Figure 4.6c). Then, once the focus is found on the metalens, the input objective (10X) is removed. Finally, the light impinges on the metalens and the output objective (32X) is moved along z until the new focal spot is established, Figure 4.6d. The distance between the first and the second configuration corresponds to the focal length, which in our case is close to $f = 1.14\,mm$. Figure 4.6e is a prospective view of the setup during the metalens focus measurement and its characterization. The optical response of the metalens at different propagation distances using each above laser at one-by-one wavelength is reported in Figure 4.7a, b and c respectively. Then, the three laser beams have been used simultaneusly to reproduce a RGB coherent source (RGBL) (Figure 4.7d). Then, the optical behavior of the metalens has been compared with the analysis conducted by the broadband white light source ($250\,nm$ to $1100\,nm$), as reported in Figure 4.7e. All the measurements validate the metalens broadband achromatic behavior with a focal length of $1.14\,mm$, as reported in our recent manuscript [203, 242]. In order to compare the numerical prediction and the experimental results, the full width half maximum (FWHM) at the focal plane (f) for each considered case has been evaluated and reported in Figure 4.7f. For each single laser wavelength (BL, GL and RL) the PSF presents a value of FWHM of only $0.9\,\mu m$, for 3L the FWHM is $1.5\,\mu m$ and for the WL it is $1.6\,\mu m$. The experimental depth of focus (DOF) of the metalens, which depends on the impinging wavelength, agrees with the numerical studies showing average values in the ranfe $100 - 150\,\mu m$ around the common focal distance for all wavelengths, see Figure 4.7g. Similar results have been demonstrated for grating-based metasurfaces [252]. The experimental DOF of the proposed metalens has been reported for each single light source and the combination of them, see Figure 4.7g. It is collected in the propagation range along z from $-200\,\mu m$ to $200\,\mu m$. As predicted by the numerical simulations, the DOF is short in the blu-green spectral range, while it starts to increase when the wavelength is close to the red-IR spectral

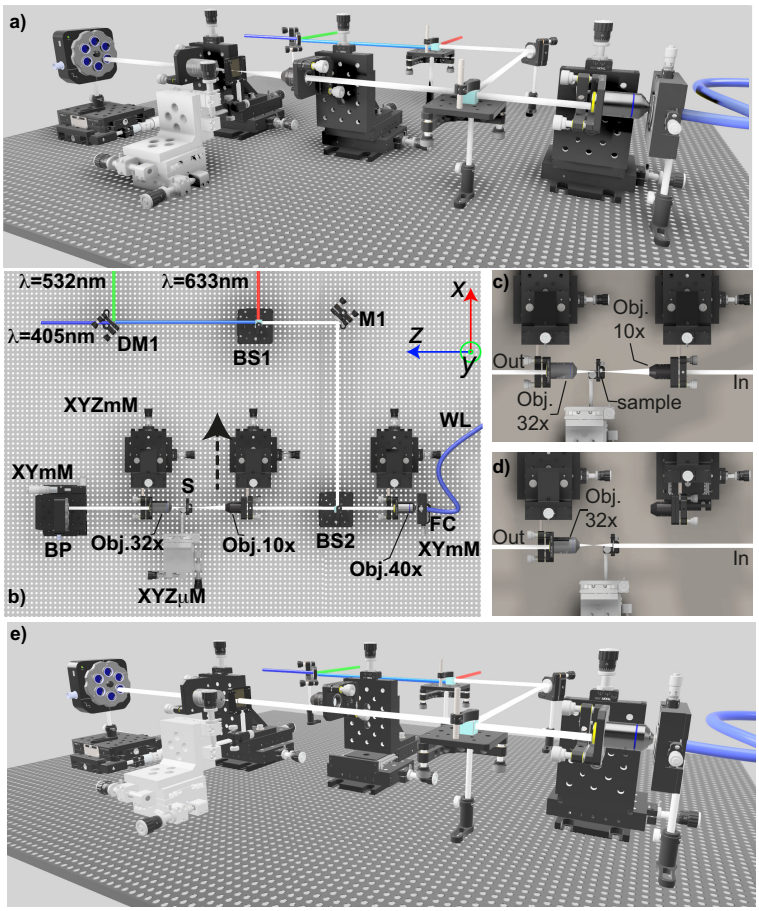

FIGURE 4.6: a) A perspective view of the optical setup used to characterize the metalens for the focal length. b) The top view with the detailed elements used in that setup. c) The sketch represents the initial confocal configuration, and d) the metalens focal length is evaluated removing the input objective (red arrow) and moving along z the output objective (32x) until the produced output spot is again the smallest one.

range. The combination of lasers (3L) presents a DOF extended as the red one. Instead, the withe light (WL) produces a depth of focus very short due to the incoherent nature of the propagated light and also because it is a continuous spectrum and the metalenses probably do not focus all wavelengths emitted by the Xenon lamp. Another important feature of this all-dielectric metalens is the the numerical aperture $NA \simeq nD/2f = 0.087$. The numerical aperture is evaluated using the following equation:

$$NA = nsin\theta \tag{4.2}$$

In the condition of a low lens magnification the equation (4.2) is reduced to

$$\mathrm{NA_i} = n\sin\theta = n\sin\left[\arctan\left(\frac{D}{2f}\right)\right] \approx n\frac{D}{2f} \tag{4.3}$$

Where D is the diameter of the lens $D = 2 * R_N$, n is the refractive index of the medium where the metalenses work $n \sim 1.0$ and f is the focal length. Such high NA value is extremely useful for realizing very precise lens systems for imaging and confocal instruments. Finally, in order to further confirm the achromatic behavior of the proposed metalens, a CIE chromaticity xy-coordinate graph has been evaluated for all the considered cases and reported in Figure 4.7h. The use of a $\lambda = 405\,nm$ produces a blue/purple point and the three collinear lasers (3L) results shifted in a blur white on the tristimulus region (warm light)[166]. As expected, the white lamp is centered on the pure white point (cold light). To further validate the RGB behavior, another test has been done using a laser with a different blue wavelength, $\lambda = 445\,nm$, obtaining this time a practically blue spot. Now, if this blue laser is combined with previous green (GL) and red (RL) lasers, a white spot comparable with the WL is obtained, reported in the gamut plot as the RGB grey circle. These results corroborate the broadband achromatic behavior of the proposed ultra-thin dielectric metalenses fabricated with a hyper resolute TP-DLW lithography process. The whole characterization confirms extremely exciting properties of the proposed metalens that can be exploited, due to their miniaturization, as optical components for micro-nano imaging, smart devices, in situ investigation as a local spectroscopic probe, color sensitivity and so on [220, 241, 251, 253–256].

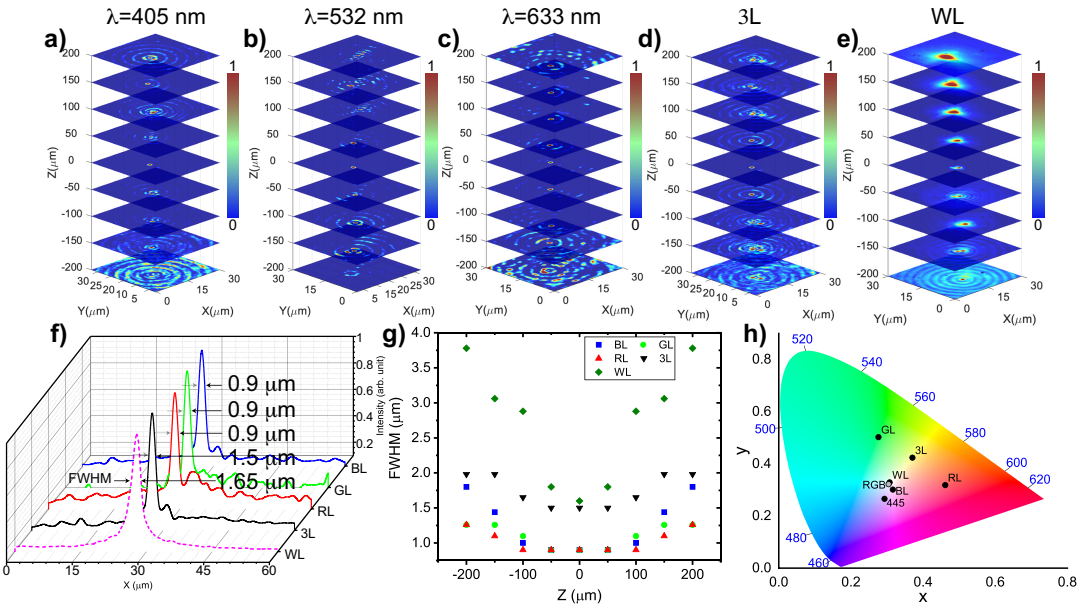

FIGURE 4.7: Stacks of the beam divergence from the focal length (1.14 mm) indicated as z=0 to $\pm 200\ \mu m$ at a) $\lambda = 405\ nm$ b)$\lambda = 532\ nm$ c)$\lambda = 633\ nm$ d) using the previous three lasers at the same time and e) using a Xenon lamp source. f) Full Width Half Maximum (FWHM) for all considered cases. It is 0.9 μm for each single laser (BL, GL, RL), 1.5 μm for the three lasers (3L) and 1.65 μm for the white lamp (WL). g) The DOF evaluated for each input laser, has been calculated considering the FWHM of the produced spot along the propagation direction z in the range from $-200\ \mu m$ to $200\ \mu m$. h) CIE chromaticity xy-coordinate plot for each laser wavelength, combination of them (3L) and white lamp (WL); for laser with $\lambda = 445\ nm$ and the combination with the GL and RL producing RGB spot (grey circle). Figure readapted from reference [203, 242].

4.5 Conclusion

In this Chapter, the ultra-flat metalenses with vertical sizes in the order of few tens of nanometers ($\sim 30\ nm$) have been reported. The metalenses are designed through GANs algorithms based on deep machine learning, they are fabricated by hyper-resolute TP-DLW process, and finally they are optically characterized. The metalenses are able to work in a broad visible range ($\lambda \sim 400 : 1000\ nm$) focusing light at a focal length of 1.14 mm, DOF of about $|50 : 150|\ \mu m$ and the numerical aperture of $NA = 0.087$. These metalenses present ground-breaking advantages as low-cost single step and time-saving fabrication, nanometric sizes, all dielectric composition. Moreover, they are engineered to be achromatic across the entire visible spectrum. The achieved results represent a significant advance in the state-of-the-art of research on metalenses, that are typically limited in their application by bandwidth and chromatic aberration. These achromatic ultra-thin flat metalenses can find vast implementation across industry and scientific research, such as in miniaturized optical devices, advanced microscopy, local imaging and nano-lithography.

Conclusions and perspectives

In this Doctoral Thesis, we carried out a research work aiming at the design, fabrication and characterization of novel metamaterials able to extremely improve the resolution of the two photon direct laser writing process. The method proposed to improve the resolution of the photopolymerization process could be convenient because it is low-cost and fast. Common denominator of all metamaterial devices is the initial optical nano-cavity configuration composed by metal/ insulator/ metal/ insulator or, as we already called, MIMI. These systems present some features as the tunable resonant wavelength as a function of the dielectric cavity thickness and it allows to design a system that works at the operation wavelength used in the TP-DLW setup. The procedure for the optimization of the design of the proposed devices has been performed by means of a home-built TMM code and implemented with a Finite Element Method (FEM) in COMSOL Multiphysics, a commercial software. Successively, the MIMI systems have been fabricated using standard DC-Sputtering. All the experimental measurements agree very well with the simulation results confirming the great quality of the work both in terms of simulation and fabrication/ characterization. The perfect match between the fabricated MIMI and our TP-DLW setup allowed us producing some tests in order to confirm the increase in terms of writing resolution, the realization of samples exploitable in labels based-on physical anti-counterfeiting that can open the way for unclonable devices, and the last but not the least, the fabrication of all-dielectric ultra-flat metalenses that show incredible features as achromaticity, a broad working spectral range, extended focal length and depth of focus, and a numerical aperture comparable with the already realized metalenses.

In particular, in Chapter1, the main aspects about metamaterials, isofrequency surface that describes the dispersion relations of hyperbolic metamaterials, and the behavior in light-matter interaction have been considered. Then, the stacked multi-layer materials and a particular family of those, the εpsilon *N*ear *Z*ero, have also been presented. These metamaterials lead to obtain particular effects as light self-collimation and canalization inside it. Finally, an overview on the plasmonic behavior in a simple metal/insulator interface that produces surface plasmon polaritons, bulk plasmon polaritons in multi-stacked metamaterials and the gap surface plasmon in Fabry-Pérot nanocavities have been explained in details.

In Chapter 2, simple and fast but robust numerical methods to design metamaterials and to predict their optical behavior have been presented. The first purpose is the ellipsometry and its advantages to measure layered and nanostructures retrieving the ellipsometer parameters Ψ and Δ, the reflectance and transmittance and also the complex refractive index $n - ik$. Then, the Transfer Matrix Method (TMM) has been detailed and it has been also used

to code a homebuilt Matlab tool to predict the optical behavior. On the same way, by using COMSOL Multiphysics a Numerical Ellipsometer Analysis (NEA) has been realized. NEA covers the role of a robust tool to predict the optical response of metamaterials with/without superstructures placed above of them. Some numerical simulations predicted by the NEA are experimentally validated by different cases increasing the system complexity. The plasmonic dispersion relations and the modal analysis have been considered for the dielectric cavities that support multi-spectral mode in the visible range. Finally, in the last section particular effects produced by MIMI cavities have been studied. The color hues, produced by the different cavity thickness, and the involved material and a fast and effective way to observe the plasmons propagating inside those structures is proposed throughout the pseudo dielectric function $< \tilde{\varepsilon} >$. These designed cavities present also particular effects as high dephasing known as Goos-Hänchen shift that it is exploitable for extremely accurate sensing.
In Chapter 3, the main concepts of one and two-photon lithography and the state of art about the TP-DLW have been introduced. Then, detailed aspects reported in the first Chapter and the use of the MIMI properties and its features gave back the possibility to design an embed device able to work at the two photon lithography process wavelength ($\lambda = 780nm$ in the presented case). Then, by the home-built confocal setup equipped with a beam profiler, the fabricated prototype has been tested. The system was investigated in terms of incident beam waist modification after the passage through it and is evaluated by the Point Spread Function (PSF) reduction. After this characterization, the MIMI device was used to produce 1D gratings in order to compare the fabricated on a classical glass substrate to the one produced on the new ENZ substrates. The reduction of 89% in height and 50% in width lead this research to reproduce the famous portrait *"The Lady with an Ermine"* by *L. Da Vinci* that exhibits an high resolution level in terms of details and the nanoscale slicing in the 3D lithography fabrication.
Finally, in the Chapter 4, the results obtained by the improved TP-DLW technique are exploited for the realization of all-dielectric ultra-flat metalenses with sizes of few tens nanometers and interesting features such as achromaticity and a broadband spectral working range. The future optics follow the trendsetting scenario of miniaturized devices with outstanding features as extended focal length and Depth of Focus (DOF), standard Numerical Aperture number (compared with the already existing metalenses), and fast and easy way to produce them. This Chapter presents the metalenses designed by deep machine learning, then the fabrication done exploiting the MIMI substrates to increase the resolution of the TP-DLW process. Once the metalenses are fabricated, their optical characterization has been done by using the home-built setup realized on purpose. The focal length has been evaluated resulting equal to $f = 1.14\,mm$, the effective DOF is in the range $|50 - 150|\,\mu$ depending on the wavelength and the numerical aperture results $NA = 0.087$.
To sum up, innovative MIMI configurations with improved performance

have been numerically and experimentally presented. These low-cost devices can pave the way for a new class of metamaterial components for achieving hyper resolution in TP-DLW process. They cover an extremely important role for industrial applications in several fields such as anti-counterfeiting and flat optics.
The perspectives about the topics addressed on this Thesis such as metamaterials, nano fabrication and metalenses can be summarized in two main future goals. The first one is the integration of the MIMI substrate directly on the objective lens used during the two photon direct laser writing. This further implementation can open the way to fabricate polymeric structures with nanometric size on the desired substrate and it allows also to experiment the Dip in Laser Lithography (DiLL) technology using the commercial resist IP-DIP, or using the IP-n162 made for freeform optics. This latter serves as immersion and photosensitive material at the same time by dipping the microscope objective into this liquid photoresist. Due to its refractive index matched to the focusing optics IP-Dip guarantees ideal focusing and hence highest resolution for DiLL. The other aspects that cover an important role is the realization/projection of a system that allows the tuning of the focal length exploiting a refractive index variation in the surrounding medium. If developed in sequence, these two perspectives could pave the way to fabricate miniaturized lens with a variable focus on different substrates such as transparent, flexible, and reflective ones, just to name a few.

Appendix A

The Effective Medium Theory

In this Appendix we treat the *Effective Medium Theory (EMT)*. The EMTis still able to capture some specific remarkable feature of the wave propagation inside these metastructures, among which the so-called Epsilon-Near-Zero-and-Pole condition finds place, which will be the main topic of this chapter. Therefore, it is essential to lay the fundaments of this theory. [17]

The constitutive relations remain valid independently on the polarization of the incident electric field and even for the effective medium so that they can be used for the calculation of both the parallel and perpendicular effective permittivity components:

$$D_j = \tilde{\varepsilon}_j E_j \tag{A.1}$$

where j stands for the considered material that can be the metal or the dielectric. It is important noticing that Eq. (A.1) is still valid even for the overall HMM, so that it can be assumed that $D_{eff} = \varepsilon_{eff} E_{eff}$, where ε_{eff} can be equal to $\varepsilon_{\parallel}$ or $\varepsilon_{\perp}$, accordingly to which parameter is being calculated.

Let?s now consider the case in which the electric field is polarized along the HMM?s surface plane. This procedure leads to the calculation of ?$\parallel$. In this case, the electric field has to be continuous at the interfaces between the metal and the dielectric. This means that:

$$E_m = E_d = E_{eff} \tag{A.2}$$

where the subscripts m, d and eff stands for metal, dielectric and effective, respectively. The superscript "$\tilde{\varepsilon}$" in Eq. (A.1) indicates that the dielectric permittivities are complex quantities. Indeed, the effective parameters are also valid for the imaginary components and are intrinsically Kramers-Krönig consistent.

The effective electric flux can be expressed as the sum of the flux density in the metal and the dielectric, averaged to each respective fill fraction f $j = (d_j/(d_{tot}))$, being d_j the thickness of the jth material ant d_{tot} the total thickness of a single metal/dielectric bilayer:

$$D_{eff,\parallel} = \tilde{\varepsilon}_{\parallel} E_{eff} = f_m d_m + f_d d_d \tag{A.3}$$

by replacing Eq. (A.2) in Eq. (A.3), we obtain the expression for $\tilde{\varepsilon}_{\parallel}$:

$$\tilde{\varepsilon}_{\parallel} = \frac{\tilde{\varepsilon}_m d_m + \tilde{\varepsilon}_d d_d}{d_m d_d} \tag{A.4}$$

In order to calculate $\tilde{\varepsilon}_{\perp}$ we start from the consideration that, when the electromagnetic field is polarized perpendicularly to the HMM?s surface plane, the electric flux d_j is continuous at the interfaces:

$$D_{eff,\perp} = \tilde{\varepsilon}_{\perp} E_{eff} = d_m + d_d \tag{A.5}$$

In this case, the effective electric field can be expressed as the fill-fraction averaged electric field in every single component, so that

$$E_{eff} = f_m E_m + f_d E_d \tag{A.6}$$

and, by replacing Eq. (A.5) in Eq. (A.6), the expression $\tilde{\varepsilon}_{\perp}$ can be immediately found:

$$\tilde{\varepsilon}_{\perp} = \frac{\tilde{\varepsilon}_d \tilde{\varepsilon}_m (d_m + d_d)}{\tilde{\varepsilon}_m d_d + \tilde{\varepsilon}_d d_m} \tag{A.7}$$

Equations (A.4) and (A.7) represent the two components of the effective local permittivities for a multilayered HMM and also an ϵNZ (and Pole) metamaterials.

Provided that the optical response can be modeled with sufficient precision via the local $\tilde{\varepsilon}_{\parallel}$ and $\tilde{\varepsilon}_{\perp}$, it is possible to calculate the exact dispersion relation for a multilayered HMM. Such a quantity provides information about the light propagation through the metamaterial and allows explaining a plethora of noticeable properties, from super-collimation to lifetime engineering in the proximity of HMMs.

Appendix B

The TMM code in Matlab

Here, it is reported the block diagram of the homebuilt script used for the *Transfer Matrix Method* coded in Matlab.

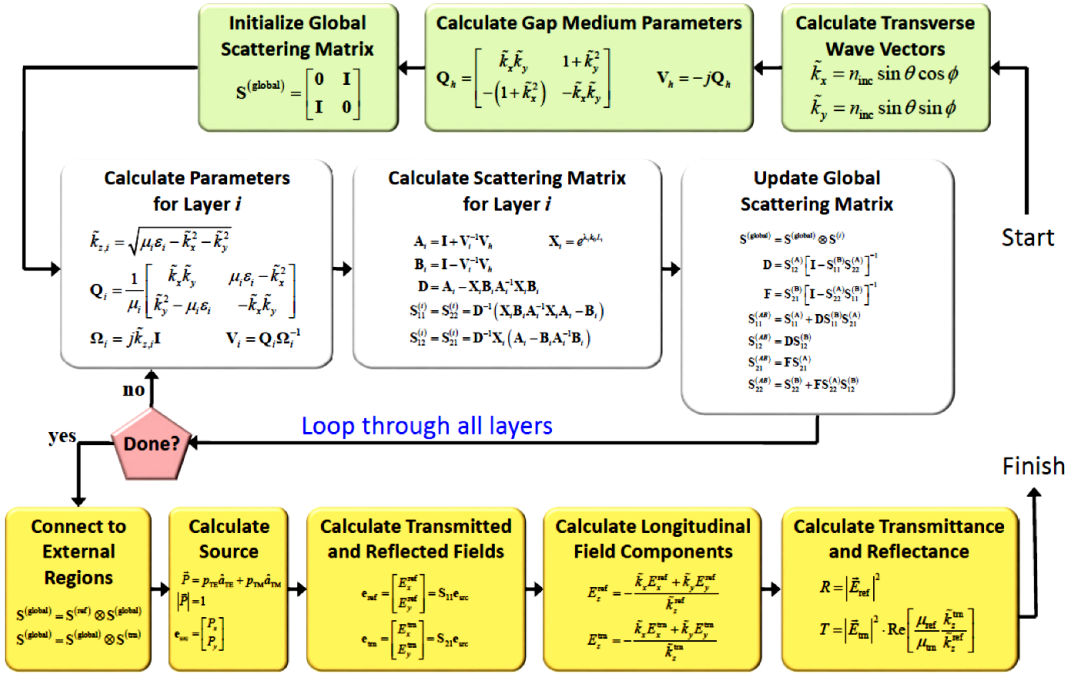

FIGURE B.1: The sketch represents the block diagram of the TMM coded in Matlab

List of Figures

1.1 Isofrequency surfaces the dispersion relation of hyperbolic metamaterials. a,b Isofrequency surfaces given by $\omega(k)$ = constant for $\varepsilon_{zz} = \varepsilon_{\perp} < 0$, $\varepsilon_{xx} = \varepsilon_{yy} = \varepsilon_{\parallel} > 0$, this is denoted as Type I (a) and $\varepsilon_{\perp} > 0$, $\varepsilon_{\parallel} < 0$, the Type II (b). 4

1.2 Examples of hyperbolic metamaterials. a) Layered metal-dielectric structure; b) hyper-lens; c) multilayer fishnet; d) nanorod arrays; e) arrays of metal-dielectric nanopyramids; f) graphene metamaterials. Reproduced with permission from [15]. 5

1.3 Figures a,c,e,f) show the behavior of the real part of $\varepsilon_{\parallel}$ and $\varepsilon_{\perp}$ calculated using the EMT. In the insets for each figure is reported the hyperbolic anisotropy sketch, the blurry blu area denotes the HMM type 1 and the blur yellow area denotes the HMM type 2. The figures b,d,f,h) show the behavior of the related imaginary part of $\varepsilon_{\parallel}$ and $\varepsilon_{\perp}$ also calculated using the EMT. The analyzed ε Near Zero and Pole HMM are the following, from the top to the bottom, Ag/ITO 20/20 nm, Ag/Al_2O_3 20/20 nm, Ag/AZO 20/20 nm and finally only an εNZ constituted by Au/Al_2O_3 10/30 nm. 8

1.4 Sketch of the field components of a SPP supported by a metal-dielectric interface. The mode is transverse magnetic, exhibiting electric field components normal to the interface ($y - axis$) and along the propagation direction ($z - axis$). The mode profile (blue) represents the magnitude of the corresponding magnetic field, itself oriented along the $x - axis$, as a function of y. Picture readapted with permission from [50] 9

1.5 Dispersion relation calculated for a plasmon thin Ag layer according with the K_{SPP} relation (Eq. 1.12). $cK/(\varepsilon d)^{1/2}$ represents the light line, ω_p is the plasma resonance and the ω_{sp} is the surface plasmon resonance. 11

1.6 a) Resonance cone calculation for the considered εNZP HMM. b) Super-collimation at the εNZP wavelength and c) propagation through a simple εNZ HMM d) Confocal analysis of the εNZP HMM. Light impinging on the HMM at the ϵNZP wavelength shows a much smaller FWHM with respect to a shorter wavelength in the type I regime. e) Super-collimation through the HMM of light coming from a 40 nm width excitation slit. Propagation in the HMM lasts for more than 100 Rayleigh lengths. Adapted from Ref. [47] 15

2.1 The sketch shows the real constitutive parts of an ellipsometer and the electromagnetic wave composed from both polarizations. Figure readapted from [93]. 21
2.2 a) The main structure of the NEA model, it is realized from a parallelepiped divided in layers that constitute the superstrate, the layer of materials and the substrate. b) A sketch of the mesh directly controlled from the physics, the larger part are meshed with a normal weave while for the small parts has been used a fine mesh weave. c)Here it is shown the application direction of the periodic boundary condition from periodic port. d, e) report the 2D and 3D electric and magnetic field vectors drawing respectively. Figure readapted from the main paper and the supplementary electronic information [93]. 25
2.3 a-b) R_p reflectances at different angles of the incident light and T transmittances at the normal incidence, calculated by the NEA and TMM models and measured by ellipsometer for the single Ag layer. The inset of a) shows the analyzed structure constituted by a single metal layer. c) The experimental and numerical ellipsometer parameters Ψ and Δ for that system. d-e) R_p reflectances at different angles of the incident light and T transmittances at the normal incidence, calculated by the NEA and TMM models and measured by ellipsometer for the HMM. The inset of d) shows the analyzed structure constituted by five bilayers of Ag/ITO 20/20 nm. f) The experimental and numerical ellipsometer parameters Ψ and Δ for the HMM. 27
2.4 a-b) R_p reflectances at different angles of the incident light and T transmittances at the normal incidence, measured and calculated by the NEA and TMM models for the 2BMM. The inset of a) shows the analyzed structure where the thickness of the dielectric layer placed between the two metal varying its thickness. c) The experimental and numerical calculated ellipsometer parameters Ψ and Δ for the 2BMM and d) the R_s measured and numerically calculated. e-f) R_p reflectances at different angles of the incident light and T transmittances at the normal incidence, measured and calculated by the NEA and TMM models for the 3BMM. g) The experimental and numerical calculated ellipsometer parameters Ψ and Δ for the 3BMM and h) the R_s measured and numerically calculated. 29
2.5 Plots of the dispersion relations of the a) 2BMM and c) the 3BMM. b-d) Modal analysis for the two systems (orange curves), with the permitted region delimited by the dielectric light line (blue curve). Figure readapted from reference [93] 30

2.6 a)Reflectance map calculated by varying the incident wavelength λ_i and angle θ_i. The dashed white line drawn on the field map indicates the position of the Brewster angle for this structure that has been used as the incident angle in the numerical simulations whose results are reported in the graph. b) The evaluation of the Brewster angle for p- and s-polarization at $\lambda = 750\,nm$. c) R_p reflectances calculated for the sensor realized by using the 3BMM with and without an AZO coating layer of $10\,nm$ on its top surface (solid black and dashed-dot red lines, respectively). 31
2.7 Calculated reflectance, using NEA analysis, at incident angle of 50° varying the dielectric layer between the metals ones. The vertical dashed lines indicate the resonant wavelengths. a) For the MIMI made by ITO it has been evaluated the case with a thickness of $t = 65\,nm$ and b)for ITO $t = 85\,nm$, c) for ZnO $t = 83\,nm$. The dashed white lines represent for each case the desired single mode at one specific wavelength. d-f) The EMT analysis for the three cavities made by ITO and ZnO respectively have been reported. 33
2.8 Calculated dispersion relation according with the Fabry-Pérot condition for a MIMI cavity composed by a) ITO $t = 65\,nm$, b) ITO $t = 85\,nm$ and c) ZnO $t = 83\,nm$. The related mode analysis (d-f) for the three considered MIMI cavities. The vertical dashed lines indicate the resonant wavelengths. The insets show the related mode profile evaluated for each structure by using COMSOL Multiphisycs. 34
2.9 a) Reflectances (p-pol) and transmittance at different incident angles for the MIMI (A) (Ag/ITO/Ag/ITO)composed of ITO layer $t_1 = 65\,nm$, the inset reports a schematic view of the whole fabricated system with the related thickness of each layer. b,c) Ψ and Δ for MIMI (A) with ITO layer $t_1 = 65\,nm$. d) Reflectances (p-pol), and transmittance at different incident angles for the MIMI (B) composed of the ITO layer with $t_1 = 85\,nm$, the inset shows the whole fabricated system with the new layers thickness. d,e) Ψ and Δ for the MIMI (B) with ITO layer $t_1 = 85\,nm$. g-h) The CIE chromaticity xy coordinate plots with the corresponding points for the measured transmittance at 0° (T_0) and reflectance at different angles from 50° to 70° ($R_{50} - R_{60} - R_{70}$) for the two ITO-based MIMI. The red and blue squares indicate the points related to numerical transmittances and reflectances, respectively. Figure readapted from reference [139]. 36
2.10 a) Reflectance (s-pol) at different incident angles for the system made by the ITO slab of $65\,nm$. b,c) Numerical results for reflectances (p and s-pol) and transmittance, Ψ and Δ. d)Reflectance (s-pol) at different incident angles for the system made by the ITO slab of $85\,nm$. e,f) Numerical results for reflectances (p and s-pol) and transmittance, Ψ and Δ. 37

2.11 Electric field maps for the MIMI(A) composed of Ag/ITO/Ag/ITO with thicknesses of $20/65/20/20\,nm$ respectively evaluated at an incidence angle of 50°. a , c) at the resonant wavelength of $\lambda = 480\,nm$ for p- and s-polarization where the resonant mode inside the ITO nano-cavity is shown. b, d) Out of resonance at $\lambda = 700\,nm$ for both polarizations. Electric field maps for the MIMI(B) composed of Ag/ITO/Ag/ITO with thicknesses of $20/85/20/20\,nm$ respectively evaluated at an incidence angle of 50°. g , h) at the resonant wavelength of $\lambda = 532\,nm$ for p- and s-polarization where the resonant mode inside the ITO nano-cavity is shown. f, h) Out of resonance at $\lambda = 700\,nm$ for both polarizations. Figure readapted from references [139]. . . 38

2.12 a) The four pictures are referred to the MIMI (A). The color of the MIMI passes from blue to gold when observed in transmission or in reflection, respectively. b) The graph reports the $< \varepsilon_2 >$ at three different incident angles while the inset depicts the $< \varepsilon_1 >$.c) The pictures are referred to the MIMI (B). The nano-cavity color passes from green to purple when it is observed in transmission or in reflection, respectively. d) The graph shows the $< \varepsilon_2 >$ at three different incident angles, while the inset shows the $< \varepsilon_1 >$ behavior. Figure readapted from reference [139]. 39

2.13 a) Reflectances (p-pol), and transmittance at different incident angles for the MIMI (Ag($20\,nm$)/ ZnO($83\,nm$)/ Ag($20\,nm$)/ ZnO($20\,nm$)). b,c) Ψ and Δ curves for the fabricated nano-cavity, the inset reports a schematic view of the MIMI with the related thickness of each layer. d) The CIE chromaticity xy coordinate plots with the corresponding points for the measured transmittance at 0° (red dot T_0) and for the reflectance at different angles from 50° to 70° (blue dots $R_{50} - R_{60} - R_{70}$). The red and blue squares indicate the points related to numerical transmittances and reflectances, respectively. e) Pictures referred to Ag/ZnO/Ag/ZnO system taken at different incident/view angles. f) $< \varepsilon_2 >$ at three different incident angles, while the inset shows the $< \varepsilon_1 >$ curves. Figure readapted from reference [139]. 41

3.1 Energy level diagram for a molecule excited by a single photon (dotted line) or by two photons (straight line), from the ground level to an excited level. In both case, the compound may be activated or may release energy through radiative or non-radiative processes. Figure readapted from reference [189] 46

3.2 Laser intensity dependency of the voxel size. If the laser intensity is below the polymerization threshold no polymerization happens, else only the portion of the Gaussian beam higher than the threshold will lead to the voxel polymerization. Over the second threshold, the resist explodes and is permanently damaged. Figure readapted from reference [189] 47

3.3 The sketch shows the two main approaches for TP-DLW and our implementation. a) Laser writing from the bottom using a matching oil and the photo-resin on the top substrate, b) the object is dipped into the resist. c) The sketch presents the coating MIMI metamaterials on the substrate that allows enabling the hyper resolution in the TP-DLW process. 48
3.4 a) A sketch of the MIMI nano-cavity. b-c) Numerical reflectance and transmittance map, respectively, at normal incidence varying the ZnO thickness that constitutes the optical nano-cavity. The value of $t_{cav} = 160\,nm$ has been choose to obtain a minimum in reflectance and maximum in transmission at $\lambda = 400\,nm$ and $\lambda = 780\,nm$. d) Effective medium theory (EMT) calculated for a four layer system showing the ε_{NZ} modes at the two resonant wavelengths. Figure readapted from reference [202, 203]. 50
3.5 a-b) Numerical and experimental reflectance p-pol, c-d) numerical and experimental transmittance p-pol e-f) Numerical and experimental reflectance s-pol and g-h) numerical and experimental transmittance s-pol map at different incident angle for the MIMI device showing the two minimum and two maximum respectively at $\lambda = 400\,nm$ and $\lambda = 780\,nm$. 51
3.6 Schematic view of the optical setup used to fully characterize the produced PSF through the MIMI device and the bare glass substrate 52
3.7 a) Calculated resonant cone angle of the fabricated MIMI. b-c)The experimental PSF reveals a beam shrinking of about 36% and 20% in the MIMI nano-cavity with respect the bare glass for the two input objectives. Experimental transmitted spot through the bare glass and MIMI nano-cavity at $\lambda = 400\,nm$ and at $\lambda = 780\,nm$, acquired through the beam profiler, d-g) for the four considered cases with the $50x$, and h-m) with the $10x$ input objective. Figure readapted from reference [202, 203]. 53
3.8 AFM morphology of a fabricated grating, pitch $400\,nm$ with a Laser Power (LP) of $20\,mW$ and a Scan Speed (SS) of $4\,mm/s$ a) through the classical glass substrate and b) through the MIMI nano-cavity. c) Profiles comparison of the two fabricated grating. d) Grating realized through the MIMI nano-cavity using a LP of $12\,mW$ and a SS of $4mm/s$ producing an element height of $\sim 5 \pm 2\,nm$. e) Height and Width for all the fabricated gratings at different laser power and scan speed using the glass substrate (black symbols) and the MIMI (red symbols). f) Height as function of the LP for glass (black square) and MIMI (red squares) substrates showing an average reduction of $\sim 89\%$. Figure readapted from reference [202, 203]. . . 54

3.9 a) Original portrait and b) TP-DLW software model of the bas-relief *"Lady with an Ermine"*. c) Optical image of the realized 3D sample collected with an objective with magnification 40X through the MIMI substrate and enlighten from the top. d) AFM morphology of the fabricated sample. e-f) Emission confocal images of the bas-relief. In particular e) reports the base of the 3D print showing the silhouette of the "Lady". f) Image collected close to the top ($H_z \sim 0.5\mu m$) of the portrait and some details are shown as the hand, the shoulders, and parts of dress and face. g) A whole 3D sample image has been reconstructed highlighting the reliability to "print" very well all particulars at the nanoscale. The scale-bar in each picture is $20\,\mu m$. 55

4.1 The Figure depicts the state of art, a) shows the evolution of optics element from a classical lens to metalaneses passing through the Fresnel ones (Sketch readapted from reference [223]). b) is an examples of different realized metasurfaces and metalenses as already presented by [226]. c) depicts two complicate examples of all dielectric metalenses realized by EBL, (taken from [235]). 59

4.2 Global optimization based on a generative neural network (GAN) opportunely modified. a) Schematic view of nano ridges that constitutes the metalens. b) Schematic representation of the conditional GANs code for metalens generation. The generator is built by a neural network, deconvolution layers (dconv) and a Gaussian filter. An identity shortcut connection is also used by the electric near field equation. The input of GANs code are the device's geometrical parameters as height (H), width (W), period (Λ) and finally wavelength (λ). During each iteration of training, a batch of devices is generated and for each device efficiency gradients (g) are calculated using forward electromagnetic simulations. These gradients are propagated through the network to update the weights of neurons (W_n). The GAN verifies that the near field E(x; y0) produced by the metasurface satisfy the Fresnel diffraction formula (E(u; f)). Then, the GAN algorithm compares the electrical near field of the actual geometrical parameters and the considered wavelength with the one of a classical lens having the same focal length. Only the parameters that respect the fixed condition over the focal length and the maximum lens transversal dimension at multiple wavelengths are stored. c) Revolved sketch of the constitutive elements. d) Examples of produced element disposition in function of wavelength and deflection angle, varying the height, width and period of the constitutive metalens element. e) Histogram efficiency used to chose the element disposition. Figure readapted from reference [203, 242]. 61

4.3 a) Beam envelope at the focal plane (common for five different wavelengths) calculated through the Fresnel diffraction formula by using the near field $E(x, y_0)$ distribution provided by the GAN algorithm. b) Electric field maps evaluated by using the beam envelope model based on Rigorous Coupled Wave Analysis (RCWA) for five different wavelengths along the propagation XZ plane together with its corresponding focal spot image (XY plane). c) Beam profile retrieved at the common XY focal plane (FP, $f = 1.14\,mm$) by calculating the Point Spread Function (PSF); d) Schematic view of numerically designed apochromatic metalens. Figure readapted from reference [203, 242]. 63
4.4 The phase shift analyzed for different wavelengths at the same focal length and along the lens diameter. The analyzed wavelengths are: a) 450 nm, b) 532 nm, c) 633 nm, d) 780 nm and finally e) 1000 nm. 64
4.5 a) AFM morphological characterization of the metalenses with b) the related height and width profile obtained from a transversal cut. c) Optical image of the metalenses matrix acquired with microscope with magnification 20x, (zoom at 50x in the inset). Particular of one metalens at 50x observed using band pass filter (BPF) at d) 390 nm, e) 450 nm and f) 780 nm. Figure readapted from reference [203, 242]. 65
4.6 a) A perspective view of the optical setup used to characterize the metalens for the focal length. b) The top view with the detailed elements used in that setup. c) The sketch represents the initial confocal configuration, and d) the metalens focal length is evaluated removing the input objective (red arrow) and moving along z the output objective (32x) until the produced output spot is again the smallest one. 67
4.7 Stacks of the beam divergence from the focal length (1.14 mm) indicated as z=0 to $\pm 200\,\mu m$ at a) $\lambda = 405\,nm$ b)$\lambda = 532\,nm$ c)$\lambda = 633\,nm$ d) using the previous three lasers at the same time and e) using a Xenon lamp source. f) Full Width Half Maximum (FWHM) for all considered cases. It is 0.9 μm for each single laser (BL, GL, RL), 1.5 μm for the three lasers (3L) and 1.65 μm for the white lamp (WL). g) The DOF evaluated for each input laser, has been calculated considering the FWHM of the produced spot along the propagation direction z in the range from $-200\,\mu m$ to $200\,\mu m$. h) CIE chromaticity xy-coordinate plot for each laser wavelength, combination of them (3L) and white lamp (WL); for laser with $\lambda = 445\,nm$ and the combination with the GL and RL producing RGB spot (grey circle). Figure readapted from reference [203, 242]. 69

B.1 The sketch represents the block diagram of the TMM coded in Matlab 77

Bibliography

(1) Shelby, R.; Smith, D.; Nemat-Nasser, S.; Schultz, S. Microwave transmission through a two-dimensional, isotropic, left-handed metamaterial. *Applied Physics Letters* **2001**, *78*, 489–491.

(2) Smith, D. R.; Padilla, W. J.; Vier, D.; Nemat-Nasser, S. C.; Schultz, S. Composite medium with simultaneously negative permeability and permittivity. *Physical review letters* **2000**, *84*, 4184.

(3) Kshetrimayum, R. S. A brief intro to metamaterials. *IEEE Potentials* **2004**, *23*, 44–46.

(4) Engheta, N.; Ziolkowski, R. W., *Metamaterials: physics and engineering explorations*; John Wiley & Sons: 2006.

(5) Zouhdi, S.; Sihvola, A.; Vinogradov, A. P., *Metamaterials and plasmonics: fundamentals, modelling, applications*; Springer Science & Business Media: 2008.

(6) Shelby, R. A.; Smith, D. R.; Schultz, S. Experimental verification of a negative index of refraction. *Science* **2001**, *292*, 77–79.

(7) Pendry, J. B. Negative refraction. *Contemporary Physics* **2004**, *45*, 191–202.

(8) Veselago, V. G. THE ELECTRODYNAMICS OF SUBSTANCES WITH SIMULTANEOUSLY NEGATIVE VALUES OF IMG align= ABSMIDDLE alt= ? eps/IMG AND μ. *Physics-Uspekhi* **1968**, *10*, 509–514.

(9) Rainsford, T. J.; Mickan, S. P.; Abbott, D. In *Smart Structures, Devices, and Systems II*, 2005; Vol. 5649, pp 826–838.

(10) Nayyar, A.; Palai, G; Tandon, A.; Singh, B. Realization of absorber, reflector and transmitter using single photonic structure. *Optik* **2019**, *180*, 962–966.

(11) Alici, K. B.; Özbay, E. Radiation properties of a split ring resonator and monopole composite. *Physica status solidi (b)* **2007**, *244*, 1192–1196.

(12) Brun, M.; Guenneau, S.; Movchan, A. B. Achieving control of in-plane elastic waves. *Applied physics letters* **2009**, *94*, 061903.

(13) Sievenpiper, D.; Zhang, L.; Broas, R. F.; Alexopolous, N. G.; Yablonovitch, E., et al. High-impedance electromagnetic surfaces with a forbidden frequency band. *IEEE Transactions on Microwave Theory and techniques* **1999**, *47*, 2059–2074.

(14) Pendry, J. B.; Smith, D. R. Reversing light with negative refraction. *Physics today* **2004**, *57*, 37–43.

(15) Poddubny, A.; Iorsh, I.; Belov, P.; Kivshar, Y. Hyperbolic metamaterials. *Nature photonics* **2013**, *7*, 948.

(16) Smith, D.; Schurig, D Electromagnetic wave propagation in media with indefinite permittivity and permeability tensors. *Physical Review Letters* **2003**, *90*, 077405.

(17) Sreekanth, K.; ElKabbash, M.; Caligiuri, V.; Singh, R.; De Luca, A.; Strangi, G. New Directions in Thin Film Nanophotonics.

(18) Fisher, R.; Gould, R. Resonance cones in the field pattern of a short antenna in an anisotropic plasma. *Physical Review Letters* **1969**, *22*, 1093.

(19) Alekseyev, L. V.; Podolskiy, V. A.; Narimanov, E. E. Homogeneous hyperbolic systems for terahertz and far-infrared frequencies. *Advances in Optoelectronics* **2012**, *2012*.

(20) Shen, L.; Yang, T.-J.; Chau, Y.-F. Effect of internal period on the optical dispersion of indefinite-medium materials. *Physical Review B* **2008**, *77*, 205124.

(21) Orlov, A. A.; Voroshilov, P. M.; Belov, P. A.; Kivshar, Y. S. Engineered optical nonlocality in nanostructured metamaterials. *Physical Review B* **2011**, *84*, 045424.

(22) Chebykin, A.; Orlov, A.; Vozianova, A.; Maslovski, S. I.; Kivshar, Y. S.; Belov, P. A. Nonlocal effective medium model for multilayered metal-dielectric metamaterials. *Physical Review B* **2011**, *84*, 115438.

(23) Chebykin, A.; Orlov, A.; Simovski, C.; Kivshar, Y. S.; Belov, P. A. Nonlocal effective parameters of multilayered metal-dielectric metamaterials. *Physical Review B* **2012**, *86*, 115420.

(24) Hoffman, A. J.; Alekseyev, L.; Howard, S. S.; Franz, K. J.; Wasserman, D.; Podolskiy, V. A.; Narimanov, E. E.; Sivco, D. L.; Gmachl, C. Negative refraction in semiconductor metamaterials. *Nature materials* **2007**, *6*, 946.

(25) Cortes, C.; Newman, W; Molesky, S; Jacob, Z Quantum nanophotonics using hyperbolic metamaterials. *Journal of Optics* **2012**, *14*, 063001.

(26) Bogdanov, A.; Suris, R. A. Effect of the anisotropy of a conducting layer on the dispersion law of electromagnetic waves in layered metal-dielectric structures. *JETP letters* **2012**, *96*, 49–55.

(27) Krishnamoorthy, H. N.; Jacob, Z.; Narimanov, E.; Kretzschmar, I.; Menon, V. M. Topological transitions in metamaterials. *Science* **2012**, *336*, 205–209.

(28) Vincenti, M.; De Ceglia, D; Rondinone, V; Ladisa, A; D?Orazio, A; Bloemer, M.; Scalora, M Loss compensation in metal-dielectric structures in negative-refraction and super-resolving regimes. *Physical Review A* **2009**, *80*, 053807.

(29) Ni, X.; Ishii, S.; Thoreson, M. D.; Shalaev, V. M.; Han, S.; Lee, S.; Kildishev, A. V. Loss-compensated and active hyperbolic metamaterials. *Optics express* **2011**, *19*, 25242–25254.

(30) Boltasseva, A.; Atwater, H. A. Low-loss plasmonic metamaterials. *Science* **2011**, *331*, 290–291.

(31) Naik, G. V.; Liu, J.; Kildishev, A. V.; Shalaev, V. M.; Boltasseva, A. Demonstration of Al: ZnO as a plasmonic component for near-infrared metamaterials. *Proceedings of the National Academy of Sciences* **2012**, *109*, 8834–8838.

(32) Jacob, Z.; Alekseyev, L. V.; Narimanov, E. Optical hyperlens: far-field imaging beyond the diffraction limit. *Optics express* **2006**, *14*, 8247–8256.

(33) Salandrino, A.; Engheta, N. Far-field subdiffraction optical microscopy using metamaterial crystals: Theory and simulations. *Physical Review B* **2006**, *74*, 075103.

(34) Liu, Z.; Lee, H.; Xiong, Y.; Sun, C.; Zhang, X. Far-field optical hyperlens magnifying sub-diffraction-limited objects. *Science* **2007**, *315*, 1686–1686.

(35) Smolyaninov, I. I.; Hung, Y.-J.; Davis, C. C. Magnifying superlens in the visible frequency range. *Science* **2007**, *315*, 1699–1701.

(36) Silveirinha, M.; Engheta, N. Tunneling of electromagnetic energy through subwavelength channels and bends using ε-near-zero materials. *Physical review letters* **2006**, *97*, 157403.

(37) Alu, A.; Silveirinha, M. G.; Salandrino, A.; Engheta, N. Epsilon-near-zero metamaterials and electromagnetic sources: Tailoring the radiation phase pattern. *Physical review B* **2007**, *75*, 155410.

(38) Pollard, R.; Murphy, A; Hendren, W.; Evans, P.; Atkinson, R; Wurtz, G.; Zayats, A.; Podolskiy, V. A. Optical nonlocalities and additional waves in epsilon-near-zero metamaterials. *Physical review letters* **2009**, *102*, 127405.

(39) Feng, S.; Halterman, K. Coherent perfect absorption in epsilon-near-zero metamaterials. *Physical Review B* **2012**, *86*, 165103.

(40) Xu, Y.; Chan, C.; Chen, H. Goos-Hänchen effect in epsilon-near-zero metamaterials. *Scientific reports* **2015**, *5*, 8681.

(41) Ciattoni, A.; Rizza, C.; Marini, A.; Falco, A. D.; Faccio, D.; Scalora, M. Enhanced nonlinear effects in pulse propagation through epsilon-near-zero media. *Laser & Photonics Reviews* **2016**, *10*, 517–525.

(42) Garnett, J. M. Colours in metal glasses and in metallic films. *Philosophical Transactions of the Royal Society of London. Series A, Containing Papers of a Mathematical or Physical Character* **1904**, *203*, 385–420.

(43) Garnett, J. M. Colours in metal glasses, in metallic films, and in metallic solutions.?II. *Philosophical Transactions of the Royal Society of London. Series A, Containing Papers of a Mathematical or Physical Character* **1906**, *205*, 237–288.

(44) Kocaman, S; Aras, M.; Hsieh, P; McMillan, J.; Biris, C.; Panoiu, N.; Yu, M.; Kwong, D.; Stein, A; Wong, C. Zero phase delay in negative-refractive-index photonic crystal superlattices. *Nature Photonics* **2011**, *5*, 499.

(45) Molesky, S.; Dewalt, C. J.; Jacob, Z. High temperature epsilon-near-zero and epsilon-near-pole metamaterial emitters for thermophotovoltaics. *Optics express* **2013**, *21*, A96–A110.

(46) Javani, M. H.; Stockman, M. I. Real and imaginary properties of epsilon-near-zero materials. *Physical review letters* **2016**, *117*, 107404.

(47) Caligiuri, V; Dhama, R; Sreekanth, K.; Strangi, G; De Luca, A Dielectric singularity in hyperbolic metamaterials: the inversion point of coexisting anisotropies. *Scientific reports* **2016**, *6*, 20002.

(48) Giannini, V; Zhang, Y; Forcales, M; Rivas, J. G. Long-range surface polaritons in ultra-thin films of silicon. *Optics express* **2008**, *16*, 19674–19685.

(49) Kittel, C. Solid state physics. *Wiley, New York* **1976**, *19*.

(50) Smith, C. L.; Stenger, N.; Kristensen, A.; Mortensen, N. A.; Bozhevolnyi, S. I. Gap and ed plasmons in tapered grooves: a review. *Nanoscale* **2015**, *7*, 9355–9386.

(51) Avrutsky, I.; Salakhutdinov, I.; Elser, J.; Podolskiy, V. Highly confined optical modes in nanoscale metal-dielectric multilayers. *Physical Review B* **2007**, *75*, 241402.

(52) Palermo, G.; Lio, G. E.; Esposito, M.; Ricciardi, L.; Manoccio, M.; Tasco, V.; Passaseo, A.; De Luca, A.; Strangi, G. Biomolecular sensing at the interface between chiral metasurfaces and hyperbolic metamaterials. *ACS Applied Materials & Interfaces* **2020**, *12*, PMID: 32551524, 30181–30188.

(53) Palermo, G.; Sreekanth, K. V.; Maccaferri, N.; Lio, G. E.; Nicoletta, G.; De Angelis, F.; Hinczewski, M.; Strangi, G. Hyperbolic dispersion metasurfaces for molecular biosensing. *Nanophotonics* **2020**, *10*, 295–314.

(54) Bozhevolnyi, S. I. Effective-index modeling of channel plasmon polaritons. *Optics express* **2006**, *14*, 9467–9476.

(55) Kurokawa, Y.; Miyazaki, H. T. Metal-insulator-metal plasmon nanocavities: Analysis of optical properties. *Physical Review B* **2007**, *75*, 035411.

(56) Liu, J.-Q.; Wang, L.-L.; He, M.-D.; Huang, W.-Q.; Wang, D.; Zou, B.; Wen, S. A wide bandgap plasmonic Bragg reflector. *Optics Express* **2008**, *16*, 4888–4894.

(57) Senlik, S. S.; Kocabas, A.; Aydinli, A. Grating based plasmonic band gap cavities. *Optics Express* **2009**, *17*, 15541–15549.

(58) Kuttge, M.; Cai, W.; de Abajo, F. J. G.; Polman, A. Dispersion of metal-insulator-metal plasmon polaritons probed by cathodoluminescence imaging spectroscopy. *Physical Review B* **2009**, *80*, 033409.

(59) Vassant, S.; Archambault, A.; Marquier, F.; Pardo, F.; Gennser, U.; Cavanna, A.; Pelouard, J.-L.; Greffet, J.-J. Epsilon-near-zero mode for active optoelectronic devices. *Physical review letters* **2012**, *109*, 237401.

(60) Tagliabue, G.; Höller, C.; Eghlidi, H.; Poulikakos, D. Proximal gap-plasmon nanoresonators in the limit of vanishing inter-cavity separation. *Nanoscale* **2014**, *6*, 10274–10280.

(61) Refki, S.; Hayashi, S.; Rahmouni, A.; Nesterenko, D. V.; Sekkat, Z. Anticrossing behavior of surface plasmon polariton dispersions in metal-insulator-metal structures. *Plasmonics* **2016**, *11*, 433–440.

(62) Sorger, V. J.; Oulton, R. F.; Yao, J.; Bartal, G.; Zhang, X. Plasmonic fabry-pérot nanocavity. *Nano letters* **2009**, *9*, 3489–3493.

(63) Bozhevolnyi, S.; Volkov, V.; Devaux, E; Laluet, J.-Y.; Ebbesen, T. Channelling surface plasmons. *Applied Physics A* **2007**, *89*, 225–231.

(64) Li, J.; Fok, L.; Yin, X.; Bartal, G.; Zhang, X. Experimental demonstration of an acoustic magnifying hyperlens. *Nature materials* **2009**, *8*, 931.

(65) Rho, J.; Ye, Z.; Xiong, Y.; Yin, X.; Liu, Z.; Choi, H.; Bartal, G.; Zhang, X. Spherical hyperlens for two-dimensional sub-diffractional imaging at visible frequencies. *Nature communications* **2010**, *1*, 143.

(66) Wang, W.; Xing, H.; Fang, L.; Liu, Y.; Ma, J.; Lin, L.; Wang, C.; Luo, X. Far-field imaging device: planar hyperlens with magnification using multi-layer metamaterial. *Optics express* **2008**, *16*, 21142–21148.

(67) Kildishev, A. V.; Chettiar, U. K.; Jacob, Z.; Shalaev, V. M.; Narimanov, E. E. Materializing a binary hyperlens design. *Applied Physics Letters* **2009**, *94*, 071102.

(68) Kildishev, A. V.; Narimanov, E. E. Impedance-matched hyperlens. *Optics letters* **2007**, *32*, 3432–3434.

(69) Lu, D.; Liu, Z. Hyperlenses and metalenses for far-field super-resolution imaging. *Nature communications* **2012**, *3*, 1205.

(70) Purcell, E. M. In *Confined electrons and photons*; Springer: 1995, pp 839–839.

(71) Poddubny, A. N.; Belov, P. A.; Kivshar, Y. S. Spontaneous radiation of a finite-size dipole emitter in hyperbolic media. *Physical Review A* **2011**, *84*, 023807.

(72) Caligiuri, V.; Pezzi, L.; Veltri, A.; De Luca, A. Resonant gain singularities in 1d and 3d metal/dielectric multilayered nanostructures. *ACS Nano* **2016**, *11*, 1012–1025.

(73) Potemkin, A. S.; Poddubny, A. N.; Belov, P. A.; Kivshar, Y. S. Green function for hyperbolic media. *Physical Review A* **2012**, *86*, 023848.

(74) Newman, W. D.; Cortes, C. L.; Jacob, Z. Enhanced and directional single-photon emission in hyperbolic metamaterials. *JOSA B* **2013**, *30*, 766–775.

(75) Shekhar, P.; Atkinson, J.; Jacob, Z. Hyperbolic metamaterials: fundamentals and applications. *Nano Convergence* **2014**, *1*, 14.

(76) Ramakrishna, S. A.; Pendry, J.; Wiltshire, M.; Stewart, W. Imaging the near field. *Journal of Modern Optics* **2003**, *50*, 1419–1430.

(77) Fang, N.; Lee, H.; Sun, C.; Zhang, X. Sub–diffraction-limited optical imaging with a silver superlens. *Science* **2005**, *308*, 534–537.

(78) Jellison Jr, G. Spectroscopic ellipsometry data analysis: measured versus calculated quantities. *Thin Solid Films* **1998**, *313*, 33–39.

(79) Jellison Jr, G.; Merkulov, V.; Puretzky, A.; Geohegan, D.; Eres, G; Lowndes, D.; Caughman, J. Characterization of thin-film amorphous semiconductors using spectroscopic ellipsometry. *Thin Solid Films* **2000**, *377*, 68–73.

(80) Washington, P.; Ong, H.; Dai, J.; Chang, R. Determination of the optical constants of zinc oxide thin films by spectroscopic ellipsometry. *Applied physics letters* **1998**, *72*, 3261–3263.

(81) Jellison Jr, G.; Modine, F. Parameterization of the optical functions of amorphous materials in the interband region. *Applied Physics Letters* **1996**, *69*, 371–373.

(82) Collins, R.; Yang, B. I nsitu ellipsometry of thin-film deposition: Implications for amorphous and microcrystalline Si growth. *Journal of Vacuum Science & Technology B: Microelectronics Processing and Phenomena* **1989**, *7*, 1155–1164.

(83) De Feijter, J.; Benjamins, d. J.; Veer, F. Ellipsometry as a tool to study the adsorption behavior of synthetic and biopolymers at the air–water interface. *Biopolymers* **1978**, *17*, 1759–1772.

(84) Aspnes, D.; Theeten, J.; Hottier, F Investigation of effective-medium models of microscopic surface roughness by spectroscopic ellipsometry. *Physical Review B* **1979**, *20*, 3292.

(85) Porter, M. D.; Bright, T. B.; Allara, D. L.; Chidsey, C. E. Spontaneously organized molecular assemblies. 4. Structural characterization of n-alkyl thiol monolayers on gold by optical ellipsometry, infrared spectroscopy, and electrochemistry. *Journal of the American Chemical Society* **1987**, *109*, 3559–3568.

(86) Jellison Jr, G. Optical functions of silicon determined by two-channel polarization modulation ellipsometry. *Optical Materials* **1992**, *1*, 41–47.

(87) Jellison, G.; Boatner, L. Optical functions of uniaxial ZnO determined by generalized ellipsometry. *Physical Review B* **1998**, *58*, 3586.

(88) Aspnes, D. Minimal-data approaches for determining outer-layer dielectric responses of films from kinetic reflectometric and ellipsometric measurements. *JOSA A* **1993**, *10*, 974–983.

(89) Manjavacas, A.; De Abajo, F. G. Tunable plasmons in atomically thin gold nanodisks. *Nature communications* **2014**, *5*, 3548.

(90) Tompkins, H.; Irene, E. A., *Handbook of ellipsometry*; William Andrew: 2005.

(91) Gorlyak, A.; Khramtsovsky, I.; Solonukha, V. Ellipsometry method application in optics of inhomogeneous media. *Nauchno-Tekhnicheskii Vestnik Informatsionnykh Tekhnologii, Mekhaniki i Optiki* **2015**, *15*, 378.

(92) Butt, H.-J.; Graf, K.; Kappl, M. Measurement of Adsorption Isotherms. *Physics and Chemistry of Interfaces. Weinheim: Wiley-VCH* **2006**, 206–09.

(93) Lio, G. E.; Palermo, G.; Caputo, R.; De Luca, A. A comprehensive optical analysis of nanoscale structures: From thin films to asymmetric nanocavities. *RSC advances* **2019**, *9*, 21429–21437.

(94) Born, M.; Wolf, E., *Principles of optics: electromagnetic theory of propagation, interference and diffraction of light*; Elsevier: 2013.

(95) D Apuzzo, F.; Esposito, M.; Cuscunà, M.; Cannavale, A.; Gambino, S.; Lio, G. E.; De Luca, A.; Gigli, G.; Lupi, S. Mid-infrared plasmonic excitation in indium tin oxide microhole arrays. *ACS Photonics* **2018**, *5*, 2431–2436.

(96) Lio, G. E.; Madrigal, J. B.; Xu, X.; Peng, Y.; Pierini, S.; Couteau, C.; Jradi, S.; Bachelot, R.; Caputo, R.; Blaize, S. Integration of Nanoemitters onto Photonic Structures by Guided Evanescent-Wave Nano-Photopolymerization. *The Journal of Physical Chemistry C* **2019**, *123*, 14669–14676.

(97) Emanuele Lio, G.; De Luca, A.; Umeton, C. P.; Caputo, R. Opto-mechanically induced thermoplasmonic response of unclonable flexible tags with hotspot fingerprint. *Journal of Applied Physics* **2020**, *128*, 093107.

(98) Palermo, G.; Cataldi, U.; Condello, A.; Caputo, R.; Bürgi, T.; Umeton, C.; De Luca, A. Flexible thermo-plasmonics: an opto-mechanical control of the heat generated at the nanoscale. *Nanoscale* **2018**.

(99) Lio, G. E.; Palermo, G.; Caputo, R.; De Luca, A. Opto-mechanical control of flexible plasmonic materials. *Journal of Applied Physics* **2019**, *125*, 082533.

(100) Lio, G. E.; Palermo, G.; De Luca, A.; Caputo, R. Tensile control of the thermal flow in plasmonic heaters realized on flexible substrates. *The Journal of Chemical Physics* **2019**, *151*, 244707.

(101) Caligiuri, V.; De Luca, A. Metal-semiconductor-oxide extreme hyperbolic metamaterials for selectable canalization wavelength. *Journal of Physics D: Applied Physics* **2016**, *49*, 08LT01.

(102) Caligiuri, V.; Palei, M.; Imran, M.; Manna, L.; Krahne, R. Planar Double-Epsilon-Near-Zero Cavities for Spontaneous Emission and Purcell Effect Enhancement. *ACS Photonics* **2018**.

(103) Han, Z.; Forsberg, E.; He, S. Surface plasmon Bragg gratings formed in metal-insulator-metal waveguides. *IEEE Photonics Technology Letters* **2007**, *19*, 91–93.

(104) Newman, W. D.; Cortes, C. L.; Atkinson, J.; Pramanik, S.; DeCorby, R. G.; Jacob, Z. Ferrell–Berreman modes in plasmonic epsilon-near-zero media. *ACS Photonics* **2014**, *2*, 2–7.

(105) Sun, L; Yu, K. Strategy for designing broadband epsilon-near-zero metamaterials. *JOSA B* **2012**, *29*, 984–989.

(106) Sun, L.; Yang, X.; Gao, J. Loss-compensated broadband epsilon-near-zero metamaterials with gain media. *Applied Physics Letters* **2013**, *103*, 201109.

(107) Valentine, J.; Zhang, S.; Zentgraf, T.; Ulin-Avila, E.; Genov, D. A.; Bartal, G.; Zhang, X. Three-dimensional optical metamaterial with a negative refractive index. *Nature* **2008**, *455*, 376.

(108) Shalaev, V. M.; Cai, W.; Chettiar, U. K.; Yuan, H.-K.; Sarychev, A. K.; Drachev, V. P.; Kildishev, A. V. Negative index of refraction in optical metamaterials. *Optics letters* **2005**, *30*, 3356–3358.

(109) Zhang, S.; Fan, W.; Panoiu, N.; Malloy, K.; Osgood, R.; Brueck, S. Experimental demonstration of near-infrared negative-index metamaterials. *Physical review letters* **2005**, *95*, 137404.

(110) Justice, B. J.; Mock, J. J.; Guo, L.; Degiron, A.; Schurig, D.; Smith, D. R. Spatial mapping of the internal and external electromagnetic fields of negative index metamaterials. *Optics Express* **2006**, *14*, 8694–8705.

(111) Talwar, V.; Singh, O.; Singh, R. C. ZnO assisted polyaniline nanofibers and its application as ammonia gas sensor. *Sensors and Actuators B: Chemical* **2014**, *191*, 276–282.

(112) Hjiri, M; Dhahri, R; Omri, K; El Mir, L; Leonardi, S.; Donato, N; Neri, G Effect of indium doping on ZnO based-gas sensor for CO. *Materials Science in Semiconductor Processing* **2014**, *27*, 319–325.

(113) Klem, E. J.; Lewis, J. S.; Temple, D. In *Infrared Technology and Applications XXXVI*, 2010; Vol. 7660, 76602E.

(114) Kim, C. E.; Moon, P.; Kim, S.; Myoung, J.-M.; Jang, H. W.; Bang, J.; Yun, I. Effect of carrier concentration on optical bandgap shift in ZnO: Ga thin films. *Thin Solid Films* **2010**, *518*, 6304–6307.

(115) Sreekanth, K.; De Luca, A; Strangi, G Excitation of volume plasmon polaritons in metal-dielectric metamaterials using 1D and 2D diffraction gratings. *Journal of Optics* **2014**, *16*, 105103.

(116) Sreekanth, K. V.; De Luca, A.; Strangi, G. Experimental demonstration of surface and bulk plasmon polaritons in hypergratings. *Scientific Reports* **2013**, *3*, 3291.

(117) Sreekanth, K. V.; Alapan, Y.; ElKabbash, M.; Ilker, E.; Hinczewski, M.; Gurkan, U. A.; De Luca, A.; Strangi, G. Extreme sensitivity biosensing platform based on hyperbolic metamaterials. *Nature materials* **2016**, *15*, 621.

(118) Maas, R.; Parsons, J.; Engheta, N.; Polman, A. Experimental realization of an epsilon-near-zero metamaterial at visible wavelengths. *Nature Photonics* **2013**, *7*, 907.

(119) Vahala, K. J. Optical microcavities. *Nature* **2003**, *424*, 839–846.

(120) Grover, S.; Moddel, G. Applicability of metal/insulator/metal (MIM) diodes to solar rectennas. *IEEE Journal of Photovoltaics* **2011**, *1*, 78–83.

(121) Guo, C. F.; Sun, T.; Cao, F.; Liu, Q.; Ren, Z. Metallic nanostructures for light trapping in energy-harvesting devices. *Light: Science & Applications* **2014**, *3*, e161.

(122) Grover, S.; Moddel, G. Engineering the current–voltage characteristics of metal–insulator–metal diodes using double-insulator tunnel barriers. *Solid-State Electronics* **2012**, *67*, 94–99.

(123) Hosseini, A.; Massoud, Y. A low-loss metal-insulator-metal plasmonic bragg reflector. *Optics Express* **2006**, *14*, 11318–11323.

(124) Zhang, Q.; Huang, X.-G.; Lin, X.-S.; Tao, J.; Jin, X.-P. A subwavelength coupler-type MIM optical filter. *Optics Express* **2009**, *17*, 7549–7554.

(125) Wang, G.; Lu, H.; Liu, X.; Mao, D.; Duan, L. Tunable multi-channel wavelength demultiplexer based on MIM plasmonic nanodisk resonators at telecommunication regime. *Optics Express* **2011**, *19*, 3513–3518.

(126) Hill, M. T.; Marell, M.; Leong, E. S.; Smalbrugge, B.; Zhu, Y.; Sun, M.; Van Veldhoven, P. J.; Geluk, E. J.; Karouta, F.; Oei, Y.-S., et al. Lasing in metal-insulator-metal sub-wavelength plasmonic waveguides. *Optics Express* **2009**, *17*, 11107–11112.

(127) Choo, H.; Kim, M.-K.; Staffaroni, M.; Seok, T. J.; Bokor, J.; Cabrini, S.; Schuck, P. J.; Wu, M. C.; Yablonovitch, E. Nanofocusing in a metal–insulator–metal gap plasmon waveguide with a three-dimensional linear taper. *Nature Photonics* **2012**, *6*, 838.

(128) Kim, H.-T.; Park, J.-H.; Kim, Y.-K.; Kwon, Y. In *2002 IEEE MTT-S International Microwave Symposium Digest (Cat. No. 02CH37278)*, 2002; Vol. 1, pp 341–344.

(129) Thissen, P.; Schindler, B.; Diesing, D.; Hasselbrink, E. Optical response of metal–insulator–metal heterostructures and their application for the detection of chemicurrents. *New Journal of Physics* **2010**, *12*, 113014.

(130) Banerjee, P.; Perez, I.; Henn-Lecordier, L.; Lee, S. B.; Rubloff, G. W. Nanotubular metal–insulator–metal capacitor arrays for energy storage. *Nature Nanotechnology* **2009**, *4*, 292.

(131) Miyazaki, H. T.; Kurokawa, Y. Squeezing visible light waves into a 3-nm-thick and 55-nm-long plasmon cavity. *Physical Review Letters* **2006**, *96*, 097401.

(132) Stegeman, G.; Wallis, R.; Maradudin, A. Excitation of surface polaritons by end-fire coupling. *Optics Letters* **1983**, *8*, 386–388.

(133) Zia, R.; Selker, M. D.; Catrysse, P. B.; Brongersma, M. L. Geometries and materials for subwavelength surface plasmon modes. *JOSA A* **2004**, *21*, 2442–2446.

(134) Dereshgi, S. A.; Okyay, A. K. Large area compatible broadband superabsorber surfaces in the VIS-NIR spectrum utilizing metal-insulator-metal stack and plasmonic nanoparticles. *Optics Express* **2016**, *24*, 17644–17653.

(135) Sharma, P.; Dinesh, K. V. In *2017 Progress in Electromagnetics Research Symposium-Fall (PIERS-FALL)*, 2017, pp 2747–2751.

(136) Miyazaki, H. T.; Kurokawa, Y. Controlled plasmon resonance in closed metal/insulator/metal nanocavities. *Applied Physics Letters* **2006**, *89*, 211126.

(137) Neutens, P.; Van Dorpe, P.; De Vlaminck, I.; Lagae, L.; Borghs, G. Electrical detection of confined gap plasmons in metal–insulator–metal waveguides. *Nature Photonics* **2009**, *3*, 283.

(138) Todisco, F.; Esposito, M.; Panaro, S.; De Giorgi, M.; Dominici, L.; Ballarini, D.; Fernández-Domínguez, A. I.; Tasco, V.; Cuscuna, M.; Passaseo, A., et al. Toward cavity quantum electrodynamics with hybrid photon gap-plasmon states. *ACS Nano* **2016**, *10*, 11360–11368.

(139) Lio, G. E.; Ferraro, A.; Giocondo, M.; Caputo, R.; De Luca, A. Color Gamut Behavior in Epsilon Near-Zero Nanocavities during Propagation of Gap Surface Plasmons. *Advanced Optical Materials* **2020**, *8*, 2000487.

(140) Lee, Y.-J.; Ruby, D. S.; Peters, D. W.; McKenzie, B. B.; Hsu, J. W. ZnO nanostructures as efficient antireflection layers in solar cells. *Nano Letters* **2008**, *8*, 1501–1505.

(141) Manor, A.; Katz, E. A.; Tromholt, T.; Krebs, F. C. Electrical and Photo-Induced Degradation of ZnO Layers in Organic Photovoltaics. *Advanced Energy Materials* **2011**, *1*, 836–843.

(142) Tritschler, T; Mücke, O.; Wegener, M; Morgner, U; Kärtner, F. Evidence for third-harmonic generation in disguise of second-harmonic generation in extreme nonlinear optics. *Physical Review Letters* **2003**, *90*, 217404.

(143) Neumann, U.; Grunwald, R.; Griebner, U.; Steinmeyer, G.; Schmidbauer, M.; Seeber, W. Second-harmonic performance of a-axis-oriented ZnO nanolayers on sapphire substrates. *Applied Physics Letters* **2005**, *87*, 171108.

(144) Yayapao, O.; Thongtem, T.; Phuruangrat, A.; Thongtem, S. Ultrasonic-assisted synthesis of Nd-doped ZnO for photocatalysis. *Materials Letters* **2013**, *90*, 83–86.

(145) Jaramillo, T. F.; Baeck, S.-H.; Kleiman-Shwarsctein, A.; McFarland, E. W. Combinatorial electrochemical synthesis and screening of mesoporous ZnO for photocatalysis. *Macromolecular Rapid Communications* **2004**, *25*, 297–301.

(146) Han, Z.; Bozhevolnyi, S. I. Plasmon-induced transparency with detuned ultracompact Fabry-Perot resonators in integrated plasmonic devices. *Optics Express* **2011**, *19*, 3251–3257.

(147) Azzam, R. M.; Bashara, N. M.; Ballard, S. S. Ellipsometry and polarized light. *Physics Today* **1978**, *31*, 72.

(148) Ager, C.; Hughes, H. Optical properties of stratified systems including lamellar gratings. *Physical Review B* **1991**, *44*, 13452.

(149) Xu, T.; Shi, H.; Wu, Y.-K.; Kaplan, A. F.; Ok, J. G.; Guo, L. J. Structural colors: from plasmonic to carbon nanostructures. *Small* **2011**, *7*, 3128–3136.

(150) Chen, J.; Yang, J.; Chen, Z.; Fang, Y.-J.; Zhan, P.; Wang, Z.-L. Plasmonic reflectors and high-Q nano-cavities based on coupled metal-insulator-metal waveguides. *AIP Advances* **2012**, *2*, 012145.

(151) Gu, Y.; Zhang, L.; Yang, J. K.; Yeo, S. P.; Qiu, C.-W. Color generation via subwavelength plasmonic nanostructures. *Nanoscale* **2015**, *7*, 6409–6419.

(152) Segal, E.; Weissman, A.; Gachet, D.; Salomon, A. Hybridization between nanocavities for a polarimetric color sorter at the sub-micron scale. *Nanoscale* **2016**, *8*, 15296–15302.

(153) Caligiuri, V.; Biffi, G.; Palei, M.; Martín-García, B.; Pothuraju, R. D.; Bretonnière, Y.; Krahne, R. Angle and Polarization Selective Spontaneous Emission in Dye-Doped Metal/Insulator/Metal Nanocavities. *Advanced Optical Materials* **2020**, *8*, 1901215.

(154) Shaltout, A. M.; Kim, J.; Boltasseva, A.; Shalaev, V. M.; Kildishev, A. V. Ultrathin and multicolour optical cavities with embedded metasurfaces. *Nature communications* **2018**, *9*, 1–7.

(155) Li, Z.; Butun, S.; Aydin, K. Large-area, lithography-free super absorbers and color filters at visible frequencies using ultrathin metallic films. *ACS Photonics* **2015**, *2*, 183–188.

(156) Snyder, A. W.; Love, J. D. Goos-Hänchen shift. *Applied Optics* **1976**, *15*, 236–238.

(157) Wild, W. J.; Giles, C. L. Goos-Hänchen shifts from absorbing media. *Physical Review A* **1982**, *25*, 2099.

(158) Lai, H.; Cheng, F.; Tang, W. Goos–Hänchen effect around and off the critical angle. *JOSA A* **1986**, *3*, 550–557.

(159) De Fornel, F., *Evanescent waves: from Newtonian optics to atomic optics*; Springer Science & Business Media: 2001; Vol. 73.

(160) Foster, D. H.; Nöckel, J. U. Methods for 3-D vector microcavity problems involving a planar dielectric mirror. *Optics Communications* **2004**, *234*, 351–383.

(161) Foster, D. H.; Cook, A. K.; Nöckel, J. U. Goos-Hänchen induced vector eigenmodes in a dome cavity. *Optics Letters* **2007**, *32*, 1764–1766.

(162) Jiang, L.; Zeng, S.; Xu, Z.; Ouyang, Q.; Zhang, D.-H.; Chong, P. H. J.; Coquet, P.; He, S.; Yong, K.-T. Multifunctional hyperbolic nanogroove metasurface for submolecular detection. *Small* **2017**, *13*, 1700600.

(163) Sreekanth, K. V.; Zeng, S.; Yong, K.-T.; Yu, T. Sensitivity enhanced biosensor using graphene-based one-dimensional photonic crystal. *Sensors and Actuators B: Chemical* **2013**, *182*, 424–428.

(164) Sreekanth, K. V.; Ouyang, Q.; Sreejith, S.; Zeng, S.; Lishu, W.; Ilker, E.; Dong, W.; ElKabbash, M.; Ting, Y.; Lim, C. T., et al. Phase-Change-Material-Based Low-Loss Visible-Frequency Hyperbolic Metamaterials for Ultrasensitive Label-Free Biosensing. *Advanced Optical Materials* **2019**, 1900081.

(165) Merano, M.; Aiello, A.; 't Hooft, G.; van Exter, M. P.; Eliel, E. R.; Woerdman, J. P. Observation of Goos-Hänchen shifts in metallic reflection. *Optics Express* **2007**, *15*, 15928–15934.

(166) Broadbent, A. D. A critical review of the development of the CIE1931 RGB color-matching functions. *Color Research & Application: Endorsed by Inter-Society Color Council, The Colour Group (Great Britain), Canadian Society for Color, Color Science Association of Japan, Dutch Society for the Study of Color, The Swedish Colour Centre Foundation, Colour Society of Australia, Centre Français de la Couleur* **2004**, *29*, 267–272.

(167) Hashimoto, T.; Yoshino, T. Optical heterodyne sensor using the Goos–Hänchen shift. *Optics Letters* **1989**, *14*, 913–915.

(168) Yin, X.; Hesselink, L. Goos-Hänchen shift surface plasmon resonance sensor. *Applied Physics Letters* **2006**, *89*, 261108.

(169) Yokogawa, S.; Burgos, S. P.; Atwater, H. A. Plasmonic color filters for CMOS image sensor applications. *Nano Letters* **2012**, *12*, 4349–4354.

(170) Roberts, A. S.; Pors, A.; Albrektsen, O.; Bozhevolnyi, S. I. Subwavelength plasmonic color printing protected for ambient use. *Nano Letters* **2014**, *14*, 783–787.

(171) Maier, S. A. Gain-assisted propagation of electromagnetic energy in subwavelength surface plasmon polariton gap waveguides. *Optics Communications* **2006**, *258*, 295–299.

(172) Lal, S.; Link, S.; Halas, N. J. Nano-optics from sensing to waveguiding. *Nature Photonics* **2007**, *1*, 641.

(173) Karalis, A.; Joannopoulos, J.; Soljačić, M. Plasmonic-dielectric systems for high-order dispersionless slow or stopped subwavelength light. *Physical Review Letters* **2009**, *103*, 043906.

(174) Martin-Cano, D.; Martin-Moreno, L.; Garcia-Vidal, F. J.; Moreno, E. Resonance energy transfer and superradiance mediated by plasmonic nanowaveguides. *Nano Letters* **2010**, *10*, 3129–3134.

(175) Ellenbogen, T.; Seo, K.; Crozier, K. B. Chromatic plasmonic polarizers for active visible color filtering and polarimetry. *Nano Letters* **2012**, *12*, 1026–1031.

(176) Cui, Y.; Hegde, R. S.; Phang, I. Y.; Lee, H. K.; Ling, X. Y. Encoding molecular information in plasmonic nanostructures for anti-counterfeiting applications. *Nanoscale* **2014**, *6*, 282–288.

(177) Zheng, Y.; Jiang, C.; Ng, S. H.; Lu, Y.; Han, F.; Bach, U.; Gooding, J. J. Unclonable Plasmonic Security Labels Achieved by Shadow-Mask-Lithography-Assisted Self-Assembly. *Advanced Materials* **2016**, *28*, 2330–2336.

(178) Smith, A. F.; Patton, P.; Skrabalak, S. E. Plasmonic Nanoparticles as a Physically Unclonable Function for Responsive Anti-Counterfeit Nanofingerprints. *Advanced Functional Materials* **2016**, *26*, 1315–1321.

(179) Xia, Y.; Whitesides, G. M. Soft lithography. *Annual review of materials science* **1998**, *28*, 153–184.

(180) Bratton, D.; Yang, D.; Dai, J.; Ober, C. K. Recent progress in high resolution lithography. *Polymers for Advanced Technologies* **2006**, *17*, 94–103.

(181) Mack, C., *Fundamental principles of optical lithography: the science of microfabrication*; John Wiley & Sons: 2008.

(182) Kim, P.; Kwon, K. W.; Park, M. C.; Lee, S. H.; Kim, S. M.; Suh, K. Y. Soft lithography for microfluidics: a review. **2008**.

(183) Beebe, D. J.; Mensing, G. A.; Walker, G. M. Physics and applications of microfluidics in biology. *Annual review of biomedical engineering* **2002**, *4*, 261–286.

(184) Whitesides, G. M. The origins and the future of microfluidics. *Nature* **2006**, *442*, 368–373.

(185) Anderson, J. R.; Chiu, D. T.; Jackman, R. J.; Cherniavskaya, O.; McDonald, J. C.; Wu, H.; Whitesides, S. H.; Whitesides, G. M. Fabrication of topologically complex three-dimensional microfluidic systems in PDMS by rapid prototyping. *Analytical chemistry* **2000**, *72*, 3158–3164.

(186) Psaltis, D.; Quake, S. R.; Yang, C. Developing optofluidic technology through the fusion of microfluidics and optics. *Nature* **2006**, *442*, 381–386.

(187) Testa, G.; Persichetti, G.; Sarro, P. M.; Bernini, R. A hybrid silicon-PDMS optofluidic platform for sensing applications. *Biomedical optics express* **2014**, *5*, 417–426.

(188) Leclerc, E.; Sakai, Y.; Fujii, T. Microfluidic PDMS (polydimethylsiloxane) bioreactor for large-scale culture of hepatocytes. *Biotechnology progress* **2004**, *20*, 750–755.

(189) Schmidt, V.; Belegratis, M. R., *Laser technology in biomimetics*; Springer: 2016.

(190) Von Freymann, G.; Ledermann, A.; Thiel, M.; Staude, I.; Essig, S.; Busch, K.; Wegener, M. Three-dimensional nanostructures for photonics. *Advanced Functional Materials* **2010**, *20*, 1038–1052.

(191) Röhrig, M.; Thiel, M.; Worgull, M.; Hölscher, H. 3D direct laser writing of nano-and microstructured hierarchical gecko-mimicking surfaces. *Small* **2012**, *8*, 3009–3015.

(192) Göppert-Mayer, M. Elementary processes with two quantum transitions. *Annalen der Physik* **2009**, *18*, 466–479.

(193) Kaiser, W; Garrett, C. Two-photon excitation in Ca F 2: Eu 2+. *Physical review letters* **1961**, *7*, 229.

(194) Zhang, Y.-L.; Chen, Q.-D.; Xia, H.; Sun, H.-B. Designable 3D nanofabrication by femtosecond laser direct writing. *Nano Today* **2010**, *5*, 435–448.

(195) Li, L.; Gattass, R. R.; Gershgoren, E.; Hwang, H.; Fourkas, J. T. Achieving $\lambda/20$ resolution by one-color initiation and deactivation of polymerization. *Science* **2009**, *324*, 910–913.

(196) Xing, J.; Liu, L.; Song, X.; Zhao, Y.; Zhang, L.; Dong, X.; Jin, F.; Zheng, M.; Duan, X. 3D hydrogels with high resolution fabricated by two-photon polymerization with sensitive water soluble initiators. *Journal of Materials Chemistry B* **2015**, *3*, 8486–8491.

(197) Lee, K.-S.; Kim, R. H.; Yang, D.-Y.; Park, S. H. Advances in 3D nano/microfabrication using two-photon initiated polymerization. *Progress in Polymer Science* **2008**, *33*, 631–681.

(198) Tan, D.; Li, Y.; Qi, F.; Yang, H.; Gong, Q.; Dong, X.; Duan, X. Reduction in feature size of two-photon polymerization using SCR500. *Applied physics letters* **2007**, *90*, 071106.

(199) Wu, D.; Wu, S.-Z.; Niu, L.-G.; Chen, Q.-D.; Wang, R.; Song, J.-F.; Fang, H.-H.; Sun, H.-B. High numerical aperture microlens arrays of close packing. *Applied physics letters* **2010**, *97*, 031109.

(200) Passinger, S.; Saifullah, M. S.; Reinhardt, C.; Subramanian, K. R.; Chichkov, B. N.; Welland, M. E. Direct 3D patterning of TiO2 using femtosecond laser pulses. *Advanced Materials* **2007**, *19*, 1218–1221.

(201) Park, S.-H.; Yang, D.-Y.; Lee, K.-S. Two-photon stereolithography for realizing ultraprecise three-dimensional nano/microdevices. *Laser & Photonics Reviews* **2009**, *3*, 1–11.

(202) Lio, G. E.; Ritacco, T.; Ferraro, A.; Luca, A. D.; Caputo, R.; Giocondo, M. Hyper Resolution Two Photon Direct Laser Writing using ENZ Nano-Cavity., 2020.

(203) Lio, G. E.; Ferraro, A.; Ritacco, T.; Aceti, D. M.; De Luca, A.; Giocondo, M.; Caputo, R. Leveraging on ENZ Metamaterials to achieve 2D and 3D Hyper Resolution in Two-Photon Direct Laser Writing. *Advanced Materials* **2021**, *33*, DOI: 10.1002/adma.202008644.

(204) Yin, X.; Fang, N.; Zhang, X.; Martini, I. B.; Schwartz, B. J. Near-field two-photon nanolithography using an apertureless optical probe. *Applied Physics Letters* **2002**, *81*, 3663–3665.

(205) Hell, S. W. Improvement of lateral resolution in far-field fluorescence light microscopy by using two-photon excitation with offset beams. *Optics communications* **1994**, *106*, 19–24.

(206) Sánchez, E. J.; Novotny, L.; Xie, X. S. Near-field fluorescence microscopy based on two-photon excitation with metal tips. *Physical Review Letters* **1999**, *82*, 4014.

(207) Imura, K.; Nagahara, T.; Okamoto, H. Near-field two-photon-induced photoluminescence from single gold nanorods and imaging of plasmon modes. *The Journal of Physical Chemistry B* **2005**, *109*, 13214–13220.

(208) Zeng, X.; Bergman, D.; Hui, P.; Stroud, D Effective-medium theory for weakly nonlinear composites. *Physical Review B* **1988**, *38*, 10970.

(209) Rousselle, D; Berthault, A; Acher, O; Bouchaud, J.; Zerah, P. Effective medium at finite frequency: Theory and experiment. *Journal of Applied Physics* **1993**, *74*, 475–479.

(210) Mocella, V; Cabrini, S; Chang, A.; Dardano, P; Moretti, L.; Rendina, I; Olynick, D; Harteneck, B; Dhuey, S Self-collimation of light over millimeter-scale distance in a quasi-zero-average-index metamaterial. *Physical review letters* **2009**, *102*, 133902.

(211) Pollès, R.; Centeno, E.; Arlandis, J.; Moreau, A. Self-collimation and focusing effects in zero-average index metamaterials. *Optics express* **2011**, *19*, 6149–6154.

(212) Di Caprio, G.; Dardano, P.; Coppola, G.; Cabrini, S.; Mocella, V. Digital holographic microscopy characterization of superdirective beam by metamaterial. *Optics letters* **2012**, *37*, 1142–1144.

(213) Arlandis, J.; Centeno, E.; Pollès, R.; Moreau, A. In *Photonic Crystal Materials and Devices X*, 2012; Vol. 8425, p 842510.

(214) Palermo, G.; Lio, G. E.; Strangi, G. Compressed and canalized emission of quantum emitters in MIM nano-cavities. *Quantum Stud.: Math. Found.* **2020**, DOI: `https://doi.org/10.1007/s40509-020-00231-9`.

(215) Fang, N.; Zhang, X. In *Proceedings of the 2nd IEEE Conference on Nanotechnology*, 2002, pp 225–228.

(216) Casse, B.; Lu, W.; Huang, Y.; Gultepe, E; Menon, L; Sridhar, S Super-resolution imaging using a three-dimensional metamaterials nanolens. *Applied Physics Letters* **2010**, *96*, 023114.

(217) Zhao, Y.; Nawaz, A. A.; Lin, S.-C. S.; Hao, Q.; Kiraly, B.; Huang, T. J. Nanoscale super-resolution imaging via a metal–dielectric metamaterial lens system. *Journal of Physics D: Applied Physics* **2011**, *44*, 415101.

(218) Kim, M.; Rho, J. Metamaterials and imaging. *Nano Convergence* **2015**, *2*, 22.

(219) Chen, W. T.; Zhu, A. Y.; Sanjeev, V.; Khorasaninejad, M.; Shi, Z.; Lee, E.; Capasso, F. A broadband achromatic metalens for focusing and imaging in the visible. *Nature nanotechnology* **2018**, *13*, 220–226.

(220) Fan, Z.-B.; Qiu, H.-Y.; Zhang, H.-L.; Pang, X.-N.; Zhou, L.-D.; Liu, L.; Ren, H.; Wang, Q.-H.; Dong, J.-W. A broadband achromatic metalens array for integral imaging in the visible. *Light: Science & Applications* **2019**, *8*, 1–10.

(221) Idjadi, M. H.; Aflatouni, F. Nanophotonic phase noise filter in silicon. *Nature Photonics* **2020**, *14*, 234–239.

(222) Gao, Y.; Xin, Z.; Zeng, B.; Gan, Q.; Cheng, X.; Bartoli, F. J. Plasmonic interferometric sensor arrays for high-performance label-free biomolecular detection. *Lab on a Chip* **2013**, *13*, 4755–4764.

(223) Engelberg, J.; Levy, U. The advantages of metalenses over diffractive lenses. *Nature Communications* **2020**, *11*, 1–4.

(224) Byrnes, S. J.; Lenef, A.; Aieta, F.; Capasso, F. Designing large, high-efficiency, high-numerical-aperture, transmissive meta-lenses for visible light. *Optics express* **2016**, *24*, 5110–5124.

(225) Khorasaninejad, M.; Shi, Z.; Zhu, A. Y.; Chen, W.-T.; Sanjeev, V.; Zaidi, A.; Capasso, F. Achromatic metalens over 60 nm bandwidth in the visible and metalens with reverse chromatic dispersion. *Nano letters* **2017**, *17*, 1819–1824.

(226) Khorasaninejad, M.; Capasso, F. Metalenses: Versatile multifunctional photonic components. *Science* **2017**, *358*, eaam8100.

(227) She, A.; Zhang, S.; Shian, S.; Clarke, D. R.; Capasso, F. Large area metalenses: design, characterization, and mass manufacturing. *Optics express* **2018**, *26*, 1573–1585.

(228) Khorasaninejad, M.; Aieta, F.; Kanhaiya, P.; Kats, M. A.; Genevet, P.; Rousso, D.; Capasso, F. Achromatic metasurface lens at telecommunication wavelengths. *Nano letters* **2015**, *15*, 5358–5362.

(229) Khorasaninejad, M.; Chen, W. T.; Devlin, R. C.; Oh, J.; Zhu, A. Y.; Capasso, F. Metalenses at visible wavelengths: Diffraction-limited focusing and subwavelength resolution imaging. *Science* **2016**, *352*, 1190–1194.

(230) Khorasaninejad, M.; Capasso, F. Metalenses: Versatile multifunctional photonic components. *Science* **2017**, *358*, eaam8100.

(231) Aieta, F.; Kats, M. A.; Genevet, P.; Capasso, F. Multiwavelength achromatic metasurfaces by dispersive phase compensation. *Science* **2015**, *347*, 1342–1345.

(232) Park, J.-S.; Zhang, S.; She, A.; Chen, W. T.; Lin, P.; Yousef, K. M.; Cheng, J.-X.; Capasso, F. All-glass, large metalens at visible wavelength using deep-ultraviolet projection lithography. *Nano letters* **2019**, *19*, 8673–8682.

(233) Ni, X.; Ishii, S.; Kildishev, A. V.; Shalaev, V. M. Ultra-thin, planar, Babinet-inverted plasmonic metalenses. *Light: Science & Applications* **2013**, *2*, e72–e72.

(234) Banerji, S.; Meem, M.; Majumder, A.; Vasquez, F. G.; Sensale-Rodriguez, B.; Menon, R. Imaging with flat optics: metalenses or diffractive lenses? *Optica* **2019**, *6*, 805–810.

(235) Shrestha, S.; Overvig, A. C.; Lu, M.; Stein, A.; Yu, N. Broadband achromatic dielectric metalenses. *Light: Science & Applications* **2018**, *7*, 1–11.

(236) Wang, S.; Wu, P. C.; Su, V.-C.; Lai, Y.-C.; Chu, C. H.; Chen, J.-W.; Lu, S.-H.; Chen, J.; Xu, B.; Kuan, C.-H., et al. Broadband achromatic optical metasurface devices. *Nature communications* **2017**, *8*, 1–9.

(237) Afridi, A.; Canet-Ferrer, J.; Philippet, L.; Osmond, J.; Berto, P.; Quidant, R. Electrically driven varifocal silicon metalens. *ACS Photonics* **2018**, *5*, 4497–4503.

(238) Wang, S.; Wu, P. C.; Su, V.-C.; Lai, Y.-C.; Chen, M.-K.; Kuo, H. Y.; Chen, B. H.; Chen, Y. H.; Huang, T.-T.; Wang, J.-H., et al. A broadband achromatic metalens in the visible. *Nature nanotechnology* **2018**, *13*, 227–232.

(239) Zhou, Y.; Zheng, H.; Kravchenko, I. I.; Valentine, J. Flat optics for image differentiation. *Nature Photonics* **2020**, 1–8.

(240) Zhu, X.; Fang, W.; Lei, J.; Li, Z.; Xie, F.; Cao, Y.; Zhang, Y.; Qin, F.; Li, X. Supercritical lens array in a centimeter scale patterned with maskless UV lithography. *Optics Letters* **2020**, *45*, 1798–1801.

(241) Huang, T.-Y.; Grote, R. R.; Mann, S. A.; Hopper, D. A.; Exarhos, A. L.; Lopez, G. G.; Kaighn, G. R.; Garnett, E. C.; Bassett, L. C. A monolithic immersion metalens for imaging solid-state quantum emitters. *Nature communications* **2019**, *10*, 1–8.

(242) Lio, G. E.; Ferraro, A.; Ritacco, T.; Aceti, D. M.; De Luca, A.; Caputo, R.; Giocondo, M. Hyper Resolute Ultra Thin Low Cost All-Dielectric Broadband Achromatic Metalenses. *arXiv preprint arXiv:2008.03250* **2020**.

(243) Jiang, J.; Fan, J. A. Global optimization of dielectric metasurfaces using a physics-driven neural network. *Nano letters* **2019**, *19*, 5366–5372.

(244) Kino, G. S.; Corle, T. R., *Confocal scanning optical microscopy and related imaging systems*; Academic Press: 1996.

(245) Decker, M.; Chen, W. T.; Nobis, T.; Zhu, A. Y.; Khorasaninejad, M.; Bharwani, Z.; Capasso, F.; Petschulat, J. Imaging performance of polarization-insensitive metalenses. *ACS Photonics* **2019**, *6*, 1493–1499.

(246) Genevet, P.; Capasso, F.; Aieta, F.; Khorasaninejad, M.; Devlin, R. Recent advances in planar optics: from plasmonic to dielectric metasurfaces. *Optica* **2017**, *4*, 139–152.

(247) Chen, W. T.; Zhu, A. Y.; Capasso, F. Flat optics with dispersion-engineered metasurfaces. *Nature Reviews Materials* **2020**, 1–17.

(248) Gissibl, T.; Thiele, S.; Herkommer, A.; Giessen, H. Two-photon direct laser writing of ultracompact multi-lens objectives. *Nature Photonics* **2016**, *10*, 554.

(249) Chen, X.; Huang, L.; Mühlenbernd, H.; Li, G.; Bai, B.; Tan, Q.; Jin, G.; Qiu, C.-W.; Zentgraf, T.; Zhang, S. Reversible Three-Dimensional Focusing of Visible Light with Ultrathin Plasmonic Flat Lens. *Advanced Optical Materials* **2013**, *1*, 517–521.

(250) Arbabi, A.; Arbabi, E.; Mansouree, M.; Han, S.; Kamali, S. M.; Horie, Y.; Faraon, A. Increasing efficiency of high numerical aperture metasurfaces using the grating averaging technique. *Scientific Reports* **2020**, *10*, 1–10.

(251) Lee, D.; Gwak, J.; Badloe, T.; Palomba, S.; Rho, J. Metasurfaces-based imaging and applications: from miniaturized optical components to functional imaging platforms. *Nanoscale Advances* **2020**.

(252) Bayati, E.; Pestourie, R.; Colburn, S.; Lin, Z.; Johnson, S. G.; Majumdar, A. Inverse designed metalenses with extended depth of focus. *ACS Photonics* **2020**, *7*, 873–878.

(253) Suwannasopon, S.; Meyer, F.; Schlickriede, C.; Chaisakul, P.; Limtrakul, J.; Zentgraf, T.; Chattham, N., et al. Miniaturized Metalens Based Optical Tweezers on Liquid Crystal Droplets for Lab-on-a-Chip Optical Motors. *Crystals* **2019**, *9*, 515.

(254) Wei, Y.; Wang, Y.; Feng, X.; Xiao, S.; Wang, Z.; Hu, T.; Hu, M.; Song, J.; Wegener, M.; Zhao, M., et al. Compact Optical Polarization-Insensitive Zoom Metalens Doublet. *Advanced Optical Materials* **2020**, 2000142.

(255) Malekovic, M.; Urann, M.; Steiner, U.; Wilts, B. D.; Kolle, M. Soft Photonic Fibers for Colorimetric Solvent Vapor Sensing. *Advanced Optical Materials* **2020**, 2000165.

(256) Kim, J. A.; Wales, D. J.; Thompson, A. J.; Yang, G.-Z. Fiber-Optic SERS Probes Fabricated Using Two-Photon Polymerization For Rapid Detection of Bacteria. *Advanced Optical Materials* **2020**, *8*, 1901934.

UNIVERSITÀ DELLA CALABRIA

ABSTRACT:

In this Doctoral Thesis, we carried out a research work aiming at the design, fabrication and characterization of novel metamaterials able to extremely improve the resolution of the two photon direct laser writing process. The method proposed to improve the resolution of the photopolymerization process could be convenient because it is low-cost and fast. Common denominator of all metamaterial devices is the initial optical nano-cavity configuration composed by metal/ insulator/ metal/ insulator or, as we already called, MIMI. These systems present some features as the tunable resonant wavelength as a function of the dielectric cavity thickness and it allows to design a system that works at the operation wavelength used in the TP-DLW setup. The procedure for the optimization of the design of the proposed devices has been performed by means of a home-built TMM code and implemented with a Finite Element Method (FEM) in COMSOL Multiphysics, a commercial software. Successively, the MIMI systems have been fabricated using standard DC-Sputtering. All the experimental measurements agree very well with the simulation results confirming the great quality of the work both in terms of simulation and fabrication/ characterization. The perfect match between the fabricated MIMI and our TP-DLW setup allowed us producing some tests in order to confirm the increase in terms of writing resolution, the realization of samples exploitable in labels based-on physical anti-counterfeiting that can open the way for unclonable devices, and the last but not the least, the fabrication of all-dielectric ultra-flat metalenses that show incredible features as achromaticity, a broad working spectral range, extended focal length and depth of focus, and a numerical aperture comparable with the already realized metalenses.